Faculty of Mechanical and Industrial Engineering

Dissertation

Development of a comprehensive cylinder lubrication model for reciprocating piston compressors to minimise oil consumption

carried out for the purpose of obtaining the degree of Doctor technicae (Dr. techn.),

submitted at TU Wien, Faculty of Mechanical and Industrial Engineering,

by

Dipl.-Ing. Bernhard Fritz

Matr.Nr.: 0326461
Elisabethallee 81/1/7, 1130 Wien

under the supervision of

Priv.-Doz. Dipl.-Ing. Dr. techn. Bernhard Scheichl
Institute of Fluid Mechanics and Heat Transfer (E322),
TU Wien

reviewed by:

Univ.-Prof. Dipl.-Ing. Dr.mont. Thomas Antretter
Institute of Mechanics,
Montanuniversität Leoben

Univ.-Prof. Dr.-Ing. Carsten Gachot
Institute of Engineering Design and Product Development (E307),
TU Wien

I confirm, that going to press of this thesis needs the confirmation of the examination committee.

Affidavit
I declare in lieu of oath, that I wrote this thesis and performed the associated research myself, using only literature cited in this volume. If text passages from sources are used literally, they are marked as such.
I confirm that this work is original and has not been submitted elsewhere for any examination, nor is it currently under consideration for a thesis elsewhere.

Vienna, July, 2019 . . . .
Signature

Kurzfassung

Die Schmierung der Zylinderlaufbahn von doppelwirkenden Kolbenkompressoren wird als Verlustschmierung ausgeführt. Diese minimiert die Reibung zwischen Zylinderwand und Ringen und erhöht die Lebensdauer letzterer. Mangelschmierung führt zu höherem Verschleiß, Überschmierung hingegen bringt kaum Vorteile, führt aber häufig zu zusätzlichen Problemen von Komponenten stromabwärts.

Mangels fehlender Alternativen wird in der Kompressorindustrie die Schmierrate mittels einfacher, empirischer Formeln und Richtlinien bestimmt. Diese gehen nicht auf systemspezifische Parameter wie z.B. Spaltmaße, Kolbenlayout, Ölviskosität ein, und geben keinen Aufschluss darüber, wie eine fallabhängige Schmierstrategie aussehen sollte, welche neben der minimalen Schmierrate den optimalen Zeitpunkt der Schmieröleinbringung berücksichtigt.

Ziel dieser Arbeit ist es diese Forschungslücke zu schließen und die für den Ölverbrauch verantwortlichen Mechanismen zu untersuchen und eine Schmierstrategie zu entwickeln. Dies ist mit ausschließlich experimentellen Methoden kaum möglich.

Um den Ölverbrauch abschätzen zu können wurde ein Simulationsmodell entwickelt, welches die wechselseitigen Abhängigkeiten von Ölfilm, komprimierten Gas, Kolben– und Tragringen, Kolbenbewegung, Kolbenstangendurchbiegung sowie der Kreuzkopfbewegung abbildet. Zur Problembeschreibung werden unterschiedliche Skalen benötigt: Die Makroskala beschreibt das globale Systemverhalten des Kompressors. Die Beschreibung der für die Aufgabenstellung wichtigen Sekundärbewegungen des Kolbens (Bewegungen normal zur Hauptrichtung der Kolbenbewegung) verlangt sowohl die Betrachtung des Kurbeltriebs, als auch die Berücksichtigung der Kreuzkopfbewegungen (Sekundärbewegung und Kippen). Die Spalte zwischen Ringflächen und Zylinderwand, sowie zwischen Kreuzkopf und Kreuzkopfführungen ergeben die Mesoskala und sind essentiell zur Lösung der Bewegungsgleichungen in der Makroskala. Auf der Ebene der Mesoskala werden elastohydrodynamische Effekte und ihre Auswirkungen auf den Netto-Ölstrom untersucht. Hierfür wird das kommerzielle Finite-Elemente Programm ABAQUS/Standard verwendet, um die elastischen Ringverformungen zu berechnen und so das vollgekoppelte elastohydrodynamische Schmierproblem zu lösen. Der hierzu notwendige Schmierspaltdruck wird in einer benutzerdefinierten Subroutine gerechnet und mittels eines Finiten Volumen Schemas 2. Ordnung implementiert.

Das so aufgestellte numerische Modell erlaubt eine genaue Betrachtung der Interaktion Zylinderwand-Ölfilm-Kolbenring-Tragring und eröffnet so zum ersten Mal die Möglichkeit, den Einfluss verschiedener Parameter auf den Netto-Ölstrom, und folgend auf die kompressorspezifische Schmierstrategie mittels einer Parameterstudie zu ermitteln.

Abstract

Cylinder loss lubrication is common practice in the piston compressor industry to reduce friction between rings and cylinder wall and to extend their lifetime. While starved lubrication shortens the lifetime, over-lubrication adds little benefit while potentially giving rise to additional problems in downstream components due to oil carry-over not to forget the environmental aspect.

Due to a lack of alternatives, it is state-of-the-art to lube compressors according to basic empirical guidelines. These guidelines disregard system-specific parameters such as clearance, piston assembly, oil viscosity, etc. and provide no guidance on an optimal lube strategy (e.g. timing of lube injection).

It is therefore the objective of this study to substantially deepen the insight into the mechanisms of oil loss to get a solid understanding of the mechanisms that are responsible for the accumulated net oil flow along the piston and to shed light on what constitutes an optimal lube strategy — something that is almost impossible to achieve by purely experimental means.

Thus a comprehensive simulation model has been developed that accounts for the mutual interactions between the oil film, the compressed gas, the piston rings and rider rings, the piston motion, the bending of the piston rod, and the crosshead motion. The approach pursued is of spatial multi-scale nature. The presented model deals with the macroscopic characteristics as covered in formulating the dynamical behaviour of the entire drive, which is capable of describing the secondary piston movements — the piston motion normal to the primary direction of piston movement. This necessarily includes the crank and the crosshead. The resulting gaps between cylinder and rings as well as between crosshead and crosshead shoes form the meso-scale and are essential ingredients for closing the hitherto unclosed equations of motion on the macro-scales. A fully coupled elastohydrodynamic calculation is done to research elastohydrodynamic effects in the ring regions, using the commercial finite-element analysis program ABAQUS/Standard to calculate the elastic ring deformations. The corresponding lubrication pressure is computed via a user-defined subroutine that employs a finite-volume scheme with second-order accuracy as adopting the finite-element discretisation. The simultaneously calculated pressure distribution between crosshead and crosshead slide governs the coupled dynamics of crosshead.

The resultant numerical model takes a close look at the interaction cylinder wall–oil film–rider– and piston rings and allows for an accurate numerical parametric study placing emphasis on the oil flow rate.

Acknowledgements

First I want to express my gratitude to HOERBIGER who allowed me to work on such a varied field of research and made it possible to conduct my thesis. I also want to thank my supervisor, Dr. Bernhard Scheichl for his support.

Additional thanks go to Dr. Bernhard Spiegl who initiated the project. I would like to express my special gratitude to Dr. Matthias Kornfeld and Dr. Tino Lindner-Silvester who have always supported me in the course of this work and have given me many times valuable advice. I thank the whole HOERBIGER R&D Team for their support. Here, special thanks go to Dr. Georg Meyer for many fruitful and productive discussions and Jonathan Gauster, Alexander Jandl and Martin Lagler who helped to realize test rigs and to execute experimental tests which are not part of this theses but whose findings helped to better comprehend the overall problem after all.

Finally, I would like to thank my family and friends for their support, patience, helpfulness and humour throughout the time.

Contents

Contents

1 Introduction

By far most of the reciprocating gas compressors depend on a reliable lubrication which

1. reduces friction between moving part,

2. carries heat away from bearing surfaces,

3. prevents corrosion both during operation and when compressor is stopped,

4. and reduces gas leakage between seal faces and close clearances [30].

The main purpose of cylinder lubrication is certainly the reduction of friction between rings and cylinder wall to extend the rings' lifetime. Excessive wear as a result of under-lubrication leads to a decrease of efficiency (gas leakage due to worn rings) or in the worst case to a metallic contact between piston and cylinder wall. Both events require critical, unplanned maintenance time resulting in additional costs, which conflicts with present efforts of increasing operational time.

Currently, no first-principles-based theory of minimal oil demand for a reliable compressor operation is available. Due to lack of alternatives, it is state-of-the-art in the compressor business to estimate optimal lube rates by quite basic empirical design formulas and charts [30, Ch. 18]. They do not account for system specific parameters like clearance, piston assembly (mass, ring configuration, ring profile, . . .), oil viscosity, etc. and give no guidance for an optimal lube strategy, which would also include instructions covering the timing of lube injections. They must generally be viewed as too conservative as resulting in most compressors to be over-lubricated. However, since cylinder lubrication is a loss lubrication, all lube oil eventually ends up in the discharge pipe, leading to displeasing side effects like

- high operating costs,

- reduced valve life due oil sticking,

- and decreased pipeline hydraulic efficiency due to oil fouling.

These negative consequences of cylinder lubrication are increased by over-lubrication, not to forget the environmental aspect of wasting oil, which is gaining significance.

1.1 **Approach**

First, the regions where lubrication comes into play are investigated: the ring regions. Analysis of the lubricated ring-regions and the evaluation of oil transport along the rings demand a most accurate prediction of the motion of the piston including the representation of the secondary piston movements — the motion normal to the primary direction of piston movement — due to the time dependent piston tilt, which is a consequence of piston– and crosshead clearances. The piston tilt causes a symmetry break in time and allows for a hydrodynamic lubrication between cylinder wall and rings. This leads to the derivation of a global compressor model, which is a lumped-element model with ideal bearings — they are assumed to have zero clearance and do not transmit a moment — enhanced by a 1D Ritz ansatz describing the bending of the piston rod. Hence, apart from the piston rod, all parts — the cranked shaft, connecting rod, crosshead and piston — are assumed to be rigid. To describe the tilt of the piston, vertical displacements of the crosshead $y_{\mathrm{C}}(t)$ as well of the piston $y_{\mathrm{P}}(t)$ are accounted for.

Oil transport along the rings (both rider– and piston rings) is an important mechanism concerning cylinder lubrication, but does not solely describe the loss of oil. For an understanding of oil loss, it is also important take a look at the oil film on the cylinder next to the rings, which is done in a second step. This oil film interacts on the one hand with the ring regions. Low film heights next to the rings can lead to starved lubrication, which in turn affects the piston dynamic and might be an indication of under-lubrication, resulting in increased ring-wear. On the other hand, this oil film interacts with the gas stream, which forces an amount of oil to finally leave the compressor chamber through the discharge valve.

Finally, the term and condition "under-lubrication" is addressed. From the customer's perspective it is clear that under-lubrication leads to higher wear and shorter service intervals. However, also properly lubricated rings need to be changed regularly, indicating that there is no clear distinction between properly lubricated and under-lubricated rings. In this work we look for indications of under-lubrication and their dependence on amount of lubrication, time and position of injection. A starving parameter St is introduced, which is a measure for under-lubrication of each ring per cycle. As a contrast, the term "starving" will be used to describe the condition of any gap, which is not fully flooded with oil, but is partially wetted. This can happen due to the interplay between rings, due to the relatively high position dependent gap heights (up to $\approx 0.5\,\mathrm{mm}$), or because of under-lubrication. Hence, some regions will experience starved conditions, even though the machine is not under-lubricated.

The simulation tool "Global cylinder lubrication model" (see Sec. 5.4), implemented in MATLAB (MathWorks, Commercial license, Release R2016a) is derived by developing the following main modules, visualized in Fig. 1.1:

dynamical compressor model (see Ch. 4) with 3 DOF (vertical crosshead movement, tilt of piston rod, bending of piston rod), being able to predict the secondary piston motions (both tilt and vertical movements).

rider ring- and crosshead model (see Sec. 4.2), which close the 3 DOF model and describe the motion dependent impressed forces and moments acting on the piston and crosshead. The rider ring model is implemented both in ABAQUS/Standard (Release 6.14-1, Dassault Systèmes Simulia Corp., Providence, RI, USA) and in MATLAB: A fully coupled elastohydrodynamic calculation is done with ABAQUS/Standard which accounts for the elastic deformations of the rider ring to evaluate its impact on oil consumption (see Sec. 5.3). The implementation in MATLAB is done with the assumption of rigid rings: Elastohydrodynamic effects are neglected to decrease calculation time.

piston ring model (see Sec. 4.2), describing the motion of the piston rings: Although any forces being transmitted from the piston rings to the piston (contact forces) are neglected, it is important to know the piston ring's movement for the description of oil flow along these rings.

2-equations gas pressure model (see Sec. 3.7 and 5.1.3), describing the time dependent pressure variation in the compression chamber as well as between any piston rings.

CFD model of flow in compression chamber (see Sec. 5.2): a CFD model using FLUENT (ANSYS FLUENT, Commercial license, Release 14.5.7) is developed to derive pressure gradients and wall shear stresses due to the gas flow in the compression chamber. These results are used to estimate oil film dynamics due to the gas flow.

The main novelties in this work are

- the development of a multi-scale dynamic compressor model, which is capable of describing the afore-mentioned secondary piston movements:
    - macro-scale: the machine dynamics describing the piston motion;
    - meso-scale: resulting gaps between cylinder wall and rings;
    - micro-scale: wear, roughness and mixed lubrication; surface roughness and time– and solution dependent wear are not implemented yet, but show how this model could be expended in future.

- the treatment of the ring area, modelled as a free boundary problem, including full fluid film lubrication, and a passive region, where the gap between cylinder and rings is too big to be flooded with oil resulting in a free surface flow.

- the analysis of elastohydrodynamic lubrication (EHL) effects in a fully coupled elastohydrodynamic calculation of the rider ring area: It is a priori not known, if elastohydrodynamic effects — the interaction between elastic deformations and oil pressure distribution — play an important role. Therefore, an elastohydrodynamic lubrication model is developed, using ABAQUS/Standard for

3
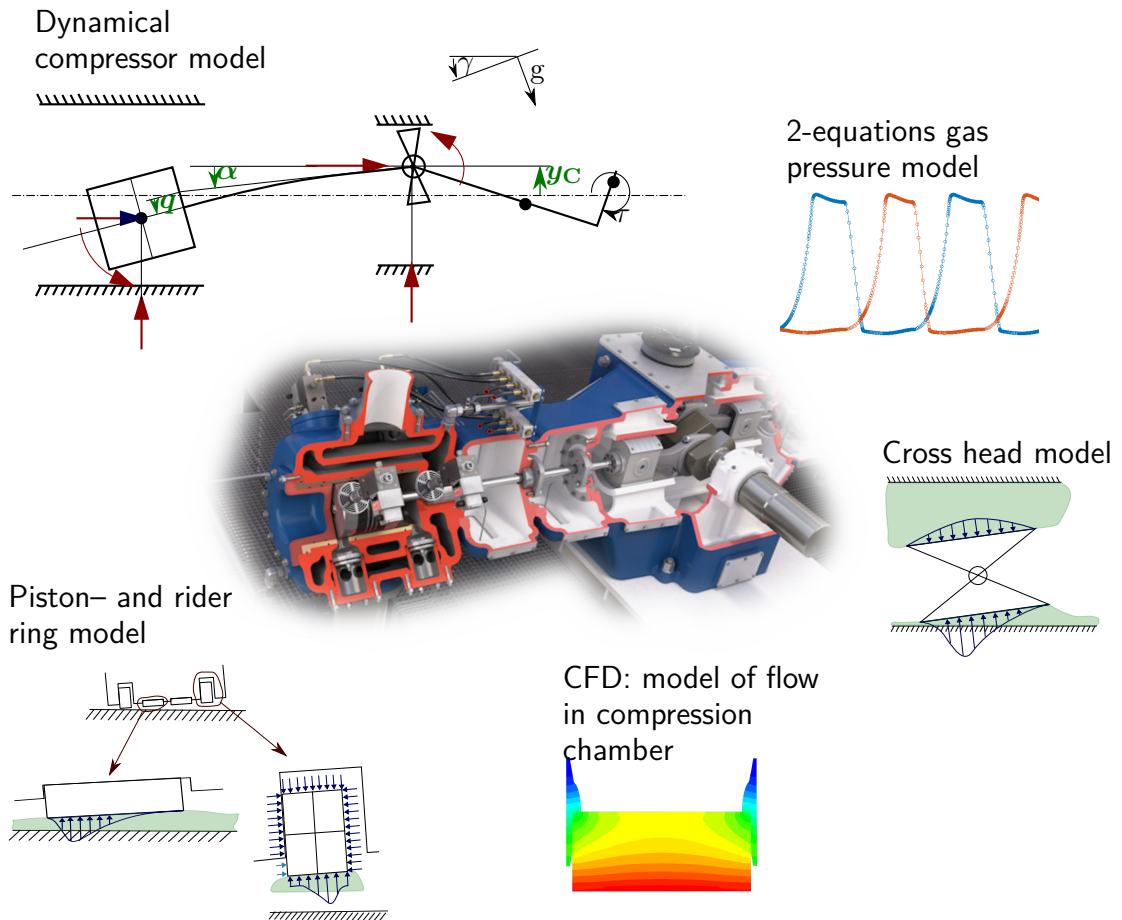
Figure 1.1: Map of simulation models used to derive an assumption of oil consumption.

> the FEM-discretisation of the rider ring. The Reynolds equation is applied as a dynamic boundary condition via a Fortran-subroutine.

A comprehensive list of all abbreviations, symbols, indices and acronyms is found at the end of this work. Not all of them will be explained explicitly in the course of this work. Above all, dimensioned quantities are marked by a tilde — where necessary: To simplify the representation of equations, this marking is omitted in cases, where solely dimensioned equations are used. Therefore, if tildes are in use, their use is mentioned at the beginning of each chapter or section. Tildes are also omitted in the list of symbols.

1.2 State of the art

This section will start giving an introduction about compressor basics, which are important to know to develop a theory of cylinder lubrication, followed by an overview

of the relevant literature which is found about this topic. Last but not least, the pressure and temperature dependence of oil viscosity is presented: Oil viscosity is the most important oil property concerning hydrodynamic lubrication.

1.2.1 Compressor basics

Functions and main components of reciprocating compressors shall be described very shortly, focusing mainly on components important for cylinder lubrication. More detailed information is found in the seminal textbooks, e.g. [30], [8], [7], [38]. The following information is taken from the textbooks mentioned above and from [42].

A reciprocating piston compressor is a positive displacement machine: It uses a piston to compress gas and delivers it at high pressure and can either be single-acting (compressing on one side of the piston) or double-acting (compressing on both side of the piston). Most compressors in use are of the double-acting type. The primary components of a typical compressor system are shown in Fig. 1.2: Discharge- and suction valves, piston assembly, piston rod, packing assembly, crosshead, and the housings called cylinder and crankcase. Both suction- and discharge valves are mechanically driven, permitting gas to flow in one direction only when a certain differential pressure across the valve is reached. The number of suction- and discharge valves of each cylinder (also called stage) varies and depends on system design. Since most compressors run with a fixed number of revolutions per minute, the full load carried by the compressor at fixed pressure levels is controlled by "unloaders" or clearance pockets: Unloaders force the suction valves to stay open for a limited time each cycle allowing the gas to recycle. Clearance pockets alter the cylinders head space (clearance volume), changing volumetric efficiency (the ratio between actual volume inducted and the swept volume of the piston).

The piston assembly consists of the piston including a number of rings which take the piston load and seal against gas pressure (see Sec. 1.2.2) and is rigidly connected to the crosshead via the piston rod. A packing assembly contains gas pressure within the cylinder (seal rings) and prevents oil from escaping along the rod out of the crankcase or distance piece (oil wipers). The distance piece connects the compressor frame to the cylinder, decreasing additionally any oil leakage from compressor frame to the cylinder, and gas leakage vice versa. The crosshead reduces the sideways forces acting on the piston due to the crank drive. Also, it allows a very small bore-to-stroke ratio, preventing the connecting rod hitting the cylinder-wall. It is rigidly coupled to the piston rod, moving primarily translatory and transmitting the force of the crank drive to the piston rod.
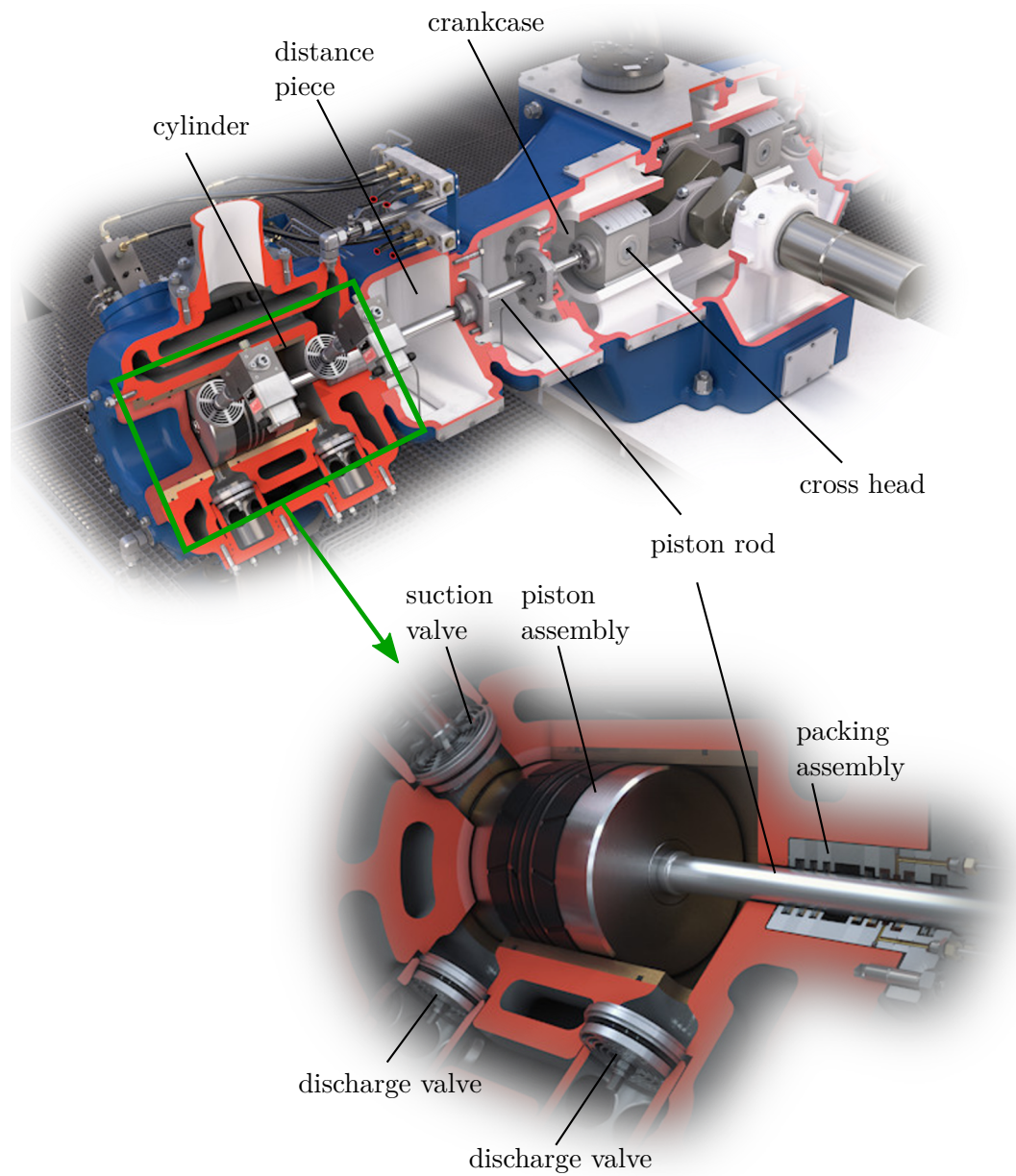
Figure 1.2: Stucture of dual-acting reciprocating compressor (©HOERBIGER)

1.2.2 Piston assembly

A typical piston assembly is shown in Fig. 1.3: It usually consists of two different ring types: rider rings and piston rings, both are nowadays usually made out of plastic compounds.
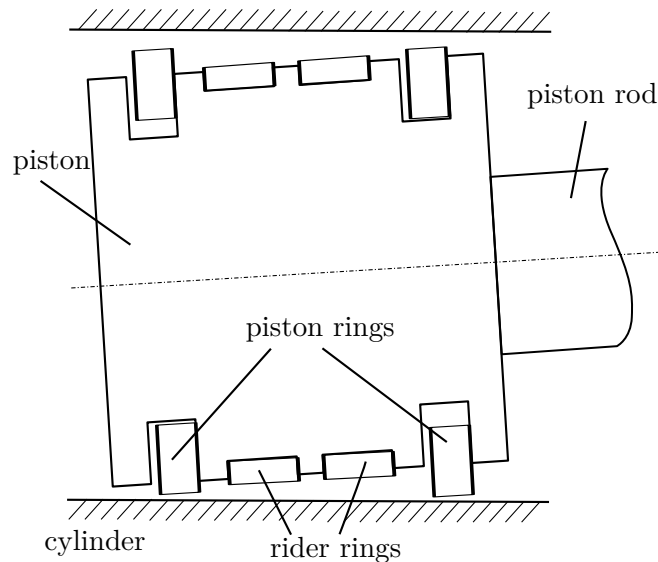
Figure 1.3: Possible piston assembly of reciprocating piston compressor: Two different ring constructions are used: Rider rings are designed to take the load due to mass forces while the piston rings' function is solely to seal against gas pressure.

Piston rings are exclusively designed to seal against gas pressure: During operation, they are pushed against the cylinder wall, which is accomplished by: (1) either a minimum differential pressure, which activates each piston ring, (2) rings, which are oversized manufactured or (3) an expander, which pushes each ring against the cylinder wall to seal against gas pressure. They exert influence on piston forces only by frictional forces between ring surface and groove surface. These are negligible against the total forces. Piston rings are mostly slotted and persist of one or more pieces for an easy placement in the piston ring groove. This makes them very flexible. Figure 1.4 shows different representative designs of slotted piston rings, including a ring designed for the use with an expander (last image). Figure 4.5 shows a typical cross section of a piston ring with acting pressures.

Rider rings, on the other hand, are pressure balanced and are seated solidly on the piston: axially placed nuts guarantee equal pressure at both sides and prevent them from pressure actuating like piston rings — they are not designed to seal but to take the load acting on the piston. Number and dimensions of rider rings depend on the mass of piston and piston rod. They are designed to support piston weight plus one-half rod weight. There are numerous different shapes of nuts, some representative

(a) linear sliced   (b) step sliced   (c) multiple sliced   (d) multiple sliced with expander
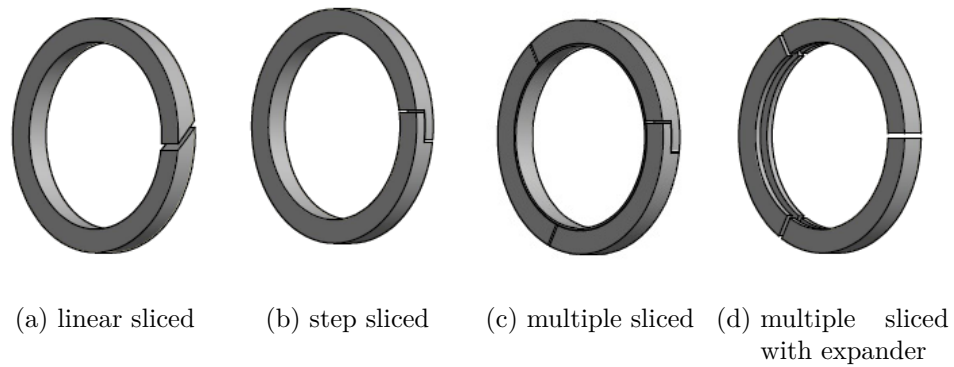
Figure 1.4: Different piston ring designs
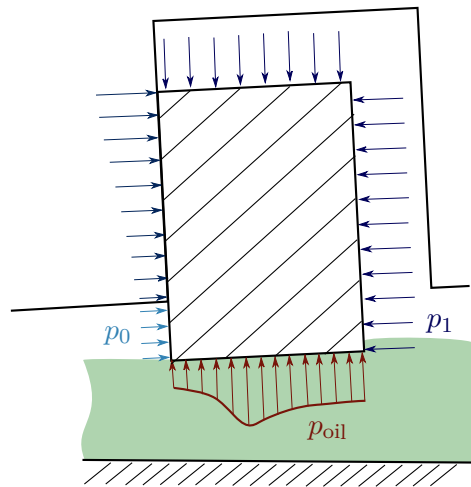
Figure 1.5: Load situation of piston rings;

designs are shown in Fig. 1.6.

1.2.3 Compressor lubrication

Two main areas need to be lubricated: The crosshead and the piston– and rider rings.

The crosshead is hydrostatically lubricated with a hydrostatic pressure of typically 4 bar–7 bar. A grid of channels distribute the hydrostatic pressure along the crosshead's surfaces (see Fig. 1.7). The same oil is used to lubricate both the crank drive as well as the crosshead and stays within the housing.

Cylinder lubrication, on the other hand, is a loss lubrication, oil passes "once through" the cylinder with no recycling. It is usually supplied by one to three lubrication channels per cylinder, which are centrally arranged around the surface. Most lubrication systems supply the oil via piston pumps at random times compared

(a) not - sliced   (b) linear sliced   (c) once sliced with additional notches (d) multiple sliced
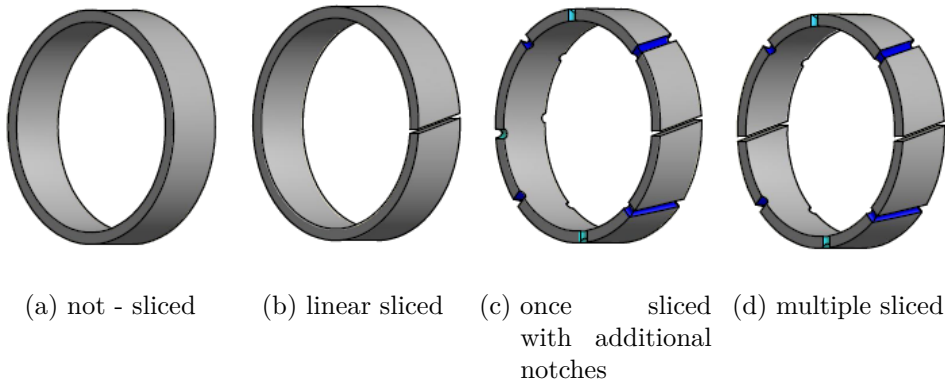
Figure 1.6: Different rider ring designs
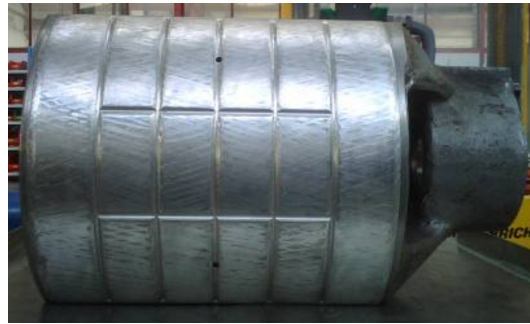
Figure 1.7: Cast steel 80 kg crosshead. A grid of lubrication channels ensures proper hydrostatic lubrication (©HOERBIGER).

to the crank angle. One recently developed lubrication system is a common rail-based system with electromagnetic valves, being capable of injecting the oil precisely in time.

Little knowledge exists on oil need of the various compressor designs, which vary in size, operation condition (speed, pressures, capacity control systems,...), lube systems, piston assembly designs (ring configuration as well as ring materials), etc. Figure 1.8 shows the impact of lubrication on compressor life: "Optimum" lubrication gives years of compressor life, while "starved" lubrication produces rapid wear and short life. "Over lubrication" gains little in operating life and requires more oil [30].

Most compressor manufacturers propose their own guidelines, which are all derived empirically and are more or less of the simple form

$$\dot{V}^{(\text{lube})} = f_{\text{e}} \times \text{stroke} \times \text{RPM} \times d_{\text{cyl}}. \tag{1.1}$$

The lube rate $\dot{V}^{(\text{lube})}$ is hereby based on the total swept surface area to be lubricated (defined by stroke and speed), modified by an empirical factor f_{e}, which accounts for

9
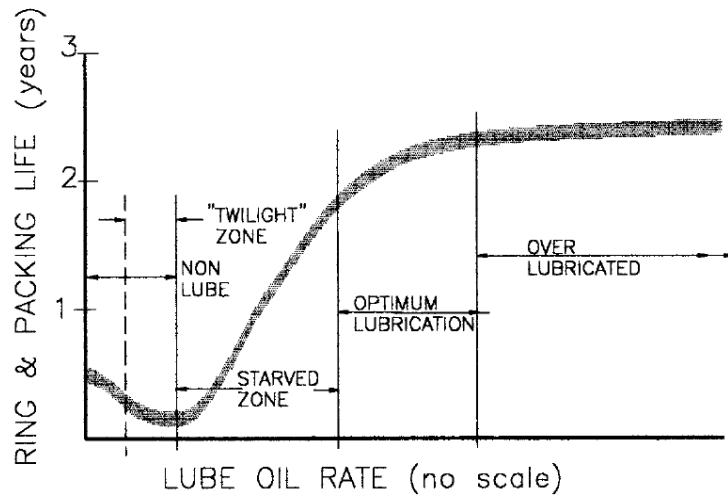
Figure 1.8: Compressor seal life vs. lube oil rate, from [30, Ch. 18]. Reprinted with permission.

different gas types etc. A graphical example of guidelines to estimate an optimum oil feed rate is shown in Fig. 1.9, which is based on (1.1): It is a 4 quadrant diagram, which takes basic compressor data (bore, speed and pressure level) into account, and includes an additional empirical factor, which depends on ring material and gas type.

1.3 Target

As mentioned above, today's knowledge about cylinder lubrication of reciprocating piston compressors is very limited. While over-lubrication reinforces problems with components downstream of the cylinder, it excludes sudden and critical maintenance time due to excessive wear as a result of under-lubrication and is therefore widely accepted. The experimental determination of an optimal lube strategy is very tedious, if not impossible: One big problem is the identification of under-lubrication: Obviously, under-lubrication results in increased ring wear: However, ring wear is only detectable after hours of operation time, resulting in experiments lasting very long times.

Let us consider the possibility to measure under-lubrication by means of oil-film measurements during operation, which would speed up experiments significantly. This has been done by a few research groups for combustion engines, for instance using the laser-induced-fluorescence technique, which requires an optical assess in the liner (e.g. [51]) or by the usage of ultrasound: This principle is based on capturing and analysing the reflection of an ultrasonic pulse at the oil film [17]. However, even if one would succeed in detecting under-lubrication on short term and in developing a lube strategy for a specific compressor, the problem arises how to adopt the derived

lube strategy to other compressors, which vary in size, geometry, speed, operating conditions etc.

Therefore, the objective of this work to substantially deepen the insight into the mechanisms inducing oil loss of reciprocating piston compressors, leading to better and preciser lubrication-guidelines for reliable and economic compressor operations. These guidelines should help to reduce oil consumption of current machines in both defining the amount of supplied oil as well as the best timing of oil injection. Lubrication systems in the past were not able to allow for precisely timed oil injection. However, current developments of lubrication systems brought substantial improvements and would allow an implementation of such guidelines.

The derivation of a lubrication guideline leads to the development of a first principle based simulation tool, which represents the most important mechanisms responsible for oil loss.

The focus is on estimating the convective net-oil flow along the piston assembly. Other aspects of oil loss in cylinder lubrication of reciprocating piston compressors, like development of oil mist due to oil injection, inertial driven detachment of accumulated oil on ring sides, oil loss through packing, etc. will just briefly be outlined for the sake of completeness in the course of this work, but will otherwise be neglected in this work and are intended to be studied in future research.
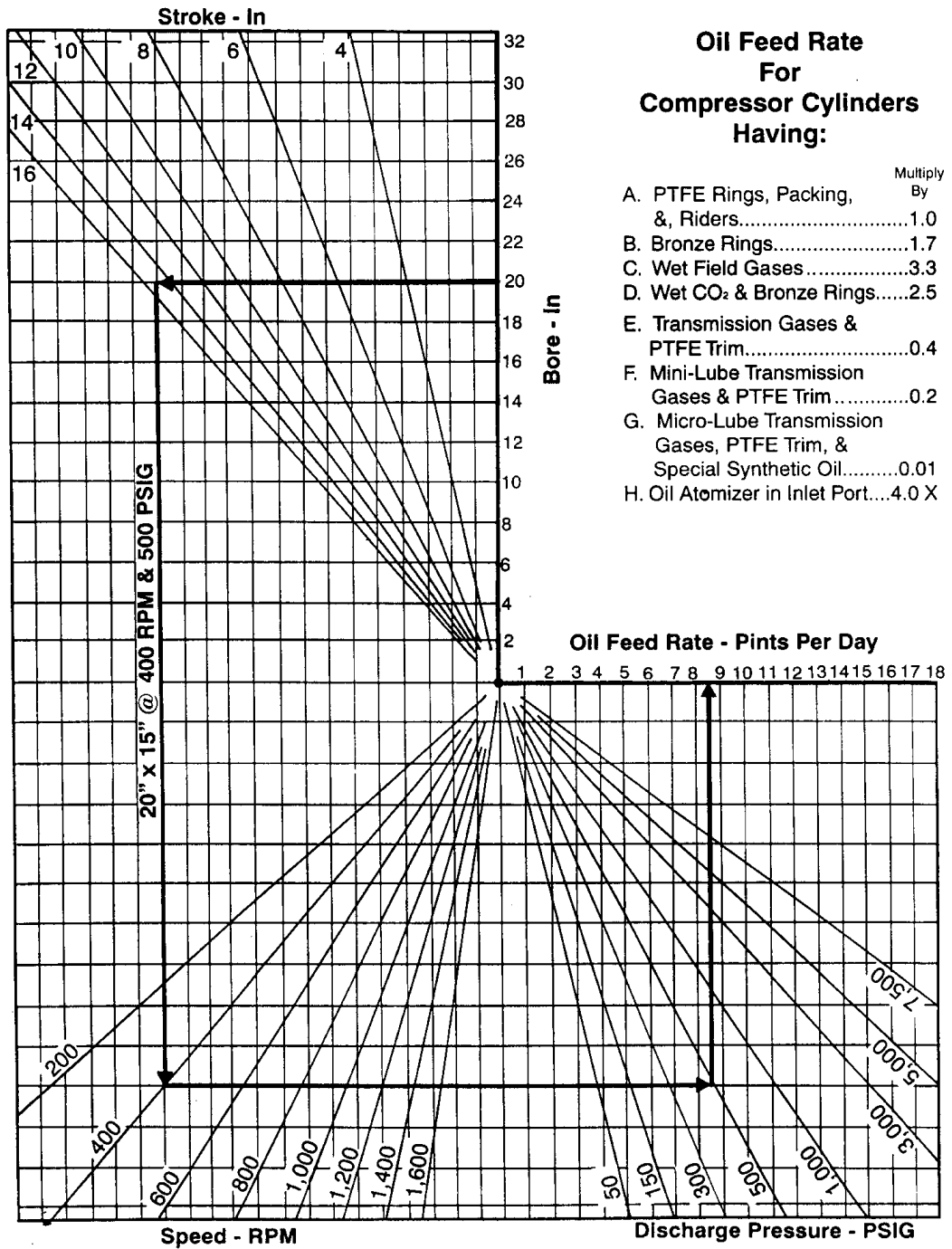
Figure 1.9: Guideline to estimate oil feed rate of compressor cylinders, from [30, Ch. 18], reprinted with permission: it is a 4-quadrant diagram, where the oil feed rate in pints per day depends on cylinder diameter (bore), compressor speed and discharge pressure.

1.4 Literature study

Literature on cylinder lubrication of reciprocating compressors is sparse. Therefore, we will also look at related problems, i.e. lubrication of reciprocating compressors employed in domestic refrigerators and of combustion engines.

Cylinder lubrication of reciprocating compressors: To the authors knowledge, there exists no theoretical research about lubrication guidelines of typical reciprocating piston compressors including crossheads, as commonly found in process- and gas industry. Some empirical work was done by different companies in the compressor market, trying to reduce lube rate[54]. This research is very tedious, since under-lubrication is hardly detectable on short term. Therefore, tests on specific compressors with specific operation conditions take at least some months—testing time is necessary to detect increase of ring wear, making it almost impossible to derive globally valid guidelines for a wide range of different compressors.

Lubrication of small reciprocating compressors: Some literature is found concerning lubrication of small reciprocating compressors employed in domestic refrigerators. Such small compressors do not have crossheads. They have no rings to reduce friction and work with very small radial piston/cylinder clearances of just a few micro meters. Therefore, they are significantly built differently than the machines researched in this work. Prata et al. [45] was the first to perform a dynamic analysis of the thin oil film between piston and cylinder of compressors with the presence of oscillating secondary piston motion. In their analysis, they assumed fully flooded gaps, whose shape was given by the tilt and eccentricity of the piston. They were interested in friction losses and gas leakage and their dependence on design parameters and operation conditions, but not in the net oil flow along pistons leading to oil consumption. Based on the model of [15], Hacioglu and Dursunkaya [26] carried out a parametric study of oil feed groove design parameters. The model of Greenwood and Trip (1971) [23], based on the classical Greenwood–Williams approach [24], is used for the calculation of boundary contact forces at the asperity contact regions. In a later work, they investigated the effect of surface roughness by implementation of the averaged Reynolds' equation [44] in the solution of the lubrication problem do define different surface textures of piston-cylinder [27]. They concluded that it is advantageous to restrict oil flow in axial direction via transverse oriented textures, since oil pressure is mainly created due to the squeeze effect. This might not be the case of bigger sized machines studied in this work, where greater clearances allow greater piston tilts. The same applies to the work of [36], who have studied the potential of partial laser surface texturing (LST) in the piston cylinder group, showing that a high density of micro dimples would decrease friction losses. However, they have not accounted for a piston tilt due to secondary piston motions and assumed parallel sliding surfaces, since they researched metallic engine piston rings.

Piston lubrication of combustion engines: Substantially more literature is found concerning piston lubrication of engines. A good point to start is the review of D'Agostino and Senatore [12], who give a detailed insight into piston ring lubrication, and the main mathematical and computer models applied so far.

Although cylinder lubrication of engines differs significantly from cylinder lubrication of compressors in many aspects, it is worth looking into it while remembering the differences, which are amongst others:

- piston layout: piston assemblies of engines commonly have three differently shaped metallic piston rings;

- they do not have a crosshead;

- temperatures are much higher;

- they are single acting machines → they have an infinite lube-oil supply at crank side;

- clearances are smaller;

- oil consumption is much less;

Important work was done by Dursunkaya and Keribar [15], who were the first to develop a hydrodynamic skirt lubrication model coupled to the secondary motion analysis of articulated (splitted piston in skirt and piston crown) and conventional piston assemblies. This model includes wristpin- and skirt lubrication submodels and calculates separately the motion of pin, rod and (for articulated pistons) skirt. In [13] elasticity effect of the surfaces and its impact on minimal gap height was first considered. In [16] the capabilities of the model presented in [15] were expended by including radial elastic deformations of the skirt. They showed the effect of skirt deformations on secondary motions and skirt friction.

Rings can have changing running conditions: At some points, they can operate fully flooded, then they can experience starved conditions. The Reynolds equation, which is typically used to calculate the pressure distribution in the lubricated gap, does not apply outside the gap. Modelling the inlet and the outlet of the lubricated gaps is very complex and is handled differently by the various authors: The easiest approach is to assume a fully flooded gap, which is done for instance in [45], [16], [18]. A more sophisticated approach is to account for for an oil built up in front of the ring: Gulwadi [25] presented the 1D implementation of the hydrodynamic lubrication equation for the piston ring, which is assumed to be flexible and can move in radial direction. This model is capable to simulate the transition between the various modes of ring lubrication (hydrodynamic, mixed, and boundary), tracks the oil film trace, which the ring is leaving and allows accumulation of oil (modelled by a trapezoidal geometry) at the leading edge of the ring. A quite similar model is given in [29], where the oil accumulation at the leading edge of the piston ring is modelled by a trapezoidal geometry. The same idea is applied in [21], except the

build up is assumed to have a parabolic shape. However, the afore mentioned shapes of menisci might be intuitive, but lack a physical justification. Felter [19] presented a 2D free surface model based on the Navier–Stokes equations, which simulates also the free surface outside the rings to overcome this problem. It does not consider effects of cavitation. The model was successfully tested on a fixed inclined slider bearing with prescribed motion, but it turns out to be computationally expensive.

In-cylinder oil consumption of combustion engines: Yilmaz et al. [56] categorized in-cylinder oil consumption of engines as follows:

- Throw-off: mechanical transport of liquid oil due to inertia forces caused by acceleration and deceleration of the piston.

The importance of this mechanism is depending on the volume and distribution of the accumulated oil on the top land and ring. Throw-off could be an issue in compressor machines, in particular when over-lubricated, although compressor do usually run slower resulting in minor inertia forces.

- Transport with reversed gas flow, which may transport oil in both liquid and mist form, in case a ring looses stability in the groove.

This happens every cycle at reciprocating compressors.

- Entrainment of oil into blow-by: transport of oil via the crankcase ventilation gases, when the pressure in the crank case exceeds the pressure in the combustion chamber. Any gas flow across the piston rings is called blow-by.

We can safely eliminate this mechanism for compressors, since there is no gas flow from the crank case to the cylinder. However, there is a gas blow-by flow from head-end to crank-end side and vice versa

- Evaporation: from liner and piston, especially during severe operating conditions with high thermal loading of engine components.

Amongst other works, oil evaporation models are presented in [55] and [39], which describe the evaporation of the oil film on the liner surface as a diffusion of oil vapour through a gas boundary layer. They accounted for distinct hydrocarbon species with own vapour pressures. [55] estimated the mass transfer Biot number, defined as the ratio of the oil species diffusion resistance in the liquid to the convection resistance in the gas phase, in the order of 10^{-3} to 10^{-2} for oil film height of a few micrometers. Therefore, he concludes that the diffusion resistance is negligible and oil evaporation is limited by gas side convection. This assumption still holds for larger film heights as expected in cylinders of bigger compressors. Taking the published assumptions of oil evaporation rates in [55] and [39] and extrapolating these assumptions to typical geometrical compressor properties, we get evaporation rates between approx. 10^{-3} l/h–10^{-1} l/h, dependent on compressor size, which are certainly small compared to usual lubrication rates of a few litres per hour. This

very rough extrapolation does not even account for much smaller gas temperatures expected in most compressors, resulting in smaller mass transfer coefficients and even lower evaporation rates.

Other authors (e.g. [31], [34]) added one more oil consumption mechanism:

- Top land scraping or Oil scraping: oil is scraped from the cylinder liner by the top land of the piston, or by carbon deposits.

This mechanism is certainly not relevant for compressor lubrication due to the greater piston clearances existing at compressors.

1.5 Temperature and pressure dependence of lubrication oil properties

The viscosity of lubrication oils decreases significantly with increasing temperatures and shows a exponential behavior. There are a number of derived approximation equations, some are purely empirical, others are derived from theoretical models. The Ubbelohde–Walter equation has become generally accepted, and forms the basis for a straight-line representation, found in American Society for Testing and Materials (ASTM) and International Organisation for Standardization (ISO) calculation guidelines :

$$\lg \lg (\nu + C) = K - m \lg T \ . \tag{1.2}$$

In this formula, the value of the kinematic viscosity ν is given in cSt ($\mathrm{mm^2 s^{-1}}$), C and K are constants, the value of T is the temperature expressed in Kelvin, and m is the double-logarithmic viscosity-temperature graph slope. The constant C is between 0.6 and 0.9 [14].

The Vogel's viscosity-temperature equation [3] performs reasonable well, however, its non-linear nature and three fluid specific coefficients (K, b, Θ_V) make it difficult for generalization [48]. It reads:

$$\eta = K \exp \left[b / (t_{\mathrm{C}} + \Theta_V) \right] \ , \tag{1.3}$$

with the value of t being the temperature expressed in Celsius. [48] gives a detailed overview of different viscosity-temperature relations found in literature.

Viscosity of oil is also pressure depending — viscosity increases with increasing pressure and can be described using the Barus law [4]:

$$\eta = \eta_0 \exp \left[\alpha_B \left(p - p_0 \right) \right] \ , \tag{1.4}$$

where α_B is the pressure-viscosity coefficient that depends on pressure and temperature (in $\mathrm{Pa^{-1}}$) and μ_0 is the dynamic viscosity at the pressure p_0 and temperature T_0.

In the work of [37], two viscosity dependency plots of typical mineral oils (HM 32 and HM 46) are shown, which are numerically derived based on the Vogel- and

Barus equation. The temperature and pressure dependent viscosity graph for HM 46 is shown in Fig. 1.10. It clearly shows both the viscosity-temperature as well as the viscosity-pressure dependency.

However, for typical compressor operating conditions it seems reasonable to assume a constant oil viscosity: Usual operating temperatures and pressures are approx. 50 °C–100 °C and 1 bar–350 bar, but with a pressure ratio less than 3. In this range, the change of viscosity is rather small.
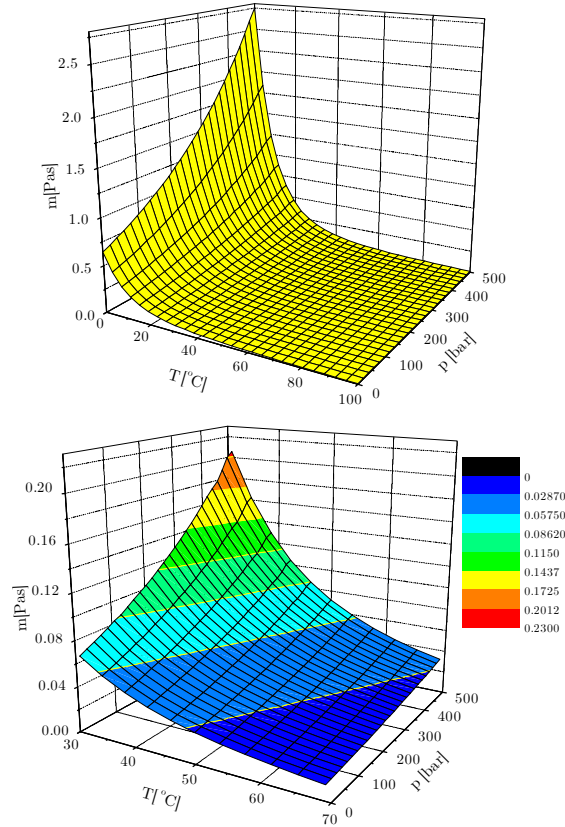
Figure 1.10: Viscosity dependency on temperature and pressure for mineral oil HM 46, taken from [37]: This graph is calculated based on the Vogel– and Barus equation.

2 Fundamental mechanisms of oil consumption and oil transport

In this chapter the essential physics leading to oil consumption shall be closer addressed.

2.1 Global mass balances

Before addressing these mechanisms, the term "oil consumption" is introduced on the basis of gross conservation of the volumetric flow: Since cylinder lubrication is a loss lubrication, all lube oil conducted to the cylinder must finally leave through the discharge valves on head-end side and crank-end side, being the "oil consumption". However, the oil flow through the discharge valves does not need to be strictly periodical: The amount of oil between rings and cylinder wall can differ from period to period, and oil can accumulate next to rings, both resulting in a storage effect and affecting likewise the time dependent outflow. Therefore, the following balance equations are set up using suitable averaged quantities over a sufficient number of crank cycles.

The total oil flow through the discharge valves $\dot{V}_{\mathrm{DV}}^{(\mathrm{oil})}$ reads

$$\dot{V}_{\mathrm{DV}}^{(\mathrm{oil})} = \dot{V}_{\mathrm{DV,HE}}^{(\mathrm{oil})} + \dot{V}_{\mathrm{DV,CE}}^{(\mathrm{oil})} \, , \qquad (2.1)$$

with $\dot{V}_{\mathrm{DV,HE}}^{(\mathrm{oil})}$, $\dot{V}_{\mathrm{DV,CE}}^{(\mathrm{oil})}$ being the oil flow through the discharge valves at head-end side, crank-end side, respectively. A minor share will leave through the packing ($\dot{V}_{\mathrm{pack}}^{(\mathrm{oil})}$) to the intermediate piece of the compressor and will be neglected in the further course. The total volume flow through the packing and through the discharge valves yields the oil consumption, hence the lubricant amount which is fed by the lubrication system:

$$\dot{V}^{(\mathrm{lube})} = \dot{V}_{\mathrm{DV}}^{(\mathrm{oil})} + \dot{V}_{\mathrm{pack}}^{(\mathrm{oil})} \, . \qquad (2.2)$$

An understanding of oil consumption requests a description of the interaction between $\dot{V}^{(\mathrm{lube})}$, $\dot{V}_{\mathrm{DV,HE}}^{(\mathrm{oil})}$ and $\dot{V}_{\mathrm{DV,CE}}^{(\mathrm{oil})}$. Hence, also the oil flow between head-end and crank-end ($\dot{V}_{\mathrm{P}}^{(\mathrm{oil})}$) needs to be understood.

The oil flow leading to oil loss through the discharge valves is described by

- oil film dynamics, describing the free surface oil film along the cylinder, driven by the gas flow. This gas driven oil flow will be referred to as $\dot{V}_{\mathrm{convection}}^{(\mathrm{oil})}$ (see Sec. 3.6).

- oil enrichment effects: The process gas leaving through the discharge valves is enriched with oil due to several effects. Probably the most important are: oil evaporation ($\dot{V}^{(\text{oil})}_{\text{evaporation}}$) and the development of oil mist($\dot{V}^{(\text{oil})}_{\text{oil mist}}$).

- oil transport ($\dot{V}^{(\text{oil})}_{\text{P}}$), describing the oil flow along the piston assembly and effecting the oil film distribution at head-end and crank-end sides;

Hence,

$$\dot{V}^{(\text{oil})}_{\text{DV}} = \dot{V}^{(\text{oil})}_{\text{evaporation}} + \dot{V}^{(\text{oil})}_{\text{oil mist}} + \dot{V}^{(\text{oil})}_{\text{convection}} . \tag{2.3}$$

Oil mist possibly forms in the course of oil injection. Another possibility is the inertial driven formation of oil mist: If oil accumulates on any piston region and forms a large droplet, the piston acceleration due to the piston's reciprocating motion can force a detachment of the oil droplet (throw-off). And third, there is the possibility of vortex formation at the cylinder wall, which could result in oil mist getting away with gas stream.

The evaporation rate can be estimated via evaporation models found in literature (see Sec. 1.4, [40]) and is negligible compared to usual lubrication rates found by compressor manufacturers for most operating conditions. The share of development of oil mist in oil consumption is unknown and is not going to be addressed in the further course of this work. We justify this simplification by assuming a perfect lubrication system and perfect lube conditions (no oil mist due to oil injection, no unnecessary, accumulated oil flow at any grooves, etc.) which might prevent the occurrence of oil mist. However, it is still worth to be subject of future studies.

These definitions lead to the following balance equations describing the oil demand on head-end side ($\dot{V}^{(\text{lube})}_{\text{HE}}$) and crank-end side ($\dot{V}^{(\text{lube})}_{\text{CE}}$):

$$\dot{V}^{(\text{lube})}_{\text{HE}} = \dot{V}^{(\text{oil})}_{\text{P}} + \dot{V}^{(\text{oil})}_{\text{DV,HE}} \tag{2.4a}$$

$$\dot{V}^{(\text{lube})}_{\text{CE}} = -\dot{V}^{(\text{oil})}_{\text{P}} + \dot{V}^{(\text{oil})}_{\text{DV,CE}} + \dot{V}^{(\text{oil})}_{\text{pack}} . \tag{2.4b}$$

A visualization of the main balancing terms is found in Fig. 2.1.

The before mentioned terminology helps to break down the description of oil consumption to three main groups representing different mechanisms, called "transport by lubrication mechanism", "oil film dynamics" and finally "oil enrichment effects". "Oil film dynamics" are discussed in Sec. 3.6. Furthermore, its impact on oil consumption will be estimated in Sec. 6.1. Lots of literature is found describing the "transport by lubrication mechanism". Hence, the next section will give a rough introduction, mentioning the assumptions leading to the problem-describing equations and giving the final equations, which are used in the further course of this work (see Sec. 3.5).
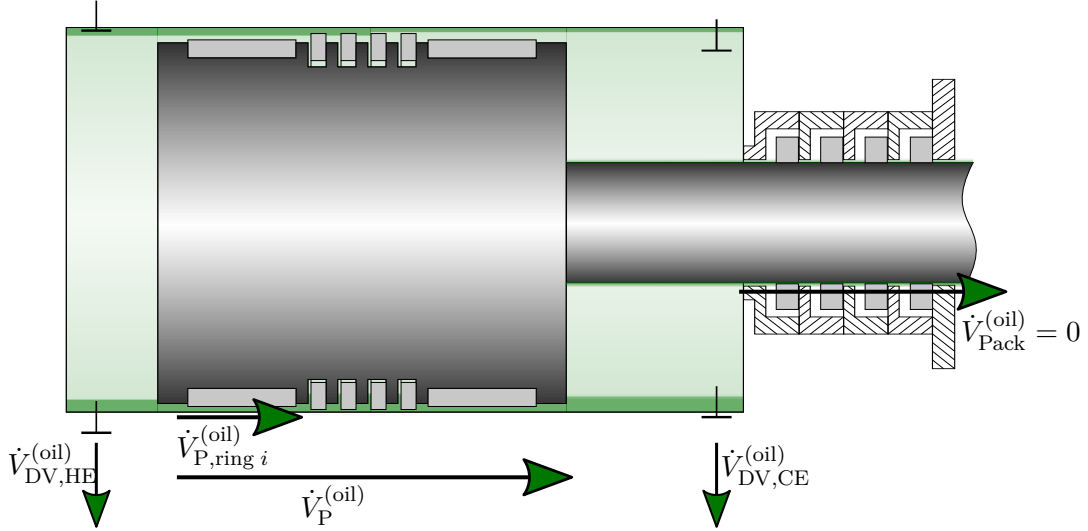
Figure 2.1: Visualization of the main balancing terms leading to oil consumption: $\dot{V}_{\mathrm{DV,HE}}^{(\mathrm{oil})}$ and $\dot{V}_{\mathrm{DV,CE}}^{(\mathrm{oil})}$ are the oil flows through the discharge valves at head-end and crank-end side, respectively, $\dot{V}_{\mathrm{P}}^{(\mathrm{oil})}$ is the oil flow along the piston assembly, and $\dot{V}_{\mathrm{pack}}^{(\mathrm{oil})}$ is the oil flow leaving the cylinder through the packing. All terms are suitably averaged over a sufficient number of crank cycles.

2.2 Transport by lubrication mechanism

The first group "transport by lubrication mechanism" represents the fully lubricated ring areas — the gap between the ring surfaces (rider– and piston rings) and the cylinder wall which is fully flooded with oil. The following properties of this problem allow the use of the classic lubrication theory, which was first studied by Reynolds [46] in 1886:

- The gap to length ratio is $\epsilon_{\mathrm{l}} = H/L \ll 1$ with H and L being the characteristic height and length of the gap.

- The Reynolds number Re times the gap to length ratio is $\epsilon Re \ll 1$, with $Re = U_{\mathrm{c}}H/\nu$ being the Reynolds number formed with the characteristic velocity U_{c} and kinematic oil viscosity ν_{f}.

The fluid is assumed to behave strictly newtonian. Then, exterior mass forces and inertia forces within the lubricant film are negligible, which simplifies the leading thin-layer approximation of the Navier–Stokes equation, resulting in a Couette–Poiseuille velocity profile:

$$u(z,y) = \frac{1}{\mu_{\mathrm{f}}} \frac{\partial p_{\mathrm{oil}}}{\partial x} \left(y^2 - yh \right) + \frac{Uy}{h} , \qquad (2.5a)$$

$$w(z,y) = \frac{1}{\mu_{\mathrm{f}}} \frac{\partial p_{\mathrm{oil}}}{\partial z} \left(y^2 - yh \right) \ , \tag{2.5b}$$

with U being the relative wall velocity. Substituting these velocity profiles in the continuity equation and integrating it across the gap height leads to the well known Reynolds equation [46]. In a Cartesian coordinate system, the classical Reynolds equation for an incompressible fluid takes the form

$$\frac{\partial}{\partial x} \left(\frac{h^3}{6\mu_{\mathrm{f}}} \frac{\partial p_{\mathrm{oil}}}{\partial x} \right) + \frac{\partial}{\partial z} \left(\frac{h^3}{6\mu_{\mathrm{f}}} \frac{\partial p_{\mathrm{oil}}}{\partial z} \right) = U \frac{\partial h}{\partial x} + 2 \frac{\partial h}{\partial t} \tag{2.6}$$

with $\mu_{\mathrm{f}} = \nu_{\mathrm{f}} \cdot \rho_{\mathrm{oil}}$ being the dynamical viscosity of the lube oil, and $h = h(y,z)$ being the gap between the surfaces. This equation can be solved numerically for any given gap distribution, provided proper given boundary conditions. In the simplest form, the pressure is given at the border of the gap (Sommerfeld boundary condition). However, solving the Reynolds equation in consideration of this boundary condition can lead to negative pressures in case of divergent gaps or high squeeze terms, which conflicts with the concept that fluids can not absorb tensile forces. In reality, an instant phase change of the initial liquid lubricant would occur once the pressure falls below the oil's vapour pressure, which is called cavitation. A simple numerical solution is to limit the pressure with the oil's vapour pressure (Gümbel or half-Sommerfeld boundary condition), with the disadvantage of violating the equation of continuity (discontinuous pressure distribution). The Reynolds boundary condition overcomes this issue by additionally requiring zero pressure gradients. These are the simplest possibilities to treat cavitation: The literature on this subject, including also more sophisticated treatments of cavitation, is enormous. Braun and Hannon [9] covered in his review about Cavitation formation and modelling for fluid film bearings extensively different cavitation models.

Calculation of the pressure distribution between rings and cylinder is (1) important since it contributes to the piston forces and consequently affects the motion of the piston and (2) is needed for calculation of the oil transport along the fully lubricated ring. From (2.5a),the volume flow in axial direction is

$$\dot{V}(x,z) = \int_0^h u \, \mathrm{d}y = -\frac{h^3}{6\mu_{\mathrm{f}}} \frac{\partial p_{\mathrm{oil}}}{\partial x} + U \frac{h}{2} \ . \tag{2.7}$$

3 Specific model considerations and simplifications (mesoscale)

This chapter covers model considerations and simplifications on the mesoscale, which are adopted in the numerical model describing the oil film dynamics, leading to a case-dependant derivation of a lube strategy. In the further course of this work, this numerical model will be called global cylinder lubrication model.

3.1 Time scales

Four time scales are identified, which are relevant for the problem description in this work:

1. a lubrication time scale $\tilde{t}_{\mathrm{lub}}$, defined by the injection frequency of the lube system: All state-of-the-art compressor lubrication systems are limited in terms of injection frequency. Usual oil consumption is defined in liter/hour.

2. a global system dynamic time scale, characterized by the primary piston movement: $\tilde{t}_{\mathrm{gl}} \sim 2\tilde{r}_{\mathrm{cd}}/\tilde{u}_{\mathrm{P}} \approx 2\pi/\omega$. This time scale is relevant for the description of the compressor model, in detail explained in Sec. 4 and will be used for a dimensionless formulation of the equations of motion.

3. a boundary time scale, characterized by the slip velocity $\tilde{u}_{\mathrm{s}}$: $\tilde{t}_{\mathrm{bl}} \sim 2\tilde{r}_{\mathrm{cd}}/\tilde{u}_{\mathrm{s}}$, which is relevant for the description of the oil film dynamics in the cylinder region, driven by the gas flow. The slip velocity $\tilde{u}_{\mathrm{s}}$(oil velocity at film surface) needs to be estimated yet (see Sec. 3.6).

4. an acoustic time scale, being relevant for the description of pressure waves travelling through the compression chamber during compression: $\tilde{t}_{\mathrm{ac}} \sim Ma\,\tilde{r}_{\mathrm{cd}}/\tilde{u}_{\mathrm{P}} \approx Ma\frac{\pi}{\omega}$, with $Ma = \tilde{u}_{\mathrm{P}}/\tilde{c}_0, \tilde{c}_0 = \sqrt{\kappa\tilde{p}_0/\tilde{\rho}_0}$. The speed of sound $\tilde{c}_0$ is estimated via the stagnation pressure $\tilde{p}_0$ and stagnation density $\tilde{\rho}_0$. This time scale is relevant for an analytical approach describing the pressure distribution in the compression chamber during compression. Important works covering this topic are: Schneider [47], who studied the change of state of gas in a cylinder during compression in consideration of the perturbation of local speed of sound using the method of characteristics and asymptotic expansion. Wang and Kassoy [53] studied the small-amplitude wave motion using perturbation methods. Klein and Peters [35] show effects of the accumulation of small-amplitude gas-dynamic perturbations at a one-dimensional piston-cylinder, again using the method of asymptotic expansion.

In this work, a CFD-calculation will be done to estimate the pressure gradients and wall shear stresses for an exemplary case (see Sec. 5.2 and Sec. 6.1). The results will show, that the gas-driven oil flow is negligible on the relevant time scale. Therefore, an approach compared to the works mentioned above will not be pursued in this work.

3.2 Net oil flow

The main interest is to estimate the net-oil flow across the rings, which is the suitable averaged oil flow along the rings over a sufficient number of crank cycles ($\dot{V}_{\mathrm{P,ring}\ i}^{(\mathrm{oil})}$ in Sec. 2). The main reason for a non-zero net-oil flow is the secondary piston motion, which is responsible for the symmetry break. The main challenge is that the net-oil flow over one crank cycle ($\Delta \dot{q}_{\mathrm{P,ring}\ i}^{(\mathrm{oil})}$ in Fig. 3.1) is small compared to the oil flow which is transported over one stroke:

$$\dot{V}_{\mathrm{P,ring}\ i}^{(\mathrm{oil})} = \int_{\tau_i}^{\tau_i + 2\pi/\omega} \dot{q}_{\mathrm{P,ring}\ i}^{(\mathrm{oil})}\ \mathrm{d}\tau \ll \int_{\tau_i}^{\tau_i + \pi/\omega} \dot{q}_{\mathrm{P,ring}\ i}^{(\mathrm{oil})}\ \mathrm{d}\tau \tag{3.1}$$

As a consequence it is not possible to neglect a priori elasto-hydrodynamic effects, which have a minor effect on the transported oil flow over one stroke, but could significantly affect the net-oil flow.

A second consequence is the need for special care of conservation of mass. Since the lubrication time-scale is large compared to the global system dynamic time scale, there is the need to estimate the net-oil flow over a large number of crank cycles. Therefore, it is necessary to extrapolate the net-oil flow of a few cycles to get as a result an oil consumption in liter/hour. Small errors can so easily accumulate.
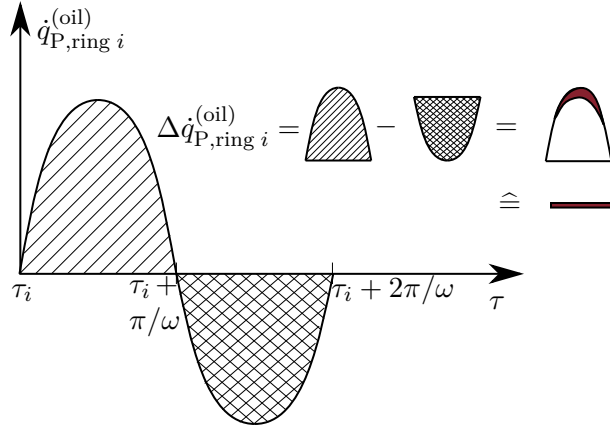

Figure 3.1: Net oil flow vs. transported oil flow over one stroke: The red filled area visualizes the net-oil flow, which is the difference between the oil transported over one stroke to the left and over one stroke to the right side.

3.3 Contact between rings and cylinder wall

The Reynolds equation, which is used to calculate the pressure distribution in fully oil-flooded gaps is valid for ideally smooth contact surfaces. The closer the gap's height is to the cylinder wall roughness, the more inaccurate the Reynolds equation gets and the surface roughness plays an increasing role. Finally, with gap's height being the same size as the surface roughness, the ring operates in the mixed lubrication regime, where the load is supported partly by the fluid film and partly by the surface asperities. To get a more realistic representation of oil flow at small gap heights, averaging techniques can be applied, leading to modified Reynolds equations (e.g. homogenization (e.g. Bayada and Faure [5]) and flow factor method by Patir and Cheng [44]). A short comparison of these two techniques can be found in Almqvist et al. [2]. Both averaging techniques require detailed knowledge of the exact structure of the wall roughness. However, this information is missing for most compressors and varies from machine to machine.

In this work, the influence of wall roughness on the pressure distribution is neglected, assuming perfectly smooth surfaces. However, the gap is limited to a minimal gap in the order of the cylinder surface roughness to eliminate non-physically small gaps. This is done by linear spring forces, which are independent from each other. They are applied to the ring surface and represent contact forces due to elastic deformation:

$$F_{c,k} = EA_{c,k} \frac{\text{gap}_{\text{min}} - \text{gap}_k}{h} \; , \tag{3.2}$$

with $A_{c,k}$ being a proportional section area, E being the Young's modulus, and h being the height of the deforming material. The evolution of wear is negligible on the time scale of a few revolutions and is therefore not accounted for. Changed ring profiles due to long-term wear can of course affect the global system behaviour and are to be defined initially. Hence, we do not use a more sophisticated approach to model the asperity contact (e.g. [24]) for getting a more realistic stress distribution, which would be needed for an accurate wear model. The approach in (3.2) is chosen, because (1) it gives a rough estimate for the resulting moment due to the contact forces, which should be accounted for, and (2) allows to track the forces due to asperity contacts between rings and cylinder counter faces. These are used to assess the condition of lubrication for each ring do to get an indication for under-lubrication: Commonly refereed to as Archard's equation of adhesive wear, the volume of wear being worn away (V_w) is proportional to the applied load W, the sliding distance x, the hardness H of the surface being worn away and the non-dimensional wear coefficient k, which is dependent on the materials in contact, the operating conditions and their cleanness [28]:

$$V_w = \frac{kWx}{H} \; . \tag{3.3}$$

This equation can be rewritten as

$$\dot{d} = \frac{kpv}{H} \; , \tag{3.4}$$

where $\dot{d}$ is the rate of wear depth and p is the apparent pressure. The rate of wear is proportional to the pv factor, which is generally used in the selection of materials for dry bearings [6] as well as for dry rider– and piston rings. Hence, the pv-load is tracked for each ring, resulting in a starving coefficient St ranging from 0–1: The pv load is integrated over each revolution, assuming a zero wear-contribution at hydrodynamic lubrication conditions and divided by the "virtual", integrated pv load of an assumed dry running ring. The limit $St = 1$ corresponds to the rate of wear of a dry-running ring, while $St = 0$ for a ring, fully running in the hydrodynamic lubrication regime. The piston– and rider rings are treated differently: In case of the rider rings, it is assumed that the piston force is transmitted to the piston via a constant apparent area, which is assumed to be the same for the dry running ring as well as for the lubricated ring. Using the Heaviside step function

$$H(x) = \begin{cases} 0 & \text{if } x < 0 \\ 1 & \text{else ,} \end{cases}$$

St is defined for each rider ring i as

$$St_{,i} = \frac{\int\limits_{\tau_i}^{\tau_i+2\pi/\omega} F_{\mathrm{P,y,sub},i}\, U H(\sum\limits_k F_k)\, \mathrm{d}\tau}{\int\limits_{\tau_i}^{\tau_i+2\pi/\omega} F_{\mathrm{P,y,sub},i}\, U\, \mathrm{d}\tau} \ . \tag{3.5}$$

For the piston ring's starving parameter, on the other hand, St is calculated for each layer of ϕ, and then summed up over all layers:

$$St_{,i} = \sum_{\phi} \frac{\int\limits_{\tau_i}^{\tau_i+2\pi/\omega} p_i U H(\sum\limits_k F_k)\, \mathrm{d}\tau}{\int\limits_{\tau_i}^{\tau_i+2\pi/\omega} p_i U\, \mathrm{d}\tau} \ . \tag{3.6}$$

In this case, k is the index describing all values for each layer, and p_i is the maximal gas pressure acting on the ring: Each layer contributes to St as soon as any contact force of this layer $F_k > 0$.

3.4 Wetting angle

To get the oil transport from one to the other side of the piston it is important to think three-dimensional (see Fig. 3.3): The clearance ($\gtrsim 0.1\,\mathrm{mm}$) is relatively high compared to typical oil film heights ($\lesssim 0.01\,\mathrm{mm}$). Therefore, under usual operation conditions, the gap between ring and cylinder will not completely be filled with oil and there will be regions, where this gap is larger than the film height, in the further course of this work called "starved regions". In these regions, the
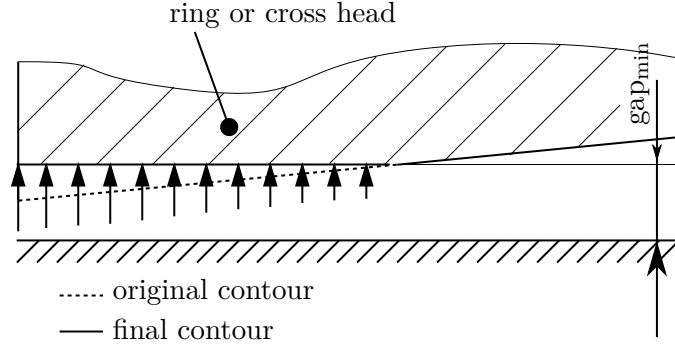
Figure 3.2: Contact formulation used in the rigid formulation.

ring will be stressed solely by the gas pressure p_{gas}. The oil film in these regions is assumed to cover the cylinder wall and is passive: its film height is independent of the piston movement. We introduce the term "wetting angle" ϕ_{w}, which defines the expansion of the fully flooded ring area in azimuthal direction. The wetting angle $\theta = \theta(z, \tau)$ is a priori not known and is part of the results. It has a great impact on the results, both on the pressure distribution, and subsequently on the oil flow and piston movement. Therefore, it is important to take the oil film distribution, both in axial and azimuthal direction into account. However, if (1) the wetting angle is sufficiently large and the fully filled area reaches up to the point, where no oil pressure builds up and (2) the gradients in azimuthal directions are negligible ($\frac{1}{r}\frac{\partial}{\partial \phi} \ll \frac{\partial}{\partial z}$), it is possible to do a quasi 1D calculation. This is done for all oil transport calculations in the cylinder region in this work (the pressure distribution along the crosshead is calculated using the 2D Reynolds equation): The 1D Reynolds equation is used to calculate oil pressure distributions between fully flooded rings and cylinder. The oil flow in azimuthal direction is neglected. Especially the simplification of the Reynolds equation reduces significantly calculation time. ϕ is now just a parameter. All calculations are done for a set of ϕ, ranging from 0–π.

While condition (2) is certainly fulfilled due to the problem's geometry, condition (1) can be violated partly, especially shortly before the event of mixed contact between rings and cylinder if ϕ_{w} approaches zero. While the axial fluid velocities will clearly dominate, independently from ϕ_{w} due to the axial motion of the piston, the error in the calculation of the pressure distribution might be considerably. Hence, the oil flow in azimuthal direction will be neglected[1], but results need to be interpreted with care for small ϕ_{w}. Figure 3.3 shows an azimuthal section of a piston moving in a cylinder. In the next section, we will take a look at the conditions in axial direction.

---

[1] Gehannin et al. [22] studied in her work air ingestion in squeeze film dampers using the VOF-method. Among others, she concluded that a 2D model and a simplified 1D model give the same results because of the minor role of the circumferential velocities.
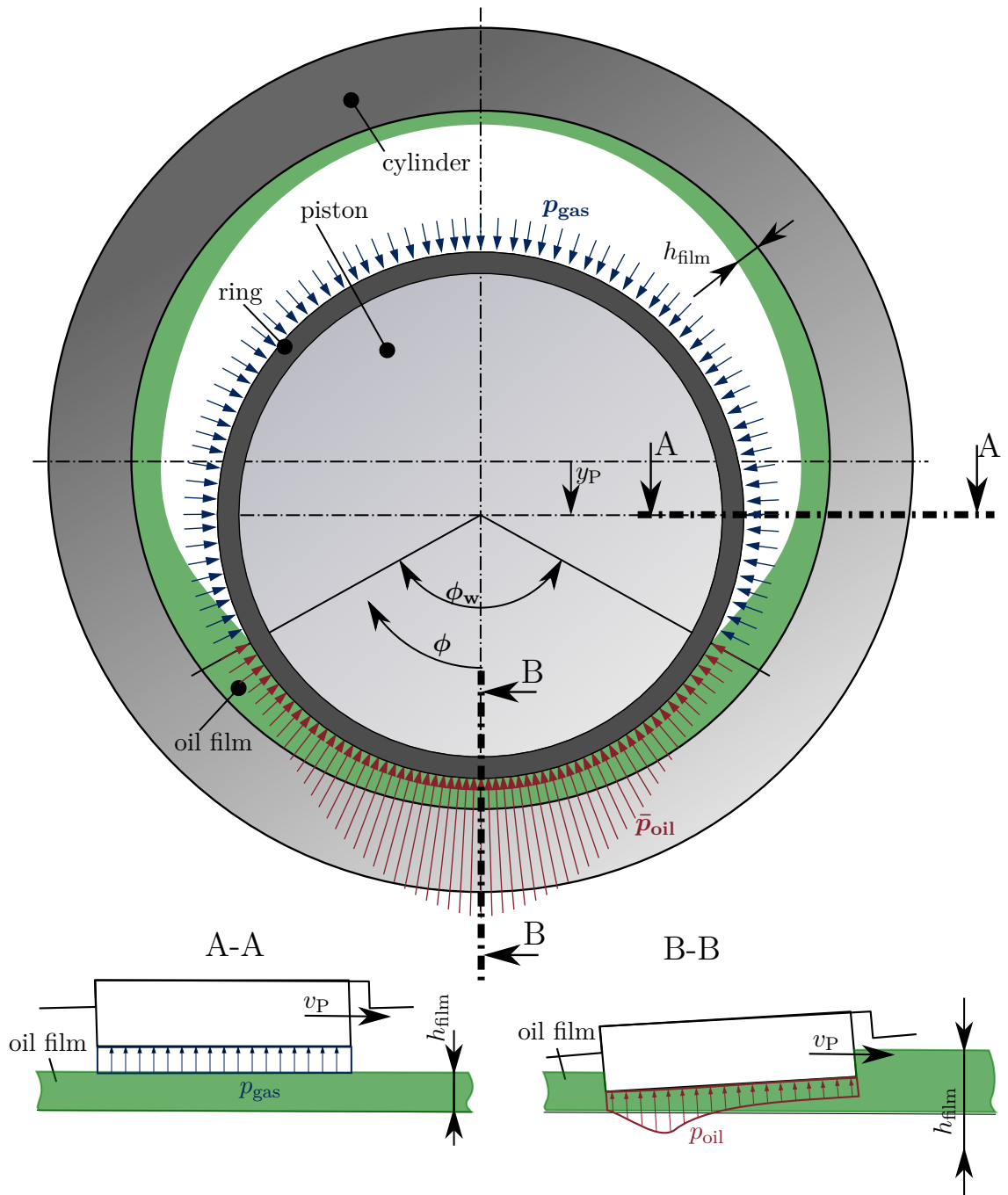
Figure 3.3: Explanation of wetting angle $\phi_{\mathrm{w}} = \phi_{\mathrm{w}}(x, \tau)$.

3.5 Calculation regimes

Oil film dynamics are modeled by dividing the calculation domain in different calculation areas (see Fig. 3.4):

- oil film in cylinder regions

- "outer" transition zone

- "inner" transition zone

- fully flooded ring region

- starved ring region

Both rider– and piston rings are handled the same, therefore no distinction is made between these ring in the further course of this section.

The transition zones are used to describe the transitions between fully flooded regions and passive regions (cylinder film and starved ring region). The highly complex physical behaviour in these regions is not modelled, they are treated like black boxes, focusing on correct mass balances (see next sections). This approach is motivated by the geometry of such a "black box": The transition between two regions will have a meniscus form in the size of the gap height. Since gap heights are typically approx. $0.01\,\mathrm{mm}$, and the length of a black box is typically approx. $0.1\,\mathrm{mm}$, this approach is motivated by the assumption that the borders of the "black box" are far enough away from the meniscus, showing an undisturbed, known flow field.

Two coordinate systems are used: The oil film in the cylinder region outside the ring regions is described in the inertial system, while the ring regions including the transition zones are described in a system moving with piston velocity v_{P}.
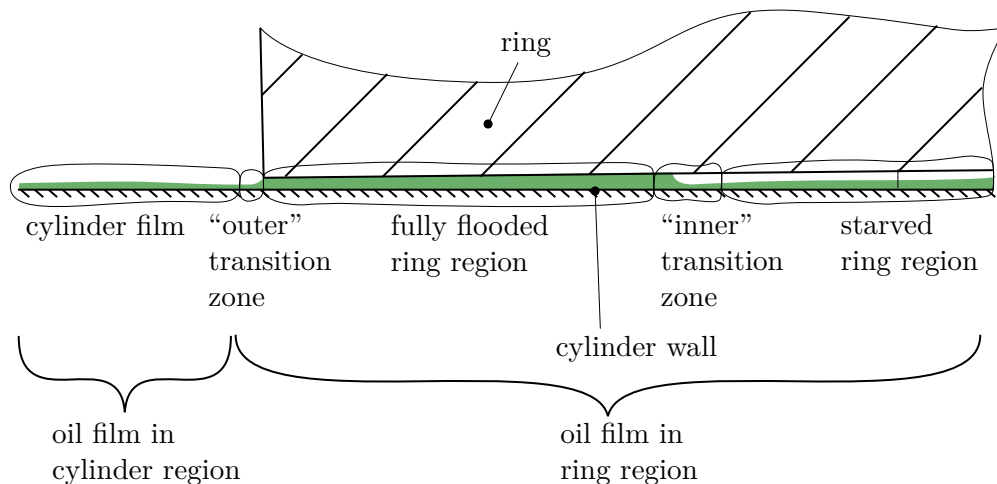
Figure 3.4: Definiton of calculation regimes;

3.5.1 Fully flooded ring regions

The 1D Reynolds equation is used to derive the oil transport along the ring regions:

$$\frac{\partial}{\partial x}\left(\frac{h^3}{6\mu_{\mathrm{f}}}\frac{\partial p_{\mathrm{oil}}}{\partial x}\right) = U\frac{\partial h}{\partial x} + 2\frac{\partial h}{\partial t}\;, \tag{3.7}$$

with U being the relative velocity of the separated surfaces, μ_{f} being the dynamical viscosity of the lube oil, and $h = h(x,z)$ being the gap between the surfaces. The oil is assumed to behave strictly newtonian, its viscosity and density are assumed to be uniform over the cylinder's surface and over the film thickness. The dependency of the oil's viscosity on pressure is neglected, since gas pressures approximately range from 1–300 bar, dependent on the machine and application with typical compression ratios of three. Hence, the viscosity-pressure dependency of typical lubrication oils is relatively low (see Fig. 1.10). Substantially more important is the viscosity-temperature dependency: However, detailed knowledge about the temperature distribution on the cylinders wall over time does not exist. Therefore, an average oil temperature needs to be guessed, taking this temperature as a reference for an oil viscosity assumption.

Unless otherwise stated, these simplification are used throughout this work, although they could easily be modified: The Reynolds equation can be extended to a 2D formulation (as it is necessary for the crosshead submodel), though this expansion would significantly increase calculation time. Viscosity dependency on temperature and pressure could easily be taken into account, if detailed information would be available.

Both sides of a fully flooded ring region are free boundaries, which need to be tracked. There, the oil pressure is prescribed and equals the gas pressure. Above all, the half-Sommerfeld condition is used, the pressure is limited with the oil's evaporation pressure. Other conditions would be more exact, however, in many applications, the gas pressure defining the boundary pressure is well above ambient pressure, limiting the possibility of cavitation. Therefore, a simple "cavitation" condition is used and considered to be sufficient.

Hirt and Nichols [32] have introduced the volume-of-fluid method (VOF) for capturing the free boundary of an incompressible liquid, using a piece-wise constant "stair stepped" approximation of the interface geometry: Each computational cell is described by a function F which describes the volume fraction of liquid and is defined as

$$F = \frac{V_{\mathrm{oil}}}{V}\;, \tag{3.8}$$

V_{oil} being the volume of lubricant in a specific cell and V being the total cell volume, both are values per unit depth. F is governed by the transport equation

$$\frac{\partial F}{\partial t} + \nabla \cdot (\boldsymbol{u}F) = 0\;. \tag{3.9}$$

Equation (3.9) (slightly modified due to numerical issues) is integrated over the cell height h by assuming a constant volume fraction F over the film thickness and then discretized using the finite volume method leading to a conditional equation for F. The transferred lubricant across cell borders is a function of the flow field and of the distribution of the volume fraction, but always under the assumption, that the volume fraction is constant over the film thickness.

However, this assumption is not valid in this work. Therefore, we introduce the transition zone for cases of "starved lubrication", when the gap between ring and cylinder is not fully flooded : This zone is between the passive oil film, which is assumed to cover the cylinder wall and the fully flooded ring region (see Fig. 3.4). Following the VOF-method, the interface tracking will be done using the volume fraction F. F represents the proportion of the fully filled cell volume on the total cell volume, ignoring the passive oil film. The position of the interface is dependent on the volume fractions of the interface- and the neighbour cells: The fully lubricated side of the interface cell is always on the side of the fully flooded ring zone (see Fig. 3.5).
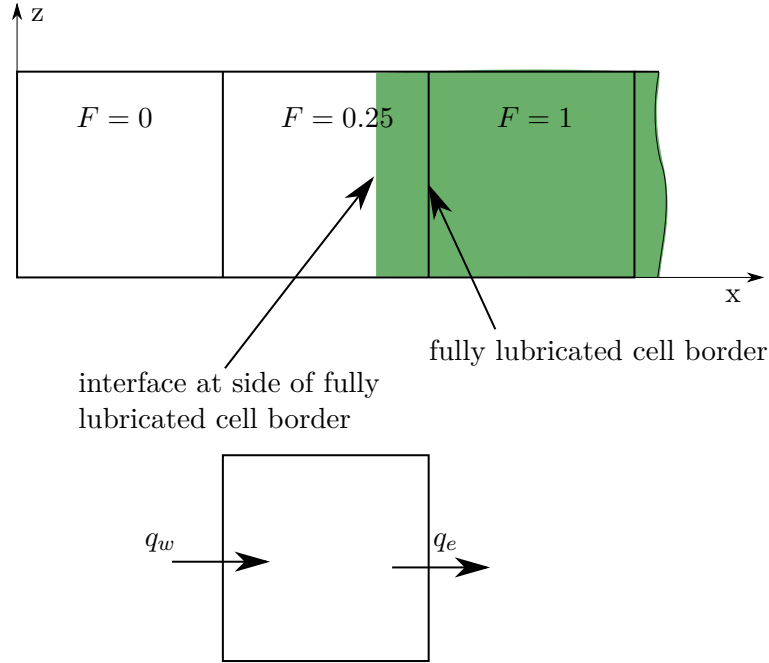
Figure 3.5: Upper figure: The position of the interface is dependent on the volume fractions of the interface- and the neighbor cells. Lower figure: volume flows of lubricant in interface cell.

The evolution of F is derived by a mass balance for the interface cell with index k

$$V_{\text{oil},k}^{(n)} = V_{\text{oil},k}^{(n-1)} + q_w^{(n)} - q_e^{(n)} \tag{3.10}$$

31

resulting in

$$F_k^{(n)} = F_k^{(n-1)} \frac{V_k^{(n-1)}}{V_k^{(n)}} + \frac{q_w^{(n)} - q_e^{(n)}}{V_k^{(n)}} \ .$$ (3.11)

The superscript (n-1) denotes the previous time step, and (n) denotes the current time step. As mentioned in Sec. 3.4, the interface tracking will be done neglecting the flow field in azimuthal direction. The treatment of the starved ring zone as well as the transition zones including the definitions of the oil flows (per unit depth) q_w and q_e will be explained in the next section.

3.5.2 Starved ring zone and transition zones

Starved ring zone: In the starved ring zone, the cylinder's wall is covered by an oil film at rest in the inertial coordinate system. Since this zone is described in a coordinate system moving with piston velocity v_P, the advection equation needs to be solved for the film height:

$$\frac{\partial h_{\text{film}}}{\partial t} - v_P \frac{\partial h_{\text{film}}}{\partial x} = 0$$ (3.12)

Inner transition zone: The inner transition zone describes the oil flow between the fully flooded and the starved ring region. Figure 3.6 shows an inner transition zone for an open boundary on the right side of the fully flooded zone being in cell i. It does not picture a physically reasonable meniscus, but already shows a discretized calculation area. In "real", the length to height ratio of a numerical transition zone cell is $\approx 10 \times 1$.
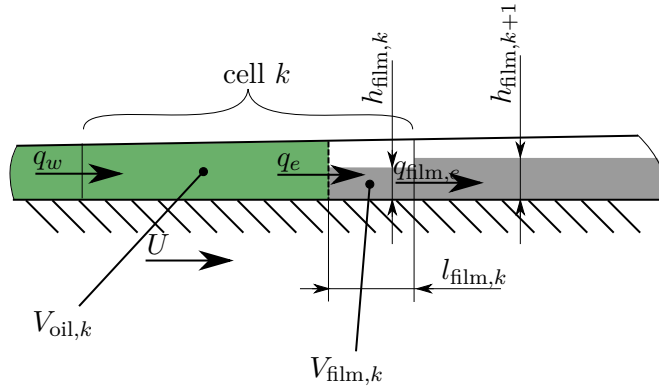
Figure 3.6: Schema of "inner" transition zone;

Taking a right-sided transition zone as pictured in Fig. 3.6 as an example, the oil flow per unit depth in axial direction q_w, calculated with the oil flow rate rate

integrated over a finite time increment $\Delta t = t^n - t^{n-1}$, is described by the Poisson-Couette profile resulting from lubrication theory (1D Reynolds equation). It describes the oil flow due to pressure gradients and relative wall velocities (wedge and squeeze mechanisms), limited by the available oil volume upstream:

$$q_w = \int\limits_{t^{n-1}}^{t^n} \int\limits_0^h v \, \mathrm{d}y \, \mathrm{d}t \approx \min\left[V_{\text{oil},k-1}, \left(-\frac{1}{12\mu_{\text{f}}}\frac{\partial p}{\partial x} + U\frac{h}{2} \right)\bigg|_w^{(n)} \Delta t \right] . \qquad (3.13)$$

A velocity-depending distinction must be made for the definition of q_e, which is describing the oil transport between passive oil film and fully flooded ring region: The case of negative cylinder velocity is intuitively easy to describe: The passive oil film must feed the fully lubricated gap. Hence, q_e is described by means of a constant velocity profile.

The other case (positive cylinder velocity) is not as clear, there is the question, what kind of trace the moving ring is leaving behind the fully lubricated zone: One limit would be a transition zone at rest, leaving a trace whose height h is defined by q_w:

$$h_{\text{film},k} = \frac{q_w}{U\,\Delta t} .$$

The other limit case would be "no trace", the transition zone would move as fast as mass conservation allows, as it would for an inviscid fluid with slipping wall condition at the cylinder wall:

$$q_e = 0 .$$

In this work, it is assumed that the trailing edge is only moving due to squeeze and wedge related oil flows. Hence,

$$q_e = U\frac{h_k}{2}\Delta t . \qquad (3.14)$$

This assumption is partly supported by CFD-calculations[2], but in reality the relations are much more complicated and require additional research.

Summarized, the right-sided oil transport between passive oil film and fully is defined as follows:

$$q_e = h_{\text{film},k}U\Delta t \qquad\qquad \text{for } U < 0 , \qquad (3.15a)$$

$$q_e = U\frac{h_k}{2}\Delta t \qquad\qquad \text{else} . \qquad (3.15b)$$

If the interface cell is on the left side of the fully lubricated gap, everything is vice versa.

Last but not least, the oil flow q_{film} needs to be defined. It is dependent on the

---

[2]documented in internal memo by ©HOERBIGER R&D

cylinder velocity:

$$q_{\text{film}} = h_{\text{film},k+1} U \Delta t \qquad \text{for } U < 0 \ , \qquad (3.16a)$$

$$q_{\text{film}} = h_{\text{film},k} U \Delta t \qquad \text{else} \ . \qquad (3.16b)$$

Outer transition zone: If the oil film upstream of a ring is above a certain height, a defined amount of oil will be transported along the ring (given by lubrication theory), but any additional oil will accumulate at the ring's border, forming a meniscus. On the other hand, if such a meniscus exists downstream of the ring, it will first degrade, until the ring leaves a trace given by mass conservation.

The focus of the outer transition zone-formulation in this work lies on conservation of mass. Oil must not get lost. However, slight imprecisions in the calculation of the oil film height in the cylinder region are acceptable. Therefore, the exact shape, growth and degradation of the meniscus is not researched. Instead, the menisci are thought of rectangular shaped columns with constant velocity profiles at the outer sides, dependent on the cylinder wall velocity. They are called transition zones to emphasize this approach. The volume flow from the outer transition zone to the ring zone is dependent on the oil film heights of both sides of the border: In case the ring gap is fully flooded, and the oil column can provide enough oil, the volume is defined by the velocity profile given by the Reynolds equation. Otherwise, it is defined by the oil column's height assuming a constant velocity. For an explanation in detail see Fig. 3.8 for a transition zone downstream of a ring, and Fig. 3.9–3.10 for a transition zone upstream of a ring, including necessary distinctions of cases. In Fig. 3.7, the nomenclature concerning the outer transition zone is given.
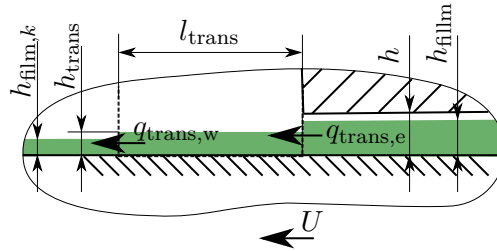
Figure 3.7: Length- and height definitions concerning the outer transition zone;

fully flooded ring region: **starved ring region:**
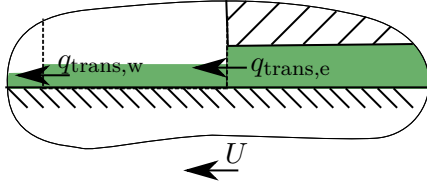
$$q_{\text{trans,e}} = \left(-\frac{1}{12\mu_{\text{f}}} \frac{\partial p}{\partial x} + U\frac{h}{2} \right) \Delta t \qquad\qquad q_{\text{trans,e}} = Uh_{\text{film}}\Delta t$$
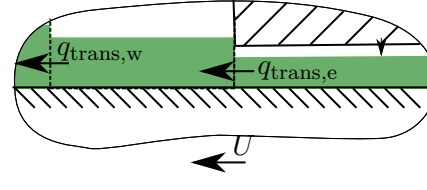
$$q_{\text{trans,w}} = Uh_{\text{trans}}\Delta t \qquad\qquad\qquad\qquad q_{\text{trans,w}} = Uh_{\text{trans}}\Delta t$$

Figure 3.8: Schema of downstream transition zone;

fully flooded ring region,
$h_{\text{trans}} < h$**:**
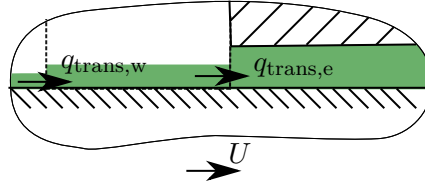
$$q_{\text{trans,e}} = \min\left[Uh_{\text{trans}}, \left(-\frac{1}{12\mu_{\text{f}}} \frac{\partial p}{\partial x} + U\frac{h}{2} \right) \right] \Delta t$$

$$q_{\text{trans,w}} = Uh_{\text{film},k}\Delta t$$

Figure 3.9: Schema of upstream transition zone;

starved ring region,   **starved ring region,**
$h_{\text{trans}} < h$**:** $h_{\text{trans}} \geq h$**:**
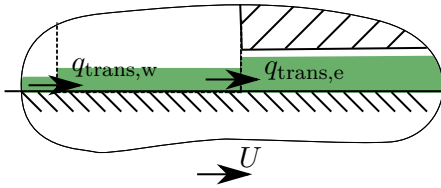
$$q_{\text{trans,e}} = Uh_{\text{trans}}\Delta t \qquad\qquad q_{\text{trans,e}} = Uh\Delta t$$
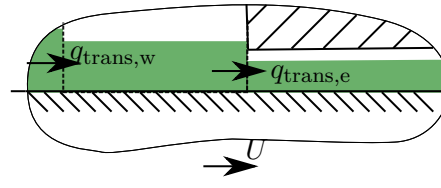
$$q_{\text{trans,w}} = Uh_{\text{film},k}\Delta t \qquad\qquad q_{\text{trans,w}} = Uh_{\text{film},k}\Delta t$$

Figure 3.10: Schema of upstream transition zone;

35

3.6 Oil film in cylinder region: thin film approximation

So far we have discussed the film regions between rings and cylinder wall. What is left, is the oil film in the cylinder region. In this section, the oil film dynamics in this regions shall be discussed and its dependency on gas flow[3]. The "~"-Symbol is used in a twofold meaning: it is used conventionally, i.e. to describe asymptotic relations, and in the sense of order-of-magnitude relations; the usage will become clear from the specific context. Furthermore, all dimensioned quantities will be marked by a tilde.

3.6.1 Estimates for gas-driven film equation

Three main assumptions are used to derive the film equations:

- The boundary layer thickness $\tilde{\delta}$ is large compared to $\tilde{H}_\mathrm{f}$, being a representative oil film height: $\tilde{\delta} \sim \tilde{r}_\mathrm{cd}/\sqrt{\mathrm{Re}_\mathrm{g}} \gg \tilde{H}_\mathrm{f}$

- the oil density $\tilde{\rho}_\mathrm{f}$ is large compared to the gas density $\tilde{\rho}_\mathrm{g}$: $\tilde{\rho}_\mathrm{f}/\tilde{\rho}_\mathrm{g} \gg 1$

- the dynamic oil viscosity $\tilde{\mu}_\mathrm{f}$ is large compared to the dynamic gas viscosity $\tilde{\mu}_\mathrm{g}$: $\tilde{\mu}_\mathrm{f}/\tilde{\mu}_\mathrm{g} \gg 1$

From the Euler equation governing the quasi-1D gas flow in the compression chamber

$$\tilde{\rho}_\mathrm{g} \left(\tilde{u}_t + \tilde{u}\tilde{u}_x \right) \sim -\tilde{p}_x \tag{3.17}$$

follows

$$-\tilde{p}_x \sim \tilde{\rho}_\mathrm{g}\tilde{u}_t \sim \tilde{\rho}_\mathrm{g}\ddot{\tilde{x}}_\mathrm{C}(t) \sim \tilde{\rho}_\mathrm{g}\tilde{\omega}^2\tilde{r}_\mathrm{cd}\frac{2}{\pi^2} \;. \tag{3.18}$$

In the boundary layer, the estimates

$$\tilde{\rho}_\mathrm{g} \left(\tilde{u}_t + \tilde{u}\tilde{u}_x \right) \sim -\tilde{p}_x + \tilde{\mu}_\mathrm{g}\tilde{u}_{yy}$$
$$\tilde{u} \sim \tilde{u}_\mathrm{P}, \; \tilde{y} \sim \frac{\tilde{r}_\mathrm{cd}}{\sqrt{\mathrm{Re}_\mathrm{g}}}, \; \tilde{t} \sim \frac{\tilde{r}_\mathrm{cd}}{\tilde{u}_\mathrm{P}}; \tag{3.19}$$

hold accordingly; hence,

$$\tilde{\rho}_\mathrm{g}\tilde{u}_t \sim \tilde{\mu}_\mathrm{g}\tilde{u}_{yy} \sim \tilde{\mu}_\mathrm{g}\frac{\tilde{u}_\mathrm{P}}{\tilde{\delta}^2} \;. \tag{3.20}$$

Similarly, we get for the oil film

$$\tilde{\rho}_\mathrm{f} \left(\tilde{u}_t + \tilde{u}\tilde{u}_x \right) \sim -\tilde{p}_x + \tilde{\mu}_\mathrm{f}\tilde{u}_{yy}$$
$$\tilde{u} \sim \tilde{u}_\mathrm{s}, \; y \sim \tilde{H}_\mathrm{f}, \; \tilde{t} \sim \frac{\tilde{r}_\mathrm{cd}}{\tilde{u}_\mathrm{P}}, \; \tilde{u}_t \sim \tilde{u}_\mathrm{s}\frac{\tilde{u}_\mathrm{P}}{\tilde{r}_\mathrm{cd}}, \; \tilde{u}\tilde{u}_x = \frac{\tilde{u}_\mathrm{s}^2}{\tilde{r}_\mathrm{cd}}, \tag{3.21}$$

and

$$\tilde{\rho}_\mathrm{f}\tilde{u}_t \sim \tilde{\mu}_\mathrm{f}\tilde{u}_{yy} \sim \tilde{\mu}_\mathrm{f}\frac{\tilde{u}_\mathrm{s}}{\tilde{H}_\mathrm{f}^2} \;. \tag{3.22}$$

---

[3]the following estimates were derived in a fruitful discussion with supervisor B. Scheichl.

These expressions are used for an estimation of order of magnitudes for the slip velocity $\tilde{u}_s$ and for the terms of the Navier–Stokes equation to derive simplified film equations, which describe the oil film dynamics in the cylinder region. It is unclear, if the estimate $\tilde{u}_s \sim \tilde{u}_P$ holds, or if $\tilde{u}_s \ll \tilde{u}_P$. The answer to this question has a great impact on the equations covering the oil film dynamics in the cylinder region.

Assumption 1: The slip velocity has the same order of magnitude as the piston velocity: $\tilde{u}_s \sim \tilde{u}_P$. Reformulating the diffusion term in (3.21), we get a correlation between $\tilde{H}_f, \tilde{\delta}, \tilde{\nu}_f, \tilde{\nu}_g$:

$$\tilde{\mu}_f \frac{\tilde{u}_s}{\tilde{H}_f^2} \sim \underbrace{\tilde{\mu}_f \frac{\tilde{u}_P}{\tilde{H}_f^2}}_{\sim \tilde{\rho}_f \tilde{u}_t} \sim \underbrace{\sim \tilde{\mu}_g \frac{\tilde{u}_P}{\tilde{\delta}^2}}_{\tilde{\rho}_g \tilde{u}_t} \underbrace{\frac{\tilde{\mu}_f}{\tilde{\mu}_g}}_{\gg 1} \underbrace{\left(\frac{\tilde{\delta}}{\tilde{H}_f}\right)^2}_{\gg 1}$$

$$\Rightarrow \frac{\tilde{\rho}_f}{\tilde{\rho}_g} \sim \frac{\tilde{\mu}_f}{\tilde{\mu}_g} \left(\frac{\tilde{\delta}}{\tilde{H}_f}\right)^2$$

$$\Rightarrow \frac{\tilde{H}_f}{\tilde{\delta}} \sim \sqrt{\frac{\tilde{\nu}_f}{\tilde{\nu}_g}} \tag{3.23}$$

However, for usual kinematic viscosities for oil and gas the last expression leads to an inconsistency, since

$$\frac{\tilde{\delta}}{\tilde{H}_f} \sqrt{\frac{\tilde{\nu}_f}{\tilde{\nu}_g}} \neq \mathcal{O}(1) . \tag{3.24}$$

Therefore, the assumption $\tilde{u}_s \sim \tilde{u}_P$ is not valid, which leads to an alternative estimation for $\tilde{u}_s$:

Assumption 2: The slip velocity is small compared to the piston velocity: $\tilde{u}_s \ll \tilde{u}_P$. Taking the dynamic boundary condition at the interface oil-gas into account: $\tilde{\tau}_f|_{i-} \sim \tilde{\tau}_g|_{i+}$, $\tilde{\tau}_f$ and $\tilde{\tau}_g$ being the shear stress in the fluid and gas phase, respectively, and accounting for $\tilde{\delta} \gg \tilde{H}_f$, we get

$$\tilde{\mu}_f \left.\frac{\partial \tilde{u}}{\partial \tilde{y}}\right|_{i-,f} = \tilde{\mu}_g \left.\frac{\partial \tilde{u}}{\partial \tilde{y}}\right|_{i+,g}$$

$$\Rightarrow \tilde{\mu}_f \frac{\tilde{u}_s}{\tilde{H}_f} \sim \tilde{\mu}_g \frac{\tilde{u}_P}{\tilde{\delta}} ,$$

$$\Rightarrow \underbrace{\frac{\tilde{\mu}_f}{\tilde{\mu}_g}}_{\gg 1} \underbrace{\frac{\tilde{\delta}}{\tilde{H}_f}}_{\gg 1} \sim \frac{\tilde{u}_P}{\tilde{u}_s} ,$$

$$\Rightarrow \tilde{u}_s \ll \tilde{u}_P . \tag{3.25}$$

Thus, the assumption $\tilde{u}_\text{s} \ll \tilde{u}_\text{P}$ proves to be the correct one. Taking again the dynamic boundary condition at the interface oil-gas $\tilde{\tau}_\text{f}|_{i-} \sim \tilde{\tau}_\text{g}|_{i+}$ into account and account for $\tilde{\delta} \gg \tilde{H}_\text{f}$ yields

$$\tilde{\tau}_\text{f}|_{i-} \sim \tilde{\tau}_\text{g}|_{i+} \Rightarrow \frac{\partial \tilde{\tau}_\text{f}}{\partial \tilde{y}} \sim \frac{\tilde{\tau}_\text{f}}{\tilde{H}_\text{f}} \gg \frac{\partial \tilde{\tau}_\text{g}}{\partial \tilde{y}} \sim \frac{\tilde{\tau}_\text{g}}{\tilde{\delta}} \sim \tilde{p}_x \ , \tag{3.26a}$$

$$\Rightarrow \frac{\partial \tilde{\tau}_\text{f}}{\partial \tilde{y}} \gg \tilde{p}_x \ . \tag{3.26b}$$

This is an important result, showing that the shear stress is the dominant term in the Navier–Stokes equation of the oil film and leading to the neglect of the pressure gradient.

These estimations lead to the simplified film equation

$$\tilde{\rho}_\text{f} \frac{\partial \tilde{u}}{\partial \tilde{t}} = \tilde{\mu}_\text{f} \frac{\partial^2 \tilde{u}}{\partial \tilde{y}^2} \ , \tag{3.27}$$

or in the dimensionless form

$$\frac{\partial u}{\partial t} = \frac{1}{Re_\text{f}} \frac{\tilde{r}_\text{cd}}{\tilde{H}_\text{f}} \frac{\partial^2 u}{\partial y^2} \ , \tag{3.28}$$

with

$$(\tilde{y}, \tilde{h}_\text{film}) = (y, h) \cdot \tilde{H}_\text{f} \ , \quad \tilde{x} = x \tilde{r}_\text{cd} \ , \quad \tilde{t} = t \frac{\tilde{r}_\text{cd}}{\tilde{u}_\text{P}} \ ,$$
$$\tilde{\tau}_\text{g} = \tilde{\mu}_\text{g} \frac{\tilde{u}_\text{P}}{\tilde{\delta}} \tau_\text{g} \ , \tag{3.29}$$

and

$$Re_\text{f} = \frac{\tilde{H}_\text{f} \tilde{u}_\text{P}}{\tilde{\nu}_\text{f}} \ , Re_\text{f} = \mathscr{O}(1). \tag{3.30}$$

For small film heights ($\tilde{H}_\text{f} \sim 1 \times 10^{-5}$), the momentum equation reduces to

$$0 = \frac{\partial^2 \tilde{u}}{\partial \tilde{y}^2} \ . \tag{3.31}$$

The boundary and interface conditions to be imposed are:

- kinematic conditions: no slip at $\tilde{y} = 0$:

$$\tilde{u} = \tilde{v} = 0 \tag{3.32}$$

- dynamic condition: continuity of tangential stress at the interface $\tilde{y} = \tilde{h}_\text{film}(\tilde{x}, \tilde{t})$, with $\tilde{\tau}_\text{g} = \tilde{\mu}_\text{g} (\partial \tilde{u}/\partial \tilde{y})_\text{gas}$:

$$\tilde{\mu}_\text{f} \left(\frac{\partial \tilde{u}}{\partial \tilde{y}} \right)_\text{oil} = \tilde{\tau}_\text{g} \ ; \tag{3.33a}$$

$$\tilde{p}_{\mathrm{f}} \approx \tilde{p}_{\mathrm{g}} \; ; \tag{3.33b}$$

- kinematic condition:

$$\tilde{v} = \frac{\partial \tilde{h}_{\mathrm{film}}}{\partial \tilde{t}} + \tilde{u}\frac{\partial \tilde{h}_{\mathrm{film}}}{\partial \tilde{x}} \; . \tag{3.34}$$

Integration of Continuity Equation over film height leads to

$$\int_0^{\tilde{h}_{\mathrm{film}}(\tilde{x})} \frac{\partial \tilde{u}}{\partial \tilde{x}}\,\mathrm{d}\tilde{y} + \int_0^{\tilde{h}_{\mathrm{film}}(\tilde{x})} \frac{\partial \tilde{v}}{\partial \tilde{y}}\,\mathrm{d}\tilde{y} = ... =$$

$$\frac{\partial \tilde{h}_{\mathrm{film}}}{\partial \tilde{t}} + \frac{\partial}{\partial \tilde{x}} \int_0^{\tilde{h}_{\mathrm{film}}(\tilde{x})} \tilde{u}(\tilde{x},\tilde{y})\,\mathrm{d}\tilde{y} = 0 \; . \tag{3.35}$$

Double integration of the Momentum equation (3.31) under considerations of the boundary conditions yields

$$\tilde{u}(\tilde{x},\tilde{y}) = \frac{1}{\tilde{\mu}_{\mathrm{f}}}\tilde{\tau}_{\mathrm{g}}\tilde{y} \; . \tag{3.36}$$

Evaluation of (3.35) with the equation for $\tilde{u}$ (3.36) yields the wave equation for the film

$$\frac{\partial \tilde{h}_{\mathrm{film}}}{\partial \tilde{t}} + \frac{\partial}{\partial \tilde{x}}\left(\frac{\tilde{\tau}_{\mathrm{g}}}{\tilde{\mu}_{\mathrm{f}}}\frac{\tilde{h}_{\mathrm{film}}^2}{2}\right) =$$

$$\frac{\partial \tilde{h}_{\mathrm{film}}}{\partial \tilde{t}} + \frac{\tilde{\tau}_{\mathrm{g}}}{\tilde{\mu}_{\mathrm{f}}}\tilde{h}_{\mathrm{film}}\frac{\partial \tilde{h}_{\mathrm{film}}}{\partial \tilde{x}} + \frac{1}{\tilde{\mu}_{\mathrm{f}}}\frac{\tilde{h}_{\mathrm{film}}^2}{2}\frac{\partial \tilde{\tau}_{\mathrm{g}}}{\partial \tilde{x}} = 0 \; , \tag{3.37}$$

or in the dimensionless form

$$\frac{\partial h_{\mathrm{film}}}{\partial t} + \frac{1}{2}\frac{\tilde{\mu}_{\mathrm{g}}}{\tilde{\mu}_{\mathrm{f}}}\frac{\tilde{H}_{\mathrm{f}}}{\tilde{\delta}}\frac{\partial}{\partial x}\left(\tau_{\mathrm{g}}h_{\mathrm{film}}^2\right) =$$

$$\frac{\partial h_{\mathrm{film}}}{\partial t} + \frac{1}{2}\frac{\tilde{\mu}_{\mathrm{g}}}{\tilde{\mu}_{\mathrm{f}}}\frac{\tilde{H}_{\mathrm{f}}}{\tilde{\delta}}\left(\frac{\partial \tau_{\mathrm{g}}}{\partial x}h_{\mathrm{film}}^2 + 2\tau_{\mathrm{g}}h_{\mathrm{film}}\frac{\partial h_{\mathrm{film}}}{\partial x}\right) =$$

$$\frac{\partial h_{\mathrm{film}}}{\partial t} + \frac{\tilde{\mu}_{\mathrm{g}}}{\tilde{\mu}_{\mathrm{f}}}\frac{\tilde{H}_{\mathrm{f}}}{\tilde{\delta}}\tau_{\mathrm{g}}h_{\mathrm{film}}\frac{\partial h_{\mathrm{film}}}{\partial x} + \frac{1}{2}\frac{\tilde{\mu}_{\mathrm{g}}}{\tilde{\mu}_{\mathrm{f}}}\frac{\tilde{H}_{\mathrm{f}}}{\tilde{\delta}}\frac{\partial \tau_{\mathrm{g}}}{\partial x}h_{\mathrm{film}}^2 = 0 \; , \tag{3.38}$$

The assumption that the slip velocity $\tilde{u}_{\mathrm{s}}$ has the same order of magnitude as the piston velocity $\tilde{u}_{\mathrm{P}}$ for a small oil film height is false (3.24). Indeed, it was shown, that $\tilde{u}_{\mathrm{s}} \ll \tilde{u}_{\mathrm{P}}$ (3.25). The correct order of magnitude of the slip velocity will later be shown by the use of a CFD calculation of a compression cycle of a real compressor (see Sec. 6.1).

3.6.2 Oil film velocities due to gravity– and capillarity forces

The Navier–Stokes equations simplified by means of the usual assumptions of negligible lubricant inertia for thin films are used to calculate the gravity– and capillarity-driven film velocities in azimuthal direction (Fig. 3.11 describes the used nomencla-

Table 3.1: Parameters of oil film

$\tilde{\mu}_f$ [Pas]	$\tilde{\mu}_g$ [Pas]	$\tilde{\rho}_f$ [kg m^{-3}]	$\tilde{\rho}_g$ [kg m^{-3}]	$\tilde{H}_f$ [m]	$\tilde{\delta}$ [m]	$\tilde{\sigma}$ [N/m]
1×10^{-1}	1×10^{-5}	870	5	1×10^{-5}	1×10^{-3}	3×10^{-2}

$$\Rightarrow \frac{\tilde{\mu}_g}{\tilde{\mu}_f} \frac{\tilde{H}_f}{\tilde{\delta}} \sim 1 \times 10^{-6}$$
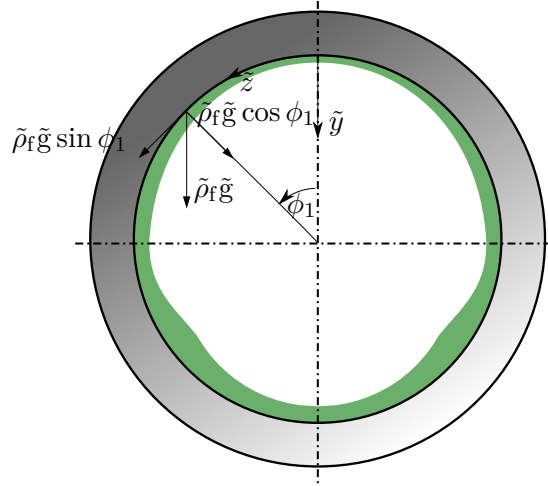
Figure 3.11: Geometry definitions used to estimate gravity-driven film velocity;

ture):

$$0 = \tilde{\rho}_f \tilde{g} \sin \phi_1 - \frac{\partial \tilde{p}}{\partial \tilde{z}} + \tilde{\mu}_f \frac{\partial^2 \tilde{w}}{\partial \tilde{y}^2} \tag{3.39a}$$

$$0 = \tilde{\rho}_f \tilde{g} \cos \phi_1 - \frac{\partial \tilde{p}}{\partial \tilde{y}} \tag{3.39b}$$

Boundary conditions are chosen to account for

- the pressure drop due to capillarity forces at the interface oil–air (3.40a),

- the continuity of tangential stress at the interface $\tilde{y} = \tilde{h}_{\text{film}}(\tilde{z}, \tilde{t})$, with $\tilde{\tau}_g \ll \tilde{\tau}_f$ (3.40b),

- the kinematic boundary condition (3.40c) and

- the no-slip condition (3.40d):

$$\tilde{y} = \tilde{h}_{\text{film}} : \qquad \qquad \tilde{p} = \tilde{p}_0 - \tilde{\sigma}\frac{\partial^2 \tilde{h}_{\text{film}}}{\partial \tilde{z}^2} \,, \qquad \qquad \text{(3.40a)}$$

$$\tilde{\mu}_{\text{f}}\frac{\partial \tilde{w}}{\partial \tilde{y}} = 0 \,, \qquad \qquad \text{(3.40b)}$$

$$\tilde{v} = \frac{\partial \tilde{h}_{\text{film}}}{\partial \tilde{t}} + \tilde{w}\frac{\partial \tilde{h}_{\text{film}}}{\partial \tilde{z}} \,, \qquad \qquad \text{(3.40c)}$$

$$\tilde{y} = 0 : \qquad \qquad \tilde{v} = 0 \,, \tilde{w} = 0 \,. \qquad \qquad \text{(3.40d)}$$

Double integration of the momentum equation (3.39a) with consideration of the boundary conditions and (3.39b) leads to the following equations for the film velocity $\tilde{w} = \tilde{w}(\tilde{y}, \tilde{z}, \tilde{t})$ and film height $\tilde{h}_{\text{film}}$:

$$\tilde{w} = \frac{1}{\tilde{\mu}_{\text{f}}}\left(\tilde{\rho}_{\text{f}}\tilde{g}\sin\phi_1\left(\frac{1}{\tilde{r}_{\text{cd}}}\tilde{h}_{\text{film}} - 1\right) - \tilde{\rho}_{\text{f}}\tilde{g}\cos\phi_1\frac{\partial \tilde{h}_{\text{film}}}{\partial \tilde{z}} - \tilde{\sigma}\frac{\partial^3 \tilde{h}_{\text{film}}}{\partial \tilde{z}^3}\right)$$
$$\cdot\left(\frac{\tilde{y}^2}{2} - \tilde{h}_{\text{film}}\tilde{y}\right) - \frac{1}{\tilde{\mu}_{\text{f}}}\tilde{\rho}_{\text{f}}\tilde{g}\sin\phi_1\frac{1}{\tilde{r}_{\text{cd}}}\left(\frac{\tilde{y}^3}{6} - \frac{\tilde{h}_{\text{film}}^2}{2}\tilde{y}\right) \,, \qquad \text{(3.41)}$$

$$\frac{\partial \tilde{h}_{\text{film}}}{\partial \tilde{t}} = -\frac{\partial}{\partial \tilde{z}}\int_0^{\tilde{h}_{\text{film}}}\tilde{w}\,\mathrm{d}\tilde{y} \,. \qquad \qquad \text{(3.42)}$$

Using the relations shown in (3.29), we get

$$\tilde{w}_s = \frac{\tilde{\rho}_{\text{f}}\tilde{g}\tilde{h}_{\text{film}}^2}{\tilde{\mu}_{\text{f}}}\frac{h^2}{2}\left(\sin\phi(1 - \frac{\tilde{h}_{\text{film}}}{\tilde{r}_{\text{cd}}}h) + \frac{\tilde{h}_{\text{film}}}{\tilde{r}_{\text{cd}}}\frac{\partial h}{\partial z}\cos\phi\right)$$
$$+ \frac{\tilde{h}_{\text{film}}^3\tilde{\sigma}}{\tilde{\mu}_{\text{f}}\tilde{r}_{\text{cd}}^3}\frac{h^2}{2}\frac{\partial^3 h}{\partial z^3} + \frac{\tilde{\rho}_{\text{f}}\tilde{g}}{\tilde{\mu}_{\text{f}}}\frac{\tilde{h}_{\text{film}}^3}{\tilde{r}_{\text{cd}}^3}\sin\phi\frac{h^3}{3} \,, \qquad \text{(3.43)}$$

where the term $\tilde{\sigma}\partial^3 h/\partial z$ describes the pressure gradient due to the surface tension at the interface oil–gas.

Taking typical quantities as shown in table 3.1 allows to neglect the second and third term in (3.43). The impact of capillarity forces is negligible compared to the gravity forces. We get

$$\tilde{w}_s = \frac{\tilde{\rho}_{\text{f}}\tilde{g}\tilde{h}_{\text{film}}^2}{\tilde{\mu}_{\text{f}}}\frac{h^2}{2}\left(\sin\phi + \frac{\tilde{h}_{\text{film}}}{\tilde{r}_{\text{cd}}}\frac{\partial h}{\partial z}\cos\phi\right) \,. \qquad \text{(3.44)}$$

This equation leads to estimated oil film velocities $\tilde{w}_s = \mathcal{O}(1 \times 10^{-5}\,\text{m/s})$. Figure 3.12 shows the oil film distribution after 60 s, starting from a uniform oil film height $\tilde{h}_{\text{film}} = 1 \times 10^{-5}\,\text{m}$. This result is derived by numerically solving (3.42), showing a change less than $10\,\%$ after 60 s.

Hence, not only capillarity driven oil velocities $w_{\text{cap}} \ll u_{\text{P}}$, but also gravity driven oil velocities in azimuthal direction $w_{\text{grav}} \ll u_{\text{P}}$.

Last but not least, the capillarity-driven pressure increase in the transition zones shall be estimated: The pressure increase across a convex interface between two fluids due to surface tension is

$$\Delta \tilde{p} = \tilde{\sigma}(\frac{1}{\tilde{R}_1} + \frac{1}{\tilde{R}_2}) \, , \tag{3.45}$$

with $\tilde{R}_1$ and $\tilde{R}_2$ being the principal radii of curvature. Evaluating this equation for typical quantities (see table 3.1) we get a pressure jump $\Delta \tilde{p} \approx 6$ mbar, which is small compared to typical hydrodynamic pressures necessary to hold the piston's weight.

These findings lead to the simplification of neglecting oil flow due to gravity– and capillarity forces in the global lubrication model.
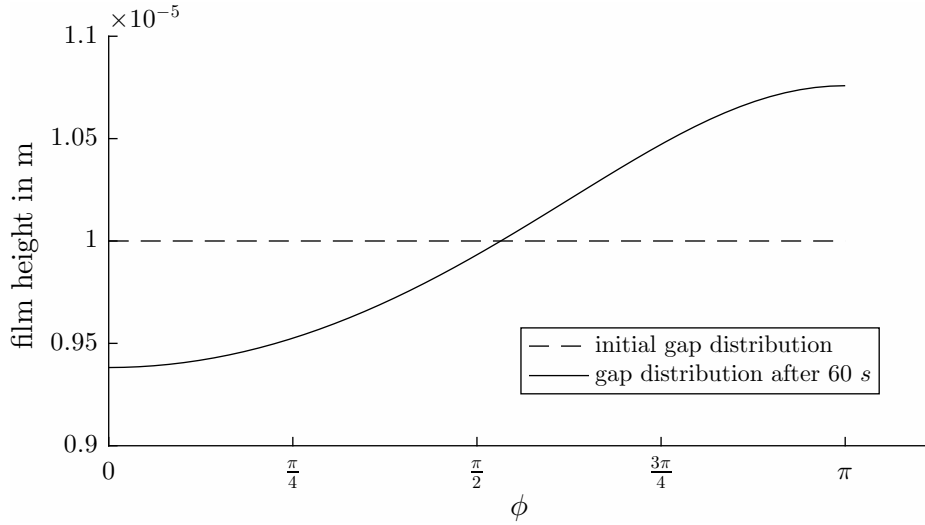
Figure 3.12: Gravity driven change of oil film distribution in azimuthal direction (initial state and state after 60 s).

Sec. 3.6.1 and Sec. 3.6.2 show that oil flow due to the gas flow in the compression chamber and due to gravity– and capillarity forces can be neglected in the global lubrication model. Therefore, the oil film distribution in the cylinder regions — which are the compression regions at head-end side and crank-end side, and the regions between any rings — is kept constant. At every time step, only the film heights of the boundary cells next to the rings need to be updated, leading to an oil trace which each ring is leaving.

3.7 Balance equation for calculation of gas pressure next to rings

To solve the Reynolds equation for the fully flooded ring regions, the pressure at both borders (transient regions) needs to be prescribed. Even though the rider
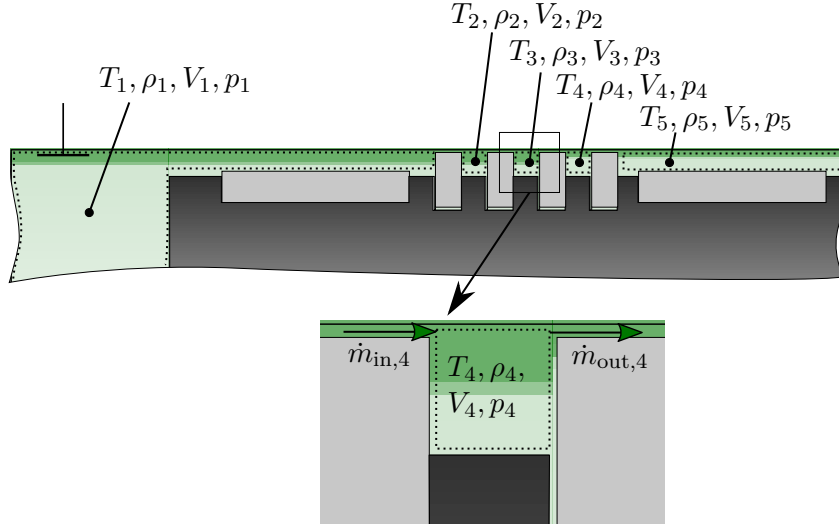
Figure 3.13: System boundaries to determine the course of pressure in the compression chamber and between rings. This is an exemplary case, in reality, the number of rings can vary.

rings are pressure balanced, the gas pressure defines the overall ring pressure level and influences at the end the happening of cavitation. The piston rings' motion is directly depending on the pressure level. Therefore it is necessary to calculate the time-dependent pressure levels in the compression chambers and between any rings.

The mixture of in-flowing gas with gas in each chamber is irreversible, therefore the energy balance has to be taken into account in addition to the mass balance. The cylinder wall is assumed to be adiabatic, the ideal gas law is used. Above all, the process is assumed to be quasi-static, resulting in a time-dependent, but uniform pressure distribution in each chamber.

The energy balance and the mass balance read

$$\frac{\mathrm{d}U}{\mathrm{d}t} = -p\frac{\mathrm{d}V}{\mathrm{d}t} + \dot{m}_{\mathrm{in}}\left(u_{\mathrm{in}}^m + p_{\mathrm{in}}^m v_{\mathrm{in}}^m\right) - \dot{m}_{\mathrm{out}}\left(u_{\mathrm{out}}^m + p_{\mathrm{out}}^m v_{\mathrm{out}}^m\right) \ , \tag{3.46}$$

$$\frac{\mathrm{d}m}{\mathrm{d}t} = \dot{m}_{\mathrm{in}} - \dot{m}_{\mathrm{out}} \ . \tag{3.47}$$

The assumption of a calorically perfect gas allows to apply the ideal gas law and to

assume constant heat capacities

$$pV = mRT$$
$$\Rightarrow \frac{\partial p}{\partial t}V + p\frac{\partial V}{\partial t} = RT\frac{\partial m}{\partial t} + mR\frac{\partial T}{\partial t} \ ,$$
$$\Rightarrow \frac{c_v}{R}\left[\frac{\partial p}{\partial t}V + p\frac{\partial V}{\partial t}\right] = c_v T\frac{\partial m}{\partial t} + mc_v\frac{\partial T}{\partial t} \ ,$$
$$c_p = \text{const}, c_v = \text{const}, c_p - c_v = R, \frac{c_p}{c_v} = \kappa \ . \tag{3.48}$$

Hence,

$$\frac{\mathrm{d}}{\mathrm{d}t}\left(mc_v T + mu_0\right) = u_0\frac{\mathrm{d}m}{\mathrm{d}t} + c_v T\frac{\partial m}{\partial t} + mc_v\frac{\partial T}{\partial t} =$$
$$- p\frac{\mathrm{d}V}{\mathrm{d}t} + \dot{m}_{\text{in}}\left(c_v T_{\text{in}}^m + u_0 + RT_{\text{in}}^m\right) - \dot{m}_{\text{out}}\left(c_v T + u_0 + RT\right) \tag{3.49}$$

and finally

$$\frac{\mathrm{d}p}{\mathrm{d}t} = \frac{\kappa}{V}\left(\dot{m}_{\text{in}}\frac{p_{\text{in}}^m}{\rho_{\text{in}}^m} - \dot{m}_{\text{out}}\frac{p}{\rho} - p\frac{\mathrm{d}V}{\mathrm{d}t}\right) \ , \tag{3.50a}$$

$$\frac{\mathrm{d}\rho}{\mathrm{d}t} = \frac{1}{V}\left(\dot{m}_{\text{in}} - \dot{m}_{\text{out}} - \rho\frac{\mathrm{d}V}{\mathrm{d}t}\right) \ . \tag{3.50b}$$

These are the final equations describing the progression of pressure in the compression chamber and between rings.

Finally, the mass flow across the rings and through the valves needs to be described. This is done, using the well-known Saint–Venant–Wantzel law. It describes the stationary, isentropic outflow of a calorically perfect gas of a pressure vessel and is derived using the stationary energy equation along a streamline. It reads

$$\dot{m} = A_1\sqrt{\frac{2\kappa}{\kappa - 1}p_0\rho_0}\sqrt{\left(\frac{p_1}{p_0}\right)^{\frac{2}{\kappa}} - \left(\frac{p_1}{p_0}\right)^{\frac{\kappa+1}{\kappa}}} \ . \tag{3.51}$$

Defining a compressibility ϵ_c

$$\epsilon_\text{c} = \sqrt{\frac{\kappa}{\kappa - 1}\frac{\left(\frac{\tilde{p}_1}{\tilde{p}_0}\right)^{\frac{2}{\kappa}} - \left(\frac{\tilde{p}_1}{\tilde{p}_0}\right)^{\frac{\kappa+1}{\kappa}}}{1 - \frac{\tilde{p}}{\tilde{p}_0}}} \ , \tag{3.52}$$

the Saint–Venant–Wantzel equation (3.51) can be reformulated, giving a relation between the mass flow and the differential pressure

$$\dot{m} = A_1\epsilon_\text{c}\sqrt{2\rho_0\left(p_0 - p_1\right)} \ . \tag{3.53}$$

The terms with index 0 are the stagnation terms in the vessel, index 1 stands for
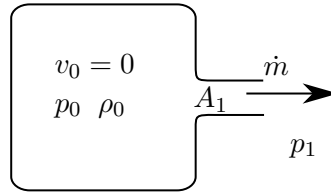
Figure 3.14: Description of terms used in Saint-Venant-Wantzel equation.

terms outside the vessel, see Fig. 3.14. The term A_1 is the opening cross-section and will be replaced by $\phi_{\text{valve}} = A_1\alpha$, $\alpha = \dot{m}/\dot{m}_{\text{th}} \leq 1$, which accounts for all kind of losses, but mainly due to flow separation. ϕ_{valve} is to be determined experimentally and should in most cases be known by the manufacturer of rings and valves.

For simplicity, the ϕ_{valve}-values of the rings are kept constant during calculation. In reality, the ϕ_{valve}-value of a ring increases on a long time range, dependent on the ring wear. The ϕ_{valve}-values of the valves are either zero or an average valve-dependent value: Any valve motion is not accounted for, the valves close and open instantaneously when a certain pressure level is reached.

3.8 Crosshead submodel
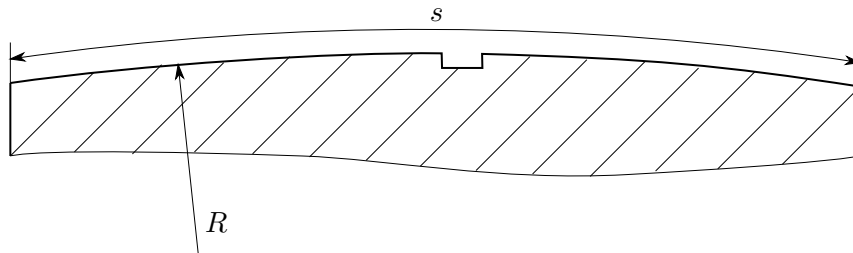
Figure 3.15: Drawing of upper crosshead sliding shoe, frontal view: s is the arc length, defining the width of the sliding shoe, R is its radius.

The crosshead is both hydrostatically and dynamically lubricated on the upper as well as the lower side. Therefore, we always have fully lubricated gaps. The 2D Reynolds equation is solved for both sides. A constant pump pressure is prescribed in the lubrication channels, the ambient pressure is described at the fixed boundaries. The crosshead is usually constructed very stiff, and is therefore assumed to be rigid. For that reason, the lubricated gaps are solely defined through the crosshead's motion.

The two cross-head sides are modelled as planes including machine-dependent lubrication channels. This assumption is valid as long as $s/R \ll 1$, where s is the arc length, defining the width of the sliding shoe and R is its radius, see Fig. 3.15.

4 System dynamics and kinematics (macroscale)

Even compressors, whose liners and crosshead slides are perfectly aligned, will have time dependent secondary piston motions (piston tilts and vertical movements of pistons) during operation. This is due to clearances which are existent in both crosshead– and piston guides. The secondary piston motion greatly affects the accumulated net-oil flow, which can only be estimated if the time– and system dependent lubricated gap distributions are known.

Therefore it is essential to include both the piston– and the crosshead movements in the dynamical model used to determine relevant gap geometries to calculate oil transport. In this section, the equation of motions shall be derived, which are describing the movement of the piston and crosshead.

4.1 Dynamic compressor model

The dynamic compressor model is a lumped-element model with ideal bearings, which are assumed to have zero clearance and do not transmit a moment. It is enhanced by a 1D Ritz ansatz. Hence, apart from the piston rod, all parts (the cranked shaft, connecting rod, crosshead and piston) are assumed to be rigid. To describe the tilt of the piston, vertical displacements of the crosshead $y_C(t)$ as well of the piston $y_P(t)$ are accounted for.

The model has three generalized DOFs (see Fig. 4.1): (1) The vertical displacement of the crosshead $y_C(t)$, (2) the tilt of the piston rod $\alpha(t)$ and (3) $q(t)$, an approximation for the max. vertical displacement of the piston rod due to bending. The bending line is determined using the ansatz

$$w(\xi, t) = q(t) \cdot \phi(\xi) \,, \tag{4.1a}$$

$$\phi(\xi) = \xi^2 / l_b^2 \,, \tag{4.1b}$$

$\phi(\xi)$ being a quadratic ansatz function and l_b being the bending length of the piston rod (see Fig. 4.2) . This ansatz is chosen, because it shows good agreement with analytical results (see Sec. 4.1.1).

$F_{P,x}, F_{P,y}$ and M_P are the generalized, impressed forces and moment acting on the piston due to gas forces and due to the oil film pressure between the rider ring and the cylinder wall. $F_{C,x}, F_{C,y}$ and M_C are the corresponding impressed forces and moment acting on the crosshead. The angle γ accounts for the possibility of different mounting positions of the compressor (every position from horizontal to vertical is

possible). It is necessary not to confuse these generalized forces with physical forces: Their relations are specified in Sec. 4.2.1 and in Sec. 4.2.2.

The position, velocity and acceleration of the crosshead $x_C(\Theta), \dot{x}_C(\Theta), \ddot{x}_C(\Theta)$ are implied by the crank motion and can be approximated by the following equations [38]:

$$x_C(\Theta) = r_{\mathrm{cd}} \left[(1 - \cos \Theta) + \frac{\lambda_s}{4} (1 - \cos (2\Theta)) \right] + \mathcal{O}(\lambda_s^4) \, , \qquad (4.2\mathrm{a})$$

$$\dot{x}_C(\Theta) = \omega r_{\mathrm{cd}} \left[\sin \Theta + \frac{1}{2} \lambda_s \sin (2\Theta) \right] + \mathcal{O}(\lambda_s^4) \, , \qquad (4.2\mathrm{b})$$

$$\ddot{x}_C(\Theta) = \omega^2 r_{\mathrm{cd}} \left[\cos \Theta + \lambda_s \cos (2\Theta) \right] + \mathcal{O}(\lambda_s^4) \, . \qquad (4.2\mathrm{c})$$

Here, λ_s is the relation of crank radius to connecting rod length, r_{cd} is the crank radius and ω is the the angular velocity of the cranked drive. These terms were derived by an expansion in power series and neglecting higher terms, which is justified for usual values of $\lambda_s \approx 0.2$–0.35. Summarized, the following main assumptions are made:

- mainly, the model is a lumped mass model, consisting of the rigid bodies: (1) piston, (2) crosshead, (3) connecting rod and (4) cranked shaft; the bending of the piston rod is accounted for by the ansatz $w(\xi, t) = q(t) \cdot \phi(\xi)$

- the bearings of connecting rod and cranked shaft are assumed to be ideal (frictionless and zero clearance)

- the angular velocity ω of the crank is constant

- the model is symmetric in z-direction

- tilt $\alpha \ll 1$ and max. bending $q \ll l_{\mathrm{b}}$.

The equations of motion are derived using the Lagrange's equation of motion for the i-th DOF:

$$\frac{\mathrm{d}}{\mathrm{d}t} \frac{\partial T_{\mathrm{kin,tot}}}{\partial \dot{q}_i} - \frac{\partial T_{\mathrm{kin,tot}}}{\partial q_i} - Q_i + \frac{\partial V_{\mathrm{tot}}}{\partial q_i} = 0 \, ; \qquad (4.3)$$
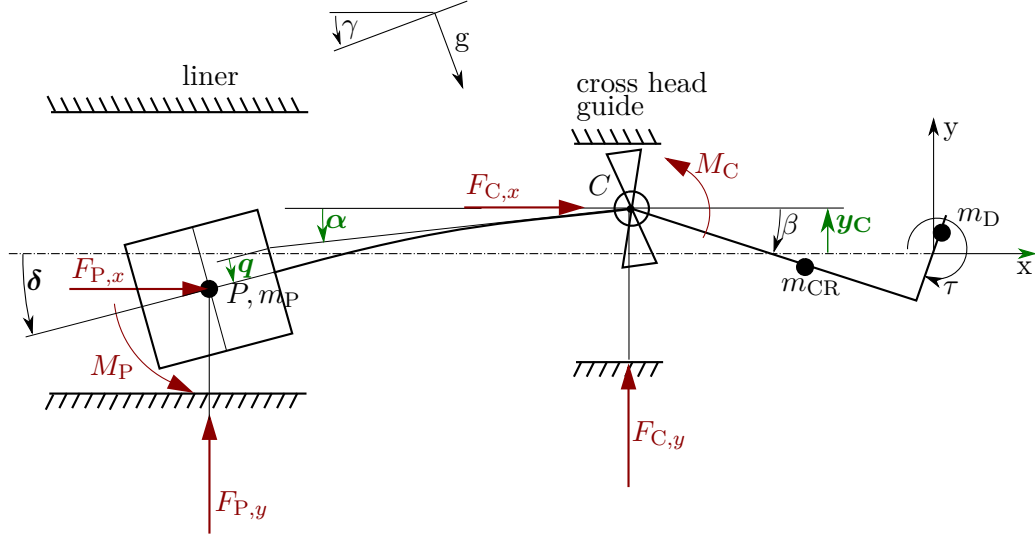
Figure 4.1: Mechanical model: degrees of freedom are shown in green, generalized forces are shown in red.

With

$$x_{\mathrm{P}} = x_{\mathrm{C}} - l_{\mathrm{P}} \cos \alpha + \left(w(\xi)\big|_{\xi=l_{\mathrm{b}}} + \frac{b_{\mathrm{P}}}{2} \frac{\partial w(\xi)}{\partial \xi}\bigg|_{\xi=l_{\mathrm{b}}} \right) \sin \alpha \qquad (4.4\mathrm{a})$$

$$y_{\mathrm{P}} = y_{\mathrm{C}} - l_{\mathrm{P}} \sin \alpha - \left(w(\xi)\big|_{\xi=l_{\mathrm{b}}} + \frac{b_{\mathrm{P}}}{2} \frac{\partial w(\xi)}{\partial \xi}\bigg|_{\xi=l_{\mathrm{b}}} \right) \cos \alpha \qquad (4.4\mathrm{b})$$

$$x_{\mathrm{PR}}(\xi) = x_{\mathrm{C}} - \xi \cos \alpha + w(\xi) \sin \alpha \qquad (4.4\mathrm{c})$$
$$y_{\mathrm{PR}}(\xi) = y_{\mathrm{C}} - \xi \sin \alpha - w(\xi) \cos \alpha \qquad (4.4\mathrm{d})$$
$$x_{\mathrm{CH}} = x_{\mathrm{C}} - l_{\mathrm{CH2}} \cos \alpha \qquad (4.4\mathrm{e})$$
$$y_{\mathrm{CH}} = y_{\mathrm{C}} - l_{\mathrm{CH2}} \sin \alpha \qquad (4.4\mathrm{f})$$
$$x_{\mathrm{CR}} = x_{\mathrm{C}} + l_{\mathrm{R1}} \cos \beta \qquad (4.4\mathrm{g})$$
$$y_{\mathrm{CR}} = y_{\mathrm{C}} - l_{\mathrm{R1}} \sin \beta \qquad (4.4\mathrm{h})$$
$$l_{\mathrm{P}} = l_{\mathrm{b}} + \frac{b_{\mathrm{P}}}{2} \; , \qquad (4.4\mathrm{i})$$

$(x_{\mathrm{P}}, y_{\mathrm{P}}), (x_{\mathrm{CH}}, y_{\mathrm{CH}}), (x_{\mathrm{CR}}, y_{\mathrm{CR}})$ being the positions of centre of mass of piston, crosshead (including crosshead nut) and connecting rod and $(x_{PR}(\xi), y_{PR}(\xi))$ describing the
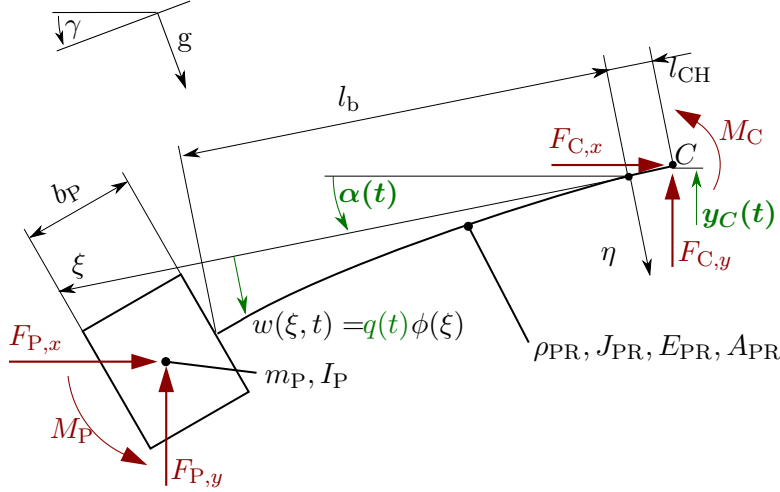
Figure 4.2: Drawing to show displacement of piston due to bending

piston rod's mid-line. The corresponding velocities are

$$v_{\mathrm{P}} = (\dot{x}_{\mathrm{P}}^2 + \dot{y}_{\mathrm{P}}^2)^{1/2} \, , \tag{4.5a}$$

$$v_{\mathrm{PR}}(\xi) = (\dot{x}_{\mathrm{PR}}^2(\xi) + \dot{y}_{\mathrm{PR}}^2(\xi))^{1/2} \, , \tag{4.5b}$$

$$v_{\mathrm{CH}} = (\dot{x}_{\mathrm{CH}}^2 + \dot{y}_{\mathrm{CH}}^2)^{1/2} \, , \tag{4.5c}$$

$$v_{\mathrm{CR}} = (\dot{x}_{\mathrm{CR}}^2 + \dot{y}_{\mathrm{CR}}^2)^{1/2} \, . \tag{4.5d}$$

We obtain the following statements for the kinetic energies of piston, connecting rod, piston rod and crosshead (including nut)

$$T_{\mathrm{kin,P}} = \frac{1}{2} m_{\mathrm{P}} v_P^2 + \frac{1}{2} I_{\mathrm{P}} \left(\dot{\alpha}(t) + \frac{\partial^2 w}{\partial \xi \partial t} \bigg|_{\xi=l_{\mathrm{b}}} \right)^2 \, , \tag{4.6a}$$

$$T_{\mathrm{kin,PR}} = \int_0^{l_{\mathrm{b}}} \frac{1}{2} \rho_{\mathrm{PR}} A_{\mathrm{PR}} v_{PR}^2(\xi) \, \mathrm{d}\xi$$

$$+ \int_0^{l_{\mathrm{b}}} \frac{1}{2} \left(\dot{\alpha} + \frac{\partial^2 w}{\partial t \partial \xi} \right)^2 \left(\rho_{\mathrm{PR}} A_{\mathrm{PR}} \frac{r_{\mathrm{PR}}^2}{4} \right) \mathrm{d}\xi \, , \tag{4.6b}$$

$$T_{\mathrm{kin,CH}} = \frac{1}{2} m_{\mathrm{CH}} v_{CH}^2 + \frac{1}{2} I_{\mathrm{CH}} \dot{\alpha}^2(t) \, , \tag{4.6c}$$

$$T_{\mathrm{kin,CR}} = \frac{1}{2} m_{\mathrm{CR}} v_{CR}^2 + \frac{1}{2} I_{\mathrm{CR}} \dot{\beta}^2(t) \, , \tag{4.6d}$$

resulting into the total kinetic energy

$$T_{\mathrm{kin,tot}} = T_{\mathrm{kin,P}} + T_{\mathrm{kin,PR}} + T_{\mathrm{kin,CH}} + T_{\mathrm{kin,CR}} \, . \tag{4.7}$$

The strain energy U and the potentials V_i of the system are

$$U = \frac{1}{2} \int_0^{l_b} E_{\mathrm{PR}} J_{\mathrm{PR}} \left(\frac{\partial^2 w(\xi)}{\partial \xi^2} \right)^2 \mathrm{d}\xi \;, \tag{4.8a}$$

$$V_{\mathrm{P}} = m_{\mathrm{P}} g y_P \cos\gamma - m_{\mathrm{P}} g x_P \sin\gamma \;, \tag{4.8b}$$

$$V_{\mathrm{PR}} = \int_0^{l_b} \Big[\rho_{\mathrm{PR}} g A_{\mathrm{PR}} \big[- w(\xi) \cos(\gamma - \alpha(t))$$

$$- (\xi + l_{\mathrm{CH}}) \sin\alpha \cos\gamma + y_C \cos\gamma \big] \Big] \mathrm{d}\xi \;, \tag{4.8c}$$

$$V_{\mathrm{CH}} = m_{\mathrm{CH}} g y_{\mathrm{CH}} \cos\gamma - m_{\mathrm{CH}} g x_{\mathrm{CH}} \sin\gamma \;, \tag{4.8d}$$

$$V_{\mathrm{CR}} = m_{\mathrm{CR}} g y_{\mathrm{CR}} \cos\gamma - m_{\mathrm{CR}} g x_{\mathrm{CR}} \sin\gamma \;, \tag{4.8e}$$

resulting into the total potential

$$V_{\mathrm{tot}} = U + V_{\mathrm{P}} + V_{\mathrm{PR}} + V_{\mathrm{CH}} + V_{\mathrm{CR}} \;. \tag{4.9}$$

For the generalized forces Q_i and the resulting virtual works δA_i apply

$$\delta A = \delta A_\alpha + \delta A_{y_C} + \delta A_q = Q_\alpha \delta\alpha + Q_{y_C} \delta y_C + Q_q \delta q \;, \tag{4.10a}$$

$$Q_\alpha = M_P + M_C + F_{P,x} \left[l_P \sin\alpha + q \cos\alpha \left(1 + \frac{b_{\mathrm{P}}}{l_b} \right) \right]$$

$$+ F_{\mathrm{gas}} \cos\left(\frac{2q}{l_b} + \alpha \right) \left(l_P \sin\alpha + q \cos\alpha \left(1 + \frac{b_{\mathrm{P}}}{l_b} \right) \right)$$

$$+ F_{\mathrm{gas}} \sin\left(\frac{2q}{l_b} + \alpha \right) \left(-l_P \cos\alpha + q \sin\alpha \left(1 + \frac{b_{\mathrm{P}}}{l_b} \right) \right)$$

$$+ F_{P,y} \left[-l_P \cos\alpha + q \sin\alpha \left(1 + \frac{b_{\mathrm{P}}}{l_b} \right) \right] \;, \tag{4.10b}$$

$$Q_{y_C} = F_{P,y} + F_{C,y} + F_{\mathrm{gas}} \sin\alpha \left(\frac{2q}{b} + \alpha \right) \;, \tag{4.10c}$$

$$Q_q = F_{P,x} \sin\alpha \left(1 + \frac{b_{\mathrm{P}}}{l_b} \right) - F_{P,y} \cos\alpha \left(1 + \frac{b_{\mathrm{P}}}{l_b} \right) + 2 M_P \frac{1}{l_b}$$

$$+ F_{\mathrm{gas}} \left(1 + \frac{b_{\mathrm{P}}}{l_b} \right) \left(\sin\alpha \cos\left(\frac{2q}{l_b} + \alpha \right) - \cos\alpha \sin\left(\frac{2q}{l_b} + \alpha \right) \right) \;. \tag{4.10d}$$

Inserting above statements into the Lagrange's equations of motion 4.3 yields, after some tedious rearrangements, three equations, governing the three DOFs α, y_C and

q. Linearised for $\alpha \ll 1$ and $q \ll l_{\mathrm{b}}$, they finally read

$$
\begin{aligned}
q\Bigg(&- (F_{\mathrm{P},x} + \alpha F_{\mathrm{P},y})\left(1 + \frac{b_{\mathrm{P}}}{l_{\mathrm{b}}}\right) - F_{\mathrm{gas}}\left[\cos\frac{2q}{l_{\mathrm{b}}}\left(1 + \frac{b_{\mathrm{P}}}{l_{\mathrm{b}}}\right)\right] \\
&+ \frac{1}{3}\alpha\rho_{\mathrm{PR}}A_{\mathrm{PR}}\mathrm{g}\left(\cos\gamma - \sin\gamma\right)l_{\mathrm{b}} \\
&+ (\alpha\mathrm{g}m_{\mathrm{P}}\cos\gamma - \mathrm{g}m_{\mathrm{P}}\sin\gamma)\left(1 + \frac{b_{\mathrm{P}}}{l_{\mathrm{b}}}\right)\Bigg) \\
&+ q(\ddot{y}_C\alpha + \ddot{x}_C)\left(\frac{1}{3}\rho_{\mathrm{PR}}A_{\mathrm{PR}}l_{\mathrm{b}} + m_{\mathrm{P}}\left(1 + \frac{b_{\mathrm{P}}}{l_{\mathrm{b}}}\right)\right) \\
&+ \left(q^2\ddot{\alpha} + 2q\dot{\alpha}\dot{q}\right)\left(\frac{1}{5}\rho_{\mathrm{PR}}A_{\mathrm{PR}}l_{\mathrm{b}} + m_{\mathrm{P}}\left(1 + \frac{b_{\mathrm{P}}^2}{l_{\mathrm{b}}^2} + 2\frac{b_{\mathrm{P}}}{l_{\mathrm{b}}}\right)\right) \\
&+ \ddot{q}\Bigg(\frac{1}{4}r_{\mathrm{PR}}^2\rho_{\mathrm{PR}}A_{\mathrm{PR}} + \frac{1}{4}\rho_{\mathrm{PR}}A_{\mathrm{PR}}l_{\mathrm{b}}^2 + \frac{1}{3}l_{\mathrm{b}}\rho_{\mathrm{PR}}A_{\mathrm{PR}}l_{\mathrm{CH}} \\
&\qquad + l_{\mathrm{P}}m_{\mathrm{P}}\left(1 + \frac{b_{\mathrm{P}}}{l_{\mathrm{b}}}\right) + 2I_P\frac{1}{l_{\mathrm{b}}}\Bigg) \\
&+ \ddot{\alpha}\Bigg(I_{\mathrm{CH}} + I_{\mathrm{P}} + \rho_{\mathrm{PR}}A_{\mathrm{PR}}\left[\frac{1}{4}r_{\mathrm{PR}}^2l_{\mathrm{b}} + \frac{1}{3}l_{\mathrm{b}}^3\right] \\
&\qquad + l_{\mathrm{CH2}}^2m_{\mathrm{CH}} + l_{\mathrm{P}}^2m_{\mathrm{P}} + l_{\mathrm{b}}^2\rho_{\mathrm{PR}}A_{\mathrm{PR}}l_{\mathrm{CH}} + l_{\mathrm{b}}\rho_{\mathrm{PR}}A_{\mathrm{PR}}l_{\mathrm{CH}}^2\Bigg) \\
&+ (\alpha\ddot{x}_C - \ddot{y}_C)\left(\frac{1}{2}\rho_{\mathrm{PR}}A_{\mathrm{PR}}l_{\mathrm{b}}^2 + l_{\mathrm{CH2}}m_{\mathrm{CH}} + l_{\mathrm{P}}m_{\mathrm{P}} + l_{\mathrm{b}}\rho_{\mathrm{PR}}A_{\mathrm{PR}}l_{\mathrm{CH}}\right) \\
&+ F_{\mathrm{P},y}l_{\mathrm{P}} - \alpha F_{\mathrm{P},x}l_{\mathrm{P}} - M_{\mathrm{P}} - M_{\mathrm{C}} + F_{\mathrm{gas}}l_{\mathrm{P}}\sin\frac{2q}{l_{\mathrm{b}}} \\
&- \mathrm{g}l_{\mathrm{P}}m_{\mathrm{P}}\left(\alpha\sin\gamma + \cos\gamma\right) - \rho_{\mathrm{PR}}A_{\mathrm{PR}}\mathrm{g}\cos\gamma\left(l_{\mathrm{b}}l_{\mathrm{CH}} + \frac{1}{2}l_{\mathrm{b}}^2\right) = 0\,,
\end{aligned}
$$

(4.11)

$$
\begin{aligned}
&\mathrm{g}\cos\gamma\,(m_{\mathrm{CR}}+m_{\mathrm{P}}) \\
&+ \ddot{y}_C\left(\rho_{\mathrm{PR}}A_{\mathrm{PR}}l_{\mathrm{b}}+m_{\mathrm{CH}}+m_{\mathrm{P}}+m_{\mathrm{CR}}\right) \\
&+ m_{\mathrm{CR}}l_{\mathrm{CR1}}\left(\dot{\beta}^2\sin\beta-\ddot{\beta}\cos\beta\right) \\
&+ q\left(\frac{1}{3}r_{\mathrm{PR}}^2\rho_{\mathrm{PR}}A_{\mathrm{PR}}l_{\mathrm{b}}+r_{\mathrm{PR}}^2 m_{\mathrm{P}}\left(1+\frac{b_{\mathrm{P}}}{l_{\mathrm{b}}}\right)\right) \\
&+ \left(\alpha\ddot{\alpha}q-\ddot{q}+2\alpha\dot{\alpha}\dot{q}\right)\left(\frac{1}{3}\rho_{\mathrm{PR}}A_{\mathrm{PR}}l_{\mathrm{b}}+m_{\mathrm{P}}\left(1+\frac{b_{\mathrm{P}}}{l_{\mathrm{b}}}\right)\right) \\
&+ \left(\alpha\dot{\alpha}^2-\ddot{\alpha}\right)\left(\frac{1}{2}\rho_{\mathrm{PR}}A_{\mathrm{PR}}l_{\mathrm{b}}^2+l_{\mathrm{CH2}}m_{\mathrm{CH}}+l_{\mathrm{P}}m_{\mathrm{P}}+l_{\mathrm{b}}\rho_{\mathrm{PR}}A_{\mathrm{PR}}l_{\mathrm{CH}}\right) \\
&- F_{\mathrm{P},y}-F_{\mathrm{C},y}-F_{\mathrm{gas}}\left(\sin\frac{2q}{l_{\mathrm{b}}}+\alpha\cos\frac{2q}{l_{\mathrm{b}}}\right)=0\,,
\end{aligned}
\tag{4.12}
$$

and

$$
\begin{aligned}
&q\left(4E_{\mathrm{PR}}J_{\mathrm{PR}}\frac{1}{l_{\mathrm{b}}^3}-\frac{1}{5}\dot{\alpha}^2\rho_{\mathrm{PR}}A_{\mathrm{PR}}l_{\mathrm{b}}\right. \\
&\qquad\left.-\dot{\alpha}^2 m_{\mathrm{P}}\left(1+\frac{b_{\mathrm{P}}^2}{l_{\mathrm{b}}^2}+\frac{2b_{\mathrm{P}}}{l_{\mathrm{b}}}\right)+2F_{\mathrm{gas}}\left(\frac{1}{l_{\mathrm{b}}}+\frac{b_{\mathrm{P}}}{l_{\mathrm{b}}^2}\right)\right) \\
&+ \ddot{q}\left(\frac{1}{3}r_{\mathrm{PR}}^2\rho_{\mathrm{PR}}A_{\mathrm{PR}}\frac{1}{l_{\mathrm{b}}}+\frac{1}{5}\rho_{\mathrm{PR}}A_{\mathrm{PR}}l_{\mathrm{b}}\right. \\
&\qquad\left.+\ 4I_{\mathrm{P}}\frac{1}{l_{\mathrm{b}}^2}+m_{\mathrm{P}}\left(1+\frac{b_{\mathrm{P}}^2}{l_{\mathrm{b}}^2}+\frac{2b_{\mathrm{P}}}{l_{\mathrm{b}}}\right)\right) \\
&+ \ddot{\alpha}\left(\frac{1}{4}r_{\mathrm{PR}}^2\rho_{\mathrm{PR}}A_{\mathrm{PR}}+\frac{1}{4}\rho_{\mathrm{PR}}A_{\mathrm{PR}}l_{\mathrm{b}}^2+2I_{\mathrm{P}}\frac{1}{l_{\mathrm{b}}}\right. \\
&\qquad\left.+b_{\mathrm{P}}l_{\mathrm{P}}m_{\mathrm{P}}\frac{1}{l_{\mathrm{b}}}+l_{\mathrm{P}}m_{\mathrm{P}}+\frac{1}{3}\rho_{\mathrm{PR}}A_{\mathrm{PR}}l_{\mathrm{CH}}l_{\mathrm{b}}\right) \\
&+ \left(\alpha\ddot{x}_C-\ddot{y}_C\right)\left(\frac{1}{3}\rho_{\mathrm{PR}}A_{\mathrm{PR}}l_{\mathrm{b}}+m_{\mathrm{P}}\left(1+\frac{b_{\mathrm{P}}}{l_{\mathrm{b}}}\right)\right) \\
&- \mathrm{g}\left(\alpha\sin\gamma+\cos\gamma\right)\left(b_{\mathrm{P}}m_{\mathrm{P}}\frac{1}{l_{\mathrm{b}}}+m_{\mathrm{P}}+\frac{1}{3}\rho_{\mathrm{PR}}A_{\mathrm{PR}}l_{\mathrm{b}}\right) \\
&- 2M_{\mathrm{P}}\frac{1}{l_{\mathrm{b}}}+\left(1+\frac{b_{\mathrm{P}}}{l_{\mathrm{b}}}\right)\left(F_{\mathrm{P},y}-\alpha F_{\mathrm{P},x}\right)=0\,.
\end{aligned}
\tag{4.13}
$$

Equations (4.11) and (4.12) can be interpreted as a result of the principal of angular and linear momentum, respectively. The third equation (4.13) describes the bending of the piston rod.

4.1.1 Consistency of equations of motion

Some sanity checks are done to verify the correctness of the derived equations of motions: The accuracy of the 1-DOF Ritz ansatz (4.1) shall be checked and the overall correctness of the system of equations (4.11–4.13) shall be controlled by comparing special cases of the derived equations of motion with analytical solutions taken from literature:

1. The equation of motion describing the piston rod bending (4.13) is compared with the analytical equation describing the eigenfrequency of an unloaded beam, clamped at one end. Also, this equation of motion is compared to the analytical solution describing the bending of a beam either loaded by a concentrated force or by an evenly distributed force (see e.g. [11]).

2. Equation (4.11) with $\gamma = -\pi/2, q = 0, y_C = 0$ should become the well known differential equation describing the physical pendulum.

First, the accuracy of the Ritz ansatz shall be assessed. For this purpose, (4.13) is evaluated.

Eigenfrequency of the piston rod, clamped at one side

To get the eigenfrequencies of the unloaded piston rod we set $\alpha = \dot{\alpha} = \ddot{\alpha} = 0$, $y_C = \dot{y}_C = \ddot{y}_C = 0$, $x_C = \dot{x}_C = \ddot{y}_C = 0$ and g $= 0$, resulting in the following equation

$$q \left[4E_{PR} J_{PR} \frac{1}{l_b^3} \right] + \ddot{q} \left[\frac{1}{3} r_{PR}^2 \rho_{PR} A_{PR} \frac{1}{l_b} + \frac{1}{5} \rho_{PR} A_{PR} l_b + \right.$$
$$\left. 4I_P \frac{1}{l_b^2} + m_P \left(1 + \frac{b_P^2}{l_b^2} + \frac{2b_P}{l_b} \right) \right] = 0 . \tag{4.14}$$

Written in the form

$$\ddot{q} + \omega_{PR}^2 q = 0 ,$$

with ω_{PR} being the eigenfrequencies of the system piston/piston rod, we get the following expression for ω_{PR}^2

$$\omega_{PR}^2 = \frac{4E_{PR}J_{PR}}{l_b^3 \left[\frac{1}{3} r_{PR}^2 \rho_{PR} A_{PR} \frac{1}{l_b} + \frac{1}{5} \rho_{PR} A_{PR} l_b + 4I_P \frac{1}{l_b^2} + m_P \left(1 + \frac{b_P^2}{l_b^2} + \frac{2b_P}{l_b} \right) \right]} \tag{4.15}$$

In Parkus [43, p. 199]), for instance, one can find the fundamental frequency of unloaded beams, clamped at one side:

$$\omega_{lit} = \frac{3.52}{l_b^2} \sqrt{\frac{E_{PR} J_{PR}}{\rho_{PR} A_{PR}}} . \tag{4.16}$$

In the derivation of this equation, the effects of rotatory inertia are neglected. Doing the same in (4.15) and setting the weight of the piston $m_P = 0$, we get

$$\omega_{PR} = \frac{4.47}{l_b^2} \sqrt{\frac{E_{PR} J_{PR}}{\rho_{PR} A_{PR}}}, \tag{4.17}$$

Bending of the piston rod

Equation (4.13) with all time derivations and F_{gas} set to zero is used to compare the bending stiffness to analytical solutions for bending lines of beams (see e.g. table 5–7 in [11, Ch. E]).

With the assumptions of horizontal installation position ($\gamma = 0$) and concentrated load at position $\xi = l_b$ ($M_P = 0, F_{P,x} = 0, \rho_{PR} = 0$), we get

$$w(l_b) = \frac{l_b^3}{4E_{PR} J_{PR}} (gm_P - F_{P,y}), \tag{4.18}$$

which represents a higher stiffness than that predicted by the classical solution found in literature:

$$w_{lit} = \frac{l_b^3}{3E_{PR} J_{PR}} (gm_P - F_{P,y}). \tag{4.19}$$

Similar conclusions are found considering the piston rod's weight, but neglecting all forces: Again, the derived bending

$$w(l_b) = \frac{\rho_{PR} A_{PR} l_b^4 g}{12 E_{PR} J_{PR}} \tag{4.20}$$

is lower than the analytical solution

$$w_{lit} = \frac{\rho A_{PR} l_b^3 g}{8 E_{PR} J_{PR}}. \tag{4.21}$$

Both the calculation of bending line and the calculation of eigenfrequencies show an increased stiffness of the piston rod. The bending due to a concentrated load and a distributed load is underestimated by 25 % and 34 %, respectively, the fundamental frequency is overestimated by 27 %. This was expected due to the reduction of degrees of freedom (1 DOF-Ritz ansatz). Different forms of the Ritz ansatz were tried to improve the accuracy of the resulting equation of motion. However, no better 1-term ansatz was found which satisfies both load cases (distributed load and concentrated load) better. A multi-term ansatz of the form

$$w(\xi, t) = q(t) \cdot \left(a \frac{\xi^2}{l_b^2} + b \frac{\xi^3}{l_b^3} + c \frac{\xi^4}{l_b^4} \right), \tag{4.22}$$

would significantly improve the solution, but was not implemented for simplicity.

Correctness of equation of motion

Equation (4.11) with $\gamma = -\pi/2, q = 0, y_C = 0$ should become the well known differential equation describing the physical pendulum. With

$$I_{\text{PR,C}} = \frac{\rho_{\text{PR}}A_{\text{PR}}l_b}{4}\left[r_{\text{PR}}^2 + \frac{4l_b^2}{3}\right] + (\rho_{\text{PR}}A_{\text{PR}}l_b)\left(\frac{l_b}{2} + l_{\text{CH}}\right)^2 , \tag{4.23a}$$

$$I_{\text{CH,C}} = I_{\text{CH}} + l_{\text{CH2}}^2 m_{\text{CH}} , \tag{4.23b}$$

$$I_{\text{P,C}} = I_{\text{P}} + l_{\text{P}}^2 m_{\text{P}} , \tag{4.23c}$$

$$I_{\text{tot,C}} = I_{\text{PR,C}} + I_{\text{CH,C}} + I_{\text{P,C}} , \tag{4.23d}$$

being the mass moments of inertia regarding point C and the assumptions mentioned before, (4.11) leads as expected to the solution of a physical pendulum for $\alpha \ll 1$

$$\ddot{\alpha}I_{\text{tot,C}} = -\text{g}l_{\text{P}}m_{\text{P}}\alpha . \tag{4.24}$$

4.2 Submodels

To close the system of equations of motions, it takes two additional submodels that describe the impressed forces and moments acting on piston and crosshead: The rider ring model describes the relation between piston movement and the impressed forces $F_{\text{P},x}, F_{\text{P},y}, M_{\text{P}}$. Accordingly, the crosshead model links the position of the crosshead with the impressed forces $F_{\text{C},x}, F_{\text{C},y}, M_{\text{C}}$. This is done by solving the well known Reynolds equation over the gap between the lubricated surfaces (rings and liners, crosshead and crosshead guides).

The main functions and constructions of piston- and rider rings are explained in Sec. 1.2.2. The rider ring submodel calculates the impressed piston forces depending on the pistons position, velocity and tilt. In contrast, the piston ring submodel is not needed directly for the system dynamics. However, it is important to take the piston ring's motion into account for oil flow calculations that exert influence on oil film thickness of reservoirs between and next to rings. This way, piston rings eventually infect the pressure distribution along the rider rings.

4.2.1 Rider ring model

Rider rings seat solidly on the piston's nuts and transmit oil– and contact forces to the piston. The ring shall be assumed to move with the piston. Then, the piston's position and inclination as well as the ring's deformation solely define the gap between cylinder wall and rider ring. The resulting point of application of the total force acting on the piston does not need to be the piston's axial position of centre of gravity. This is due to uneven pressure distributions or simple due to a shifted rider ring. Figure 4.4 shows the position of the resultant force $F_{\text{P,y,sub}}$ relative to the centre of gravity of the piston. The resultant force is the sum of all vertical force components acting on the piston, caused by all rider rings.

The generalized forces and moment of the rider ring sub-model are

$$F_{\mathrm{P},y} = \cos\left(\frac{2q}{b_{\mathrm{P}}} + \alpha\right) \sum_i F_{\mathrm{P,y,sub,i}} + \sin\left(\frac{2q}{b_{\mathrm{P}}} + \alpha\right) \sum_i F_{\mathrm{P,x,sub,i}} , \qquad (4.25a)$$

$$F_{\mathrm{P},x} = \sin\left(\frac{2q}{b_{\mathrm{P}}} + \alpha\right) \sum_i F_{\mathrm{P,y,sub,i}} + \cos\left(\frac{2q}{b_{\mathrm{P}}} + \alpha\right) \sum_i F_{\mathrm{P,x,sub,i}} , \qquad (4.25b)$$

$$M_{\mathrm{P}} = \sum_i F_{\mathrm{P,y,sub,i}} l_{\mathrm{rr},y,i} + \frac{d_{\mathrm{P}}}{2} \sum_i F_{\mathrm{P,x,sub,i}} . \qquad (4.25c)$$

4.2.2 Crosshead model

The crosshead is rigidly mounted to the piston rod. It is guided by the upper and lower crosshead slides and is both hydrostatically and dynamically lubricated. Figure 4.3 shows the position of the relevant forces. The resulting generalized force and moment are

Figure 4.3: Generalized force and moment of global model (shown in red) as well as local force and moment and its point of application.

$$F_{\mathrm{C},y} = (F_{\mathrm{CH,1,y}} - F_{\mathrm{CH,2,y}}) \cos\alpha + (F_{\mathrm{CH,1,x}} + F_{\mathrm{CH,2,x}}) \sin\alpha , \qquad (4.26a)$$

$$F_{\mathrm{C},x} = (F_{\mathrm{CH,2,y}} - F_{\mathrm{CH,1,y}}) \sin\alpha + (F_{\mathrm{CH,1,x}} + F_{\mathrm{CH,2,x}}) \cos\alpha , \qquad (4.26b)$$

$$M_{\mathrm{C}} = (F_{\mathrm{CH,1,x}} - F_{\mathrm{CH,2,x}}) \frac{h_{\mathrm{C}}}{2} + F_{\mathrm{CH,1,y}} l_{\mathrm{CH,x,1}} - F_{\mathrm{CH,2,y}} l_{\mathrm{CH,y,2}} . \qquad (4.26c)$$
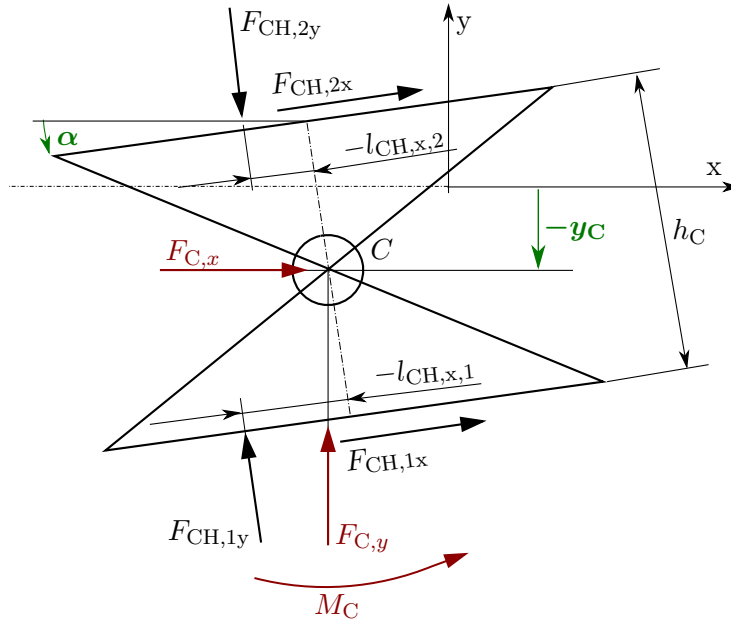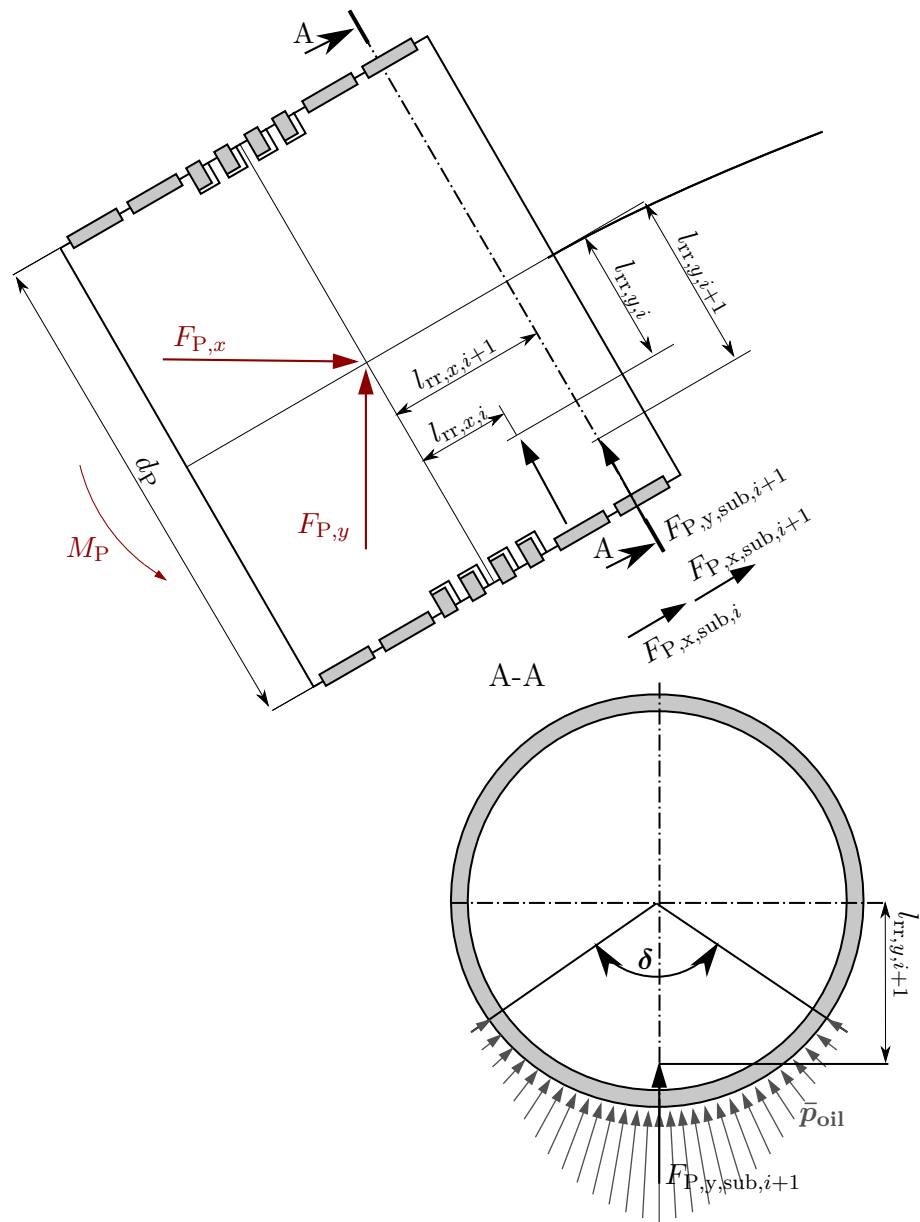
Figure 4.4: Generalized force and moment of global model (shown in red) as well as local forces and its point of applications. The local forces are exemplary shown for two rings.

4.2.3 Piston ring model

Figure 4.5 shows a typical cross section of a piston ring with acting pressures and resultant forces, Fig. 4.6 shows the main parameters which describe the piston ring's geometry and the derived mechanical analogous model. Piston rings are mostly slotted and persist of one or more pieces for an easy placement in the piston ring groove. This makes them very flexible. The piston ring is solidly seated in the groove flank and its beam axis will form a plane curve as long as the contact force lies within the piston groove, which is realistic to assume. The schematic drawing in Fig. 4.5 is rather overdrawn: Usually about 90 % of the ring length lie within the piston groove.

Figure 4.5: Load situation of piston rings;

Figure 4.6: Left: geometrical parameters characterizing ring segment; right: visualization of $q_r = p_1 - p_{\mathrm{oil}}$;

To get the geometry of the lubricated gap the ring's deformation needs to be cal-

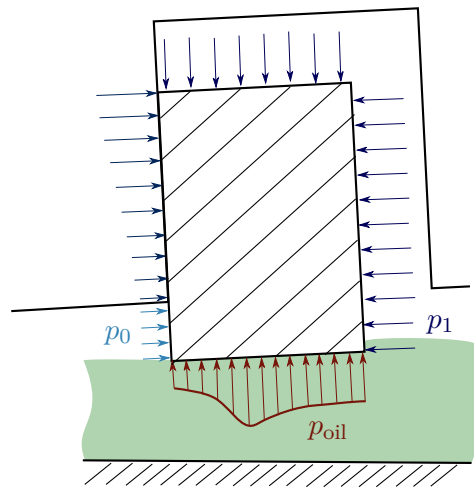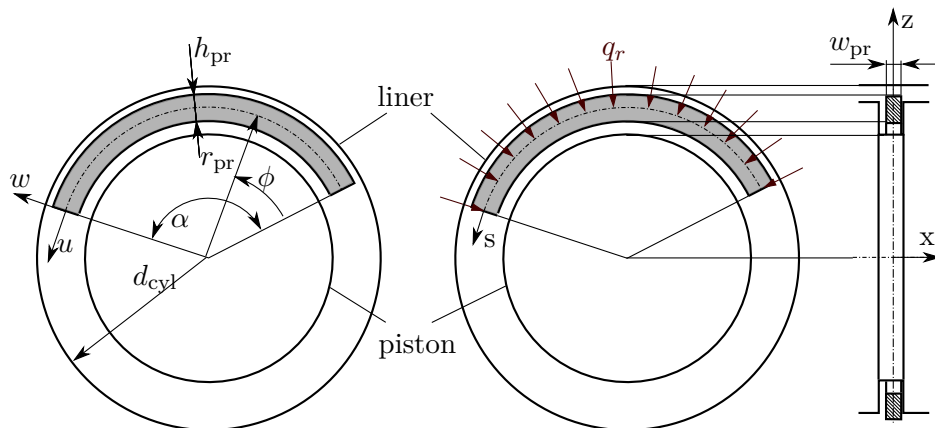culated. It is assumed that local deformations of the ring cross section are negligible: This assumption holds, if deformations w due to uneven oil pressure distributions are negligible smaller compared to the representative gap height c: $w \ll c$. Then, only global ring deformations need to be examined, which is the deformation of the ring axis. The mean pressure $\bar{p}$ as a measure for the force which is transferred from the lubrication gap is

$$\bar{p}_{\text{oil}} = \frac{6\mu U w_{\text{pr}}}{h_1^2} \frac{1}{K^2} \left[\ln \frac{h_0}{h_1} - \frac{2(h_0 - h_1)}{h_0 + h_1} \right],$$

with $K = \frac{h_0}{h_1} - 1$ defining the wedge gap [10]. For $K = \mathscr{O}(1)$ follows

$$\bar{p}_{\text{oil}} = \frac{6\mu U w_{\text{pr}}}{h_1^2} \sim \frac{6\mu U w_{\text{pr}}}{c^2} .$$

The deformation w is estimated by the elastic stress of the piston ring σ_{pr}

$$\sigma_{\text{pr}} \sim E_{\text{pr}} \frac{w}{h_{\text{pr}}} . \tag{4.27}$$

Hence, local deformations can be neglected if the following relation holds true for $w \ll c$:

$$\frac{6\mu U w_{\text{pr}}}{c^2} \sim E_{\text{pr}} \frac{w}{h_{\text{pr}}}. \tag{4.28}$$

Taking this relation and using typical material and ring parameters (see tables 4.1 and 4.2), a gap height $c \sim 1 \times 10^{-5}$ m results in local deformations due to lubrication pressure of about

$$w \sim 1 \times 10^{-6}\,\text{m} , \tag{4.29}$$

which is negligible in first order.

Also, it shall be checked if the dimensions of the ring allow for a hydrodynamic pressure to be built up in the same order as the gas pressure. In other words, if the piston ring is really operated in a hydrodynamic regime or in mixed lubrication. It takes an hydrodynamic pressure of $p_{\text{dyn}} = 1/2(p_1 - p_0)$ for a ring-equilibrium. Hence,

$$c \sim \sqrt{\frac{6\mu U w_{\text{pr}}}{p_{\text{dyn}}}} ,$$

which is 10^{-5} m–10^{-4} m for all configurations shown in table 4.1. These are values in the order of typical values of film heights. As a consequence, the dimensions of typical piston rings allow for operation in hydrodynamic regime without accounting for local deformations.

Curved beam formulation

The relationship between radial displacements and pressure loading of a slotted ring as sketched in Fig. 4.6 is derived based on [43, Ch. 13] by extending its equations by acceleration terms. The following main assumptions are used:

1. Beam axis forms a plane curve. It is only deformed in-plane of the beam axis: This assumption is applicable as long as the contact force $F_{\mathrm{pr,cont}}$ stays within the ring groove $(-h_{\mathrm{pr}}/2 < l_{\mathrm{pr,cont}} < l_{\mathrm{pr,f}})$.

2. cross-sectional dimensions are small compared to the radius of curvature (slightly curved beam): $w_{\mathrm{pr}}, h_{\mathrm{pr}} \ll d_{\mathrm{cyl}}$;

3. Principal axis of inertia of cross-section is normal to beam-plane: This is true for usual ring geometries.

4. All acting forces have to be symmetrical to the beam-plane: This is not true. However, as long as (1) is satisfied, the asymmetry is assumed to be negligible.

5. Strain $(\epsilon)_z$ of beam fibres in distance z from the neutral axis depend linearly from z: $(\epsilon)_z = \epsilon + z\,\epsilon' = \epsilon + z\frac{\partial \chi}{\partial s}$. This assumption is not equivalent to the assumption that cross sections remain flat.

6. The piston ring's geometry is axisymmetric.

From the principle of motion of a ring element in radial direction (see Fig. 4.7) we get

$$Q + \frac{\partial Q}{\partial s}\,\mathrm{d}s + q_r\,\mathrm{d}s - Q - N\,\mathrm{d}\phi + ... = \rho_{\mathrm{pr}} A_{\mathrm{pr}}\,\mathrm{d}s\,\frac{\partial^2 w}{\partial t^2}\ ,$$

here and hereafter dots abbreviate higher-order differentials. With $d\phi \to 0$ this equation leads to

$$\frac{\partial Q}{\partial s} - \frac{N}{r_{\mathrm{pr}}} = -q_r + \rho_{\mathrm{pr}} A_{\mathrm{pr}} \frac{\partial^2 w}{\partial t^2}\ . \tag{4.30}$$

Using the momentum equation of motion we get

$$-M - Q\,\mathrm{d}s + M + \frac{\partial M}{\partial s}\,\mathrm{d}s + ... = \frac{\partial D_{\mathrm{y}}}{\partial t}\ . \tag{4.31}$$

With

$$D_y = \omega_y I_y = \omega_y \rho J_{\mathrm{pr,y}}\,\mathrm{d}s + ...\ ,$$
$$\omega_y = \frac{\partial \chi}{\partial t} = \frac{1}{r_{\mathrm{pr}}}\frac{\partial u}{\partial t} - \frac{\partial^2 w}{\partial t \partial s}\ ,$$
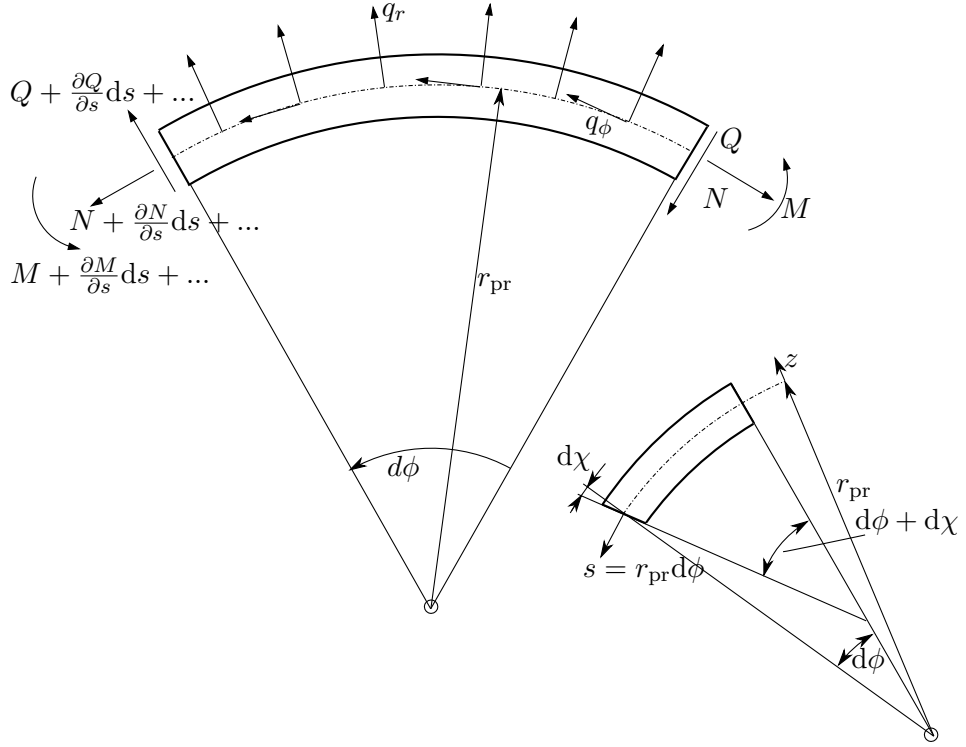
Figure 4.7: Forces acting on ring segment

(4.31) leads to

$$\frac{\partial M}{\partial s} = Q + \rho J_{\mathrm{pr,y}} \left(\frac{1}{r_{\mathrm{pr}}} \frac{\partial^2 u}{\partial t^2} - \frac{\partial^3 w}{\partial t^2 \partial s} \right) . \tag{4.32}$$

The principal of motion in tangential direction for a ring element leads to

$$N + \frac{\partial N}{\partial s} \, \mathrm{d}s - N + Q \, \mathrm{d}\phi + q_\phi \, \mathrm{d}s + ... = \rho A_{\mathrm{pr}} \, \mathrm{d}s \, \frac{\partial^2 u}{\partial t^2} . \tag{4.33}$$

With $d\phi \to 0$ this equation leads to

$$\frac{\partial N}{\partial s} + \frac{Q}{r_{\mathrm{pr}}} = -q_\phi + \rho_{\mathrm{pr}} A_{\mathrm{pr}} \frac{\partial^2 u}{\partial t^2} . \tag{4.34}$$

Assuming $r_{\mathrm{pr}} = \mathrm{const}$, $A_{\mathrm{pr}} = w_{\mathrm{pr}} h_{\mathrm{pr}} = \mathrm{const}$, $\rho_{\mathrm{pr}} = \mathrm{const}$ and using the following

relations

$$\chi = \frac{u}{r_{\mathrm{pr}}} - \frac{\partial w}{\partial s} \, , \tag{4.35a}$$

$$\frac{\partial^2 \chi}{\partial \phi^2} = \frac{1}{r_{\mathrm{pr}}} \frac{\partial^2 u}{\partial \phi^2} - \frac{1}{r_{\mathrm{pr}}} \frac{\partial^3 w}{\partial \phi^3} \, , \tag{4.35b}$$

$$M = \int_{A_{\mathrm{pr}}} \sigma z \, \mathrm{d}A_{\mathrm{pr}} = E_{\mathrm{pr}} J_{\mathrm{pr,y}} \frac{\partial \chi}{\partial s} \, , \tag{4.35c}$$

(4.32) can be rewritten to

$$Q = \frac{1}{r_{\mathrm{pr}}^3} E_{\mathrm{pr}} J_{\mathrm{pr,y}} \left(\frac{\partial^2 u}{\partial \phi^2} - \frac{\partial^3 w}{\partial \phi^3} \right) - \rho J_{\mathrm{pr,y}} \left(\frac{1}{r_{\mathrm{pr}}} \frac{\partial^2 u}{\partial t^2} - \frac{\partial^3 w}{\partial t^2 \partial s} \right) \, . \tag{4.36}$$

Taking the partial derivative of (4.30) with respect to ϕ and using the relation above, (4.36) and (4.30) can be written as

$$\frac{1}{r_{\mathrm{pr}}} \frac{\partial N}{\partial \phi} = \frac{1}{r_{\mathrm{pr}}^4} E_{\mathrm{pr}} J_{\mathrm{pr,y}} \left(\frac{\partial^4 u}{\partial \phi^4} - \frac{\partial^5 w}{\partial \phi^5} \right) - \frac{1}{r_{\mathrm{pr}}^2} \rho_{\mathrm{pr}} J_{\mathrm{pr,y}} \left(\frac{\partial^4 u}{\partial \phi^2 \partial t^2} - \frac{\partial^5 w}{\partial t^2 \partial \phi^3} \right) +$$
$$+ \frac{\partial q_r}{\partial \phi} - \rho A_{\mathrm{pr}} \frac{\partial^3 w}{\partial \phi \partial t^2} \, . \tag{4.37}$$

Inserting these relations in (4.34) and integrating over ϕ leads to the following equation of motion:

$$\frac{1}{r_{\mathrm{pr}}^4} E_{\mathrm{pr}} J_{\mathrm{pr,y}} \left(\frac{\partial^3 u}{\partial \phi^3} - \frac{\partial^4 w}{\partial \phi^4} + \frac{\partial u}{\partial \phi} - \frac{\partial^2 w}{\partial \phi^2} \right) + q_r = -\frac{1}{r_{\mathrm{pr}}^2} \rho_{\mathrm{pr}} J_{\mathrm{pr,y}} \left(\frac{\partial^4 w}{\partial t^2 \partial \phi^2} + \frac{\partial^2 w}{\partial t^2} - \frac{\partial^3 u}{\partial \phi \partial t^2} \right)$$
$$+ \rho A_{\mathrm{pr}} \frac{\partial^2 w}{\partial t^2} + \int_0^\alpha \left[\rho A_{\mathrm{pr}} \frac{\partial^2 u}{\partial t^2} + \frac{1}{r_{\mathrm{pr}}^2} \rho J_{\mathrm{pr,y}} \frac{\partial^2 u}{\partial t^2} - q_\phi \right] \mathrm{d}\phi \, . \tag{4.38}$$

In order to be able to integrate over ϕ it is assumed that both the radial displacement w and the tangential displacement u are continuous differentiable.

Dimensionless formulation

In order to identify any terms which may be neglected, (4.38) shall be formulated in dimensionless form: All dimensioned variables will be marked by a tilde in this

section. The following relations are used:

$\tilde{c}_{g,w}$ ... max reasonable gap between liner and piston ring

$\tilde{c}_{g,u}$ ... max reasonable gap in tangential direction between ring-elements

$\tilde{n}$ ... *rev* per second

$$w = \frac{\tilde{w}}{\tilde{c}_{g,w}} \ , \quad u = \frac{\tilde{u}}{\tilde{c}_{g,u}} \ , \quad t = \tilde{t}\tilde{n} \ , \quad q_r = \tilde{q}_r \frac{1}{\tilde{w}_{pr}\tilde{p}_s} \ , \quad \frac{\partial}{\partial\tilde{t}} = \tilde{n}\frac{\partial}{\partial t} \ ,$$

$$T_1 = \frac{\tilde{E}_{pr}\tilde{J}_{pr,y}\tilde{c}_{g,u}}{\tilde{r}_{pr}^4\tilde{w}_{pr}\tilde{p}_s} \ , \quad T_2 = \frac{\tilde{E}_{pr}\tilde{J}_{pr,y}\tilde{c}_{g,w}}{\tilde{r}_{pr}^4\tilde{w}_{pr}\tilde{p}_s} \ , \quad T_3 = \frac{\tilde{\rho}_{pr}\tilde{J}_{pr,y}\tilde{c}_{g,w}\tilde{n}^2}{\tilde{r}_{pr}^2\tilde{w}_{pr}\tilde{p}_s} \ ,$$

$$T_4 = \frac{\tilde{\rho}_{pr}\tilde{J}_{pr,y}\tilde{c}_{g,u}\tilde{n}^2}{\tilde{r}_{pr}^2\tilde{w}_{pr}\tilde{p}_s} \ , \quad T_5 = \frac{\tilde{\rho}_{pr}\tilde{A}_{pr}\tilde{c}_{g,w}\tilde{n}^2}{\tilde{w}_{pr}\tilde{p}_s} \ , \quad T_6 = \frac{\tilde{\rho}\tilde{A}_{pr}\tilde{c}_{g,u}\tilde{n}^2}{\tilde{w}_{pr}\tilde{p}_s} \ ;$$

In the non-dimensional form, the equation of motion for piston rings (4.38) is written as

$$T_1\left(\frac{\partial^3 u}{\partial\phi^3} + \frac{\partial u}{\partial\phi}\right) + T_2\left(-\frac{\partial^4 w}{\partial\phi^4} + \frac{\partial^2 w}{\partial\phi^2}\right) + q_r = T_3\left(-\frac{\partial^4 w}{\partial t^2\partial\phi^2} - \frac{\partial^2 w}{\partial t^2}\right)$$
$$+ T_4\left(\frac{\partial^3 u}{\partial\phi\partial t^2} + \int_0^\alpha \frac{\partial^2 u}{\partial t^2}\,\mathrm{d}\phi\right) + T_5\frac{\partial^2 w}{\partial t^2} + T_6\int_0^\alpha \frac{\partial^2 u}{\partial t^2}\,\mathrm{d}\phi \ . \tag{4.39}$$

Table 4.1 shows dimensions of typical compressors. Its data represents both big and slow running machines, as well as small and fast running machines. Using this data, possible values for for the dimensionless numbers $T_1, T_2, T_3, T_4, T_5, T_6$ (see table 4.2) are calculated, assuming $\tilde{c}_{g,u} = \tilde{c}_{g,w} = 5 \times 10^{-5}$, $\tilde{\rho}_{pr} = 870\,\mathrm{kg/m^3}$ and $\tilde{E}_{pr} = 1200\,\mathrm{MPa}$. The values for the Young's modulus $\tilde{E}_{pr}$ and the density $\tilde{\rho}_{pr}$ are representative for average plastic compound materials. $\tilde{c}_{g,u}$ and $\tilde{c}_{g,w}$ will vary from case to case, but are in principle tried to be minimized in order to increase efficiency. However, all numbers are less than 1×10^{-4}, even the assumption of much higher values (around $1\,\mathrm{mm}$) would result in $T_1, T_2, T_3, T_4, T_5, T_6 \ll 1$.

These estimations lead to the strongly simplified equation

$$q_r = q_{r,\mathrm{oil}} + q_{r,\mathrm{gas}} = 0 \ , \tag{4.40}$$

where the terms multiplicated with T_1, T_2, T_3, T_4, T_5 and T_6 are neglected. This equation corresponds to the description of a massless, flexible beam, where the forces due to gas– and oil pressure are in equilibrium.

Table 4.1: Parameters of typical reciprocating compressors.

compressor	$\tilde{w}_{\mathrm{pr}}$ [mm]	$\tilde{h}_{\mathrm{pr}}$ [mm]	$\tilde{A}_{\mathrm{pr}}$ [mm^2]	$\tilde{J}_{\mathrm{pr,y}}$ [mm^3]	$\tilde{d}_{\mathrm{cyl}}$ [mm]	stroke [mm]
C1HA	8.9	11	98	987	190	400
C2AR	9.9	13	128	1802	203	89
C3BO	18.3	23.5	430	19759	720	280
C4DR	7.9	9.5	75	560	152	140
C5SS	6.8	8.5	58	349	110	90
C6IT	11.75	18	212	5711	385	320

	rpm	gas type	number of rings	$\tilde{p}_{\mathrm{s}}$ [bar]	$\tilde{p}_{\mathrm{d}}$ [bar]	$\tilde{T}_{\mathrm{d}}$ [°C]
C1HA	370	96% H$_2$	6	30	70	123
C2AR	750	4 N$_2$$^+O_2$	1	2.8	8.2	152
C3BO	420	mixgas	3	3.3	9.2	84
C4DR	800	mixgas	5	13.8	30	72
C5SS	1780	N$_2$	4	11	31	95
C6IT	333	96% H$_2$	7	24.5	50.8	1095

Table 4.2: Non-dimensional parameters of typical reciprocating compressors.

compressor	T_1, T_2	T_2, T_3	T_4, T_5
C1HA	3×10^{-5}	7×10^{-12}	6×10^{-9}
C2AR	4×10^{-4}	5×10^{-10}	3×10^{-7}
C3BO	1×10^{-5}	5×10^{-11}	1×10^{-7}
C4DR	7×10^{-5}	5×10^{-11}	4×10^{-8}
C5SS	3×10^{-4}	6×10^{-10}	3×10^{-7}
C6IT	9×10^{-6}	7×10^{-12}	1×10^{-8}

Dimensionless parameters for configurations shown in table 4.1 for $\tilde{E}_{\mathrm{pr}} = 1200\,\mathrm{MPa}$, $\tilde{\rho}_{\mathrm{pr}} = 870\,\mathrm{kg/m^3}$, $\tilde{c}_{\mathrm{g,w}} = \tilde{c}_{\mathrm{g,u}} = 5 \times 10^{-5}\,\mathrm{m}$;

5 Numerical implementations

First, a simplified lubrication model is implemented in ABAQUS/Standard, which assumes a compressor having an "ideal" crosshead, whose moment M_C and clearance are both zero. This program (see Sec. 5.3) is used to estimate the significance of elastohydrodynamic effects by using ABAQUS/Standard to do a fully coupled simulation to account for elastic deformations of the rider ring. Hence, numerical calculations are embedded in available subroutines of ABAQUS written in Fortran 95.

Since results show (see Sec. 6) that elastohydrodynamic effects are of minor importance, we neglect elastic ring deformations and decouple numerical calculations from ABAQUS subroutines. We chose to use the commercial program MATLAB including its numerous functions for all numerical calculations, resulting in the global cylinder lubrication model (see Sec. 5.4), which covers all considerations and findings found in Sec. 3 and Sec. 4. It is capable of simulating any combination of piston– and rider rings, as found in real compressors and accounts for compressor-specific parameters.

Both programs (the simplified, fully coupled lubrication model and the final global cylinder lubrication model) are based on solving equations for non-dimensional variables. Therefore, all dimensional quantities will be marked by a tilde in this chapter. The following relations are used:

$$\tilde{\alpha} = \frac{\tilde{c}_0}{\tilde{l}_P}\alpha \ , (\tilde{y}_\mathrm{C}, \tilde{q}) = (y, q)\tilde{c}_0 \ ,$$

$$\frac{\partial}{\partial t} = \frac{\partial}{\partial \Theta}\tilde{\omega} \ ,$$

$$\tilde{x} = \tilde{B} \cdot x \ , \qquad \tilde{z} = \tilde{B} \cdot z \ , -0.5 \le x \le 0.5 \ ,$$

$$(\tilde{v}, \tilde{w}, \tilde{h}) = \tilde{c} \cdot (v, w, h) \ ,$$

$$\tilde{t} = \frac{\Theta}{2\tilde{n}\pi} \ , \qquad \Omega = \frac{2\tilde{B}\tilde{\omega}}{\tilde{U}_\mathrm{m}} \ ,$$

$$\tilde{p} = \tilde{p}_r p = \frac{6\tilde{U}_\mathrm{m}\tilde{B}\tilde{\mu}_{\mathrm{f},0}}{\tilde{c}_0^2}p \ ,$$

$$\tilde{U} = U\,\tilde{U}_\mathrm{m} = U \cdot 2 \cdot \mathrm{stroke} \cdot \mathrm{rpm}/60 \ ,$$

$$\tilde{\mu}_\mathrm{f} = \tilde{\mu}_{\mathrm{f},0}\mu \Rightarrow \mu = 1 \quad \text{for } \tilde{\mu}_\mathrm{f} = \mathrm{const} \ ;$$

5.1 Implementation of submodels and routines used in the global models

Before explaining the implementation of the simplified, fully coupled lubrication model and the global cylinder lubrication model, we describe the implementation of the various submodels which will be used, starting with the description of the implementation of the Reynolds equation for fully flooded ring regions.

5.1.1 Implementation of the Reynolds equation for fully flooded ring regions (ABAQUS/Standard & MATLAB)

The implementations adopt the considerations shown in Sec. 3.5: The pressure field of the fully flooded regions (regions between cylinder wall and rings, and between crosshead and crosshead guide) is obtained by solving the unsteady Reynolds equation (2.6). Non-dimensionally, the Reynolds equation reads

$$\frac{\partial}{\partial x}\left(h^3\frac{\partial p}{\partial x}\right) + \frac{\partial}{\partial z}\left(h^3\frac{\partial p}{\partial z}\right) = U\frac{\partial h}{\partial x} + \Omega\frac{\partial h}{\partial \Theta} \ . \tag{5.1}$$

The numerical solution is performed by using the finite volume method (2D for the crosshead calculation, and either 1D or 2D for the ring-calculation) on a fixed and rectangular grid. Since the localization of pressure gradients is a priori not possible, local refinements of the grid are not useful and are not pursued. A rectangular ring- and crosshead profile can be parametrically generated, resulting in equidistant meshes. It is also possible to consider profiled rings: A third-party mesh generator, which is capable of the ABAQUS/Standard syntax is needed to generate the mesh, which can be imported afterwards.

The computational points are placed in the centre of the elements, additional points are also placed at the open borders to account for the boundary conditions (oil pressure equals gas pressure). The gas pressure is prescribed at all cell nodes, which are exposed to the gas pressure. They are located in the starved ring regions. In addition, if starved lubrication occurs, we move the outer nodes of the fully flooded regions to the oil front in order to prescribe the boundary conditions correctly — see Fig. 5.1 for a visual explanation. The Reynolds equation is integrated for each volume, P, and its adjacent volumes, using the nomenclature shown in Fig. 5.2:

$$\int\limits_s^n \int\limits_w^e \left[\frac{\partial}{\partial z}\left(h^3\frac{\partial p}{\partial z}\right) + \frac{\partial}{\partial x}\left(h^3\frac{\partial p}{\partial x}\right) - U\frac{\partial h}{\partial x} - \Omega\frac{\partial h}{\partial \Theta}\right] \mathrm{d}z\,\mathrm{d}x = 0 \ . \tag{5.2}$$

Linear interpolation with an accuracy of second order — equivalent to the central difference approximation of the first derivation of the finite difference method — is used to derive values at the centre of volume sides (w, e, s, n) [20]. Taking side e, for
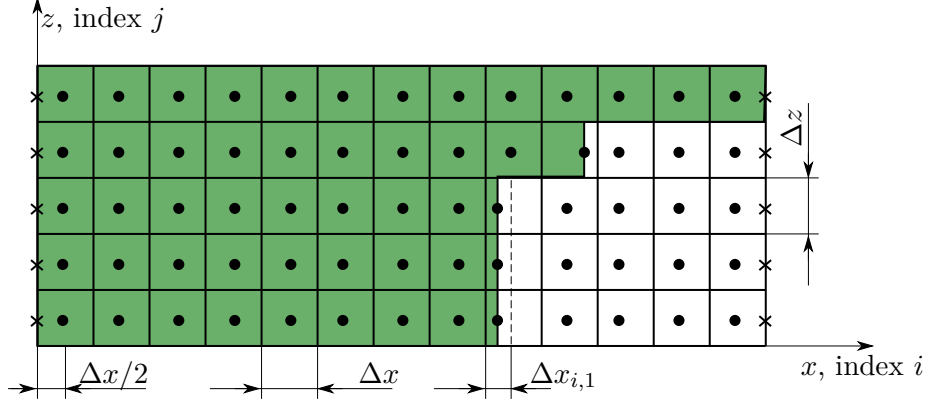
Figure 5.1: Mesh of domain: •: represents nodes at the centre of finite volumes, × represents nodes at outer boundaries; The green area represents the fully flooded ring region. The outer nodes are moved to the borders for correct implementation of the boundary conditions.

instance, we get for a value Φ

$$\Phi_e \approx \Phi_E \lambda_e + \Phi_P \left(1 - \lambda_e\right) \ , \tag{5.3}$$

with the linear factor of interpolation λ_e, which is defined as

$$\lambda_e = \frac{x_e - x_P}{x_E - x_P} \ . \tag{5.4}$$

The gradient at position e is approximated by assuming a linear profile between Node P and E

$$\left(\frac{\partial \Phi}{\partial x}\right)_e \approx \frac{\Phi_e - \Phi_P}{x_E - x_P} \ . \tag{5.5}$$

This approximation is of second order for equidistant meshes. For non-equidistant meshes, the reduction of error is similar to the reduction of error for equidistant meshes, even though the approximation is formally of first order [20].

These linear interpolations lead to the following discretized terms

$$\int\limits_s^n \int\limits_w^e \left[\frac{\partial}{\partial x}\left(h^3 \frac{\partial p}{\partial x}\right)\right] \mathrm{d}x \, \mathrm{d}z = \left[h_e^3 \frac{p_E - p_P}{dx_e} - h_w^3 \frac{p_P - p_W}{dx_w}\right] \Delta z_P \ , \tag{5.6a}$$

$$\int\limits_s^n \int\limits_w^e \left[\frac{\partial}{\partial z}\left(h^3 \frac{\partial p}{\partial z}\right)\right] \mathrm{d}x \, \mathrm{d}z = \left[h_n^3 \frac{p_N - p_P}{dz_n} - h_s^3 \frac{p_P - p_S}{dz_s}\right] \Delta x_P \ , \tag{5.6b}$$

$$\int\limits_s^n \int\limits_w^e \left[-U \frac{\partial h}{\partial x} - \Omega \frac{\partial h}{\partial \Theta}\right] \mathrm{d}x \, \mathrm{d}z = -U \left[h_e - h_w\right] \Delta z_P - \Omega \frac{\partial h}{\partial \Theta} \Delta z_P \Delta x_P \ . \tag{5.6c}$$
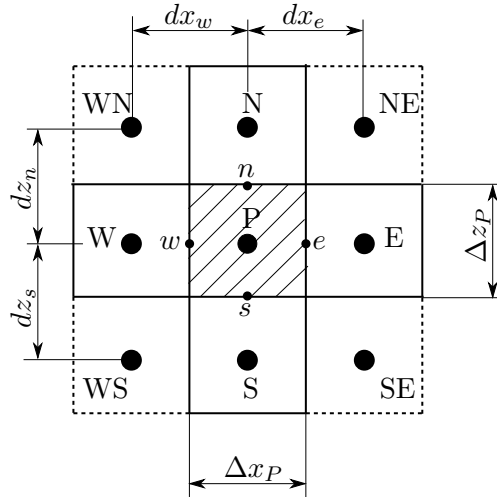
69

Figure 5.2: Typical control element: illustration of used indices;

By applying expressions (5.6) in (5.2) we get a linear system of equations of the form

$$A_P\, p_P + A_E\, p_E + A_N\, p_N + A_W\, p_W + A_S\, p_S + S_c = 0 \ . \qquad (5.7)$$

Attention must be paid to the realization of the boundary conditions: For the discretisation of the outer boundary condition, Δx is replaced by $\Delta x/2$. For the implementation of the inner boundary conditions at the oil front next to the starved region, we will need to update the front cell's width.

For the calculation of the pressure field between crosshead guide and crosshead, the hydrostatic pressure of the lubrication grooves needs to be prescribed. This is done for all nodes which are located inside these grooves.

The linear system of equations (5.7) is solved differently depending on the formulation: In case of the EHL-formulation (simplified, fully coupled lubrication model), which takes the elastic deformations of the rider ring into account, the FORTRAN 77 SLATEC-Mathematical Subroutine Library [52], specifically the subroutine "DG-BSL" is used, which solves the double precision band system $A * X = B$. MATLAB is used to solve the global cylinder lubrication model (which neglects elastohydrodynamic effects), in detail the backslash operator is used.

5.1.2 Front tracking and balancing routines

Oil front tracking as well as the evaluation of the transition zones and of the oil film thickness on the cylinder wall next to the transition zones is done via mass balancing, using two computational grids: a computational grid for the ring regions (rings have zero relative velocity) and a computational grid for the cylinder region (coordinate system is at rest). The transition zone moves along with the ring regions, leaving a trace of oil on the cylinder grid, proportional to the gap height.

The focus lies on the conservation of oil mass, errors due to coarse discretisation

are compensated: Analytically, the oil volume in the gap between ring and cylinder (1D) at time-step n for row j is

$$V_{\text{ring},j}^{(n)} = V_{\text{ring},j}^{(n-1)} + \left(q_{\text{trans}_w,\text{e},j}^{(n)} - q_{\text{trans}_e,\text{w},j}^{(n)} \right) , \tag{5.8}$$

$\tilde{q}$ denotes the oil flow through cell borders or oil fronts (per unit depth), as explained in Sec. 3.5. The corresponding dimensionless values (q, V) are defined as $(q, V) = (\tilde{q}, \tilde{V}) \tilde{b}_P \tilde{c}$. However, due to discretisation errors, this equation is violated. In case of high pressure gradients, the size of this error can falsify the mass flow in a low single-digit percentage area (up to 2%). Therefore, this error res_{ring} is tracked and is additionally added to the cell upstream of the fully flooded ring region. If the ring is fully flooded, res_{ring} is added to the outer transition zone upstream of the ring. Taking the exemplary case of Fig. 5.3, the mass balancing terms for the transition zones and the cells next to them read

$$\text{res}_{\text{ring}}^{(n)} = \left(q_{\text{trans}_w,\text{e}}^{(n)} - q_{\text{trans}_e,\text{w}}^{(n)} \right) - \left(V_{\text{ring}}^{(*)} - V_{\text{ring}}^{(n-1)} \right) , \tag{5.9a}$$

$$V_{\text{ring}}^{(n)} = V_{\text{ring}}^{(*)} + \text{res}_{\text{ring}}^{(n)} , \tag{5.9b}$$

$$V_{\text{trans}_w}^{(n)} = V_{\text{trans}_w}^{(n-1)} + \left(q_{\text{trans}_w,\text{w}}^{(n)} - q_{\text{trans}_w,\text{e}}^{(n)} \right) , \tag{5.9c}$$

$$V_{\text{trans}_e}^{(n)} = V_{\text{trans}_e}^{(n-1)} + \left(q_{\text{trans}_e,\text{w}}^{(n)} - q_{\text{trans}_e,\text{e}}^{(n)} \right) , \tag{5.9d}$$

$$V_{\text{oil,w}}^{(n)} = V_{\text{oil,w}}^{(n-1)} + q_{\text{trans}_w,\text{w}}^{(n)} , \tag{5.9e}$$

$$V_{\text{oil,e}}^{(n)} = V_{\text{oil,e}}^{(n-1)} + q_{\text{trans}_e,\text{e}}^{(n)} . \tag{5.9f}$$

The mass of the cylinder cells underneath the ring is zero; the mass of all other cells is kept constant.

Figure 5.3: Nomenclature needed for mass balancing equations.

Finally the oil volumina of cells in a starved lubricated zone is defined (see Fig. 3.6 in Sec. 3.5.2). Equation 5.10 describes the oil volume of the cell in the inner transition zone:

$$V_{\text{film,P}}^{(n)} = V_{\text{film,P}}^{(n-1)} + (q_{\text{e}}^{(n)} - q_{\text{film,e}}^{(n)}) , \tag{5.10}$$

Note, that q_e is defined using the travelled distance of the piston over last time

interval — see (3.15), but does not account for any movement of the oil front. However, since the oil volume is tracked, this does not result in any oil loss or oil generation, because $\mathrm{res}_{\mathrm{ring}}^{(n)}$ accounts for all discretisation errors.

Concerning all other cells in the starved lubrication zone, (3.12) is discretized using the conservative standard first-order upwind method (see also Fig. 5.4)

$$h_{\mathrm{film,P}}^{(n)} = h_{\mathrm{film,P}}^{(n-1)} - \frac{U\Delta t}{\Delta x}\left(h_{\mathrm{film,P}}^{(n-1)} - h_{\mathrm{film,W}}^{(n-1)}\right) \qquad \text{for } U > 0 \ , \qquad (5.11a)$$

$$h_{\mathrm{film,P}}^{(n)} = h_{\mathrm{film,P}}^{(n-1)} - \frac{U\Delta t}{\Delta x}\left(h_{\mathrm{film,P}}^{(n-1)} - h_{\mathrm{film,E}}^{(n-1)}\right) \qquad \text{else} \ . \qquad (5.11b)$$

The term $U\Delta t$ is the traveled distance of the piston over the last time interval.

Figure 5.4: VOF-Schema;

The maximal allowable time step size is chosen to fulfil the CFL condition

$$0 \leq \frac{U\Delta t}{\Delta x} \leq 0.8 \ , \qquad (5.12)$$

with Δx being the minimal cell width in x-direction, taking into account both computational grids.

The front tracking has already been explained in Sec. 3.5.1: It is done using the volume fraction F — see (3.11). However, using this formulation, non-physical oil overshoots ($F > 1$) can occur. These are corrected by adding these oil volumina to the neighbouring cells.

5.1.3 Implementation of the 2-equations gas pressure model (MATLAB)

The implementation of the 2-equations gas pressure model (3.50) is straight forward. The assumptions mentioned in Sec. 3.7 are applied, the ODE-solver "ode45" is used. Since constant ϕ_{valve}-values are used, this model can be solved in advance to the main compressor program. Results (pressure levels) are saved and can be used by the lubrication models.

5.1.4 Implementation of the piston ring model (MATLAB)

The piston ring model is implemented strictly 1D: Due to the flexibility of the piston rings this is valid for the calculation of the radial displacements of the ring axis, see (4.40). However, the 1D-assumption does not necessarily need to be valid for the pressure calculation. This assumption will later be justified in Sec. 6 by comparing the pressure profiles of a ring calculation, calculated by the 1D-Reynolds equation and by the 2D-Reynolds equation. The nomenclature of all forces and lengths used in this model are shown in Fig. 5.5.

The radial forces per unit depth due to oil– ($\tilde{F}_{\text{oil}}$) and gas pressure ($\tilde{F}_{1b}$) need to be in equilibrium. Hence

$$\tilde{q}_r = \tilde{F}_{1b} - \tilde{F}_{\text{oil}} - \sum_i \tilde{F}_i = 0 \ , \tag{5.13}$$

with $\tilde{F}_i$ being the spring forces according to Sec. 3.3 and

$$\tilde{F}_{\text{pr},1b} = \tilde{p}_1 \cdot \tilde{w}_{\text{pr}} \ . \tag{5.14}$$

This equation is solved for every line j (see Fig. 5.1) for the unknown $\tilde{y}_{\text{pr}}(\phi)$ using the MATLAB routine "fzero". $\tilde{y}_{\text{pr}}$ is the ring displacement along the piston groove, it is assumed positive when pointing to the cylinder's wall. The solution of the last time step is used as an initial guess for "fzero". This works well, as long as the profile is not fully in contact. However, once this is the case, the gap's profile is constant — there is no pressure built up due to the wedge effect because of the simplified model. In a more complicated model, which accounts for elastic deformations, ring deformations would result in a convergent gap which in turn allows for a pressure built up. To overcome this problem, the ring is assumed to be stiff for the contact formulation: Hence, the gap's profile will always correspond to the piston tilt and allows for the wedge effect. The error arising from this is small due to the small gap heights: Regions, which are in contact, hardly contribute to the total oil-volume flow. Above all, due to the strict 1D implementation, other regions of the piston ring, which are not in contact, are not affected by this simplification.

To validate the assumption that the piston ring sits solidly in the groove flank, the contact force between piston and piston ring, as well as its point of application may be tracked. This assumption is valid as long as the point of application is positioned

on the contact line between ring groove and ring:

$$-\frac{\tilde{h}_{\text{pr}}}{2} < \tilde{l}_{\text{pr,cont}} < \tilde{l}_{\text{pr,f}} \, . \tag{5.15}$$

In order to check this relation, the following terms need to be defined:

$$\tilde{F}_{\text{pr},1a} = \tilde{p}_1 \cdot \tilde{h}_{\text{pr}} \, , \tag{5.16a}$$

$$\tilde{F}_{\text{pr},1c}(\phi) = \tilde{p}_1 \left(\frac{\tilde{h}_{\text{pr}}}{2} + \tilde{l}_{\text{pr},f}(\phi) \right) \frac{\tilde{p}_0 + \tilde{p}_1}{2} \, , \tag{5.16b}$$

$$\tilde{F}_{\text{pr},2}(\phi) = \tilde{p}_0 \left(\frac{\tilde{h}_{\text{pr}}}{2} - \tilde{l}_{\text{pr},f}(\phi) \right) \, , \tag{5.16c}$$

$$\tilde{F}_{\text{pr,cont}}(\phi) = \tilde{F}_{\text{pr},1a} - \tilde{F}_{\text{pr},2}(\phi) - \tilde{F}_{\text{pr},1c}(\phi) \, , \tag{5.16d}$$

$$\tilde{l}_{\text{pr,f}}(\phi) = \tilde{l}_{\text{pr,f},0} - \tilde{y}_{\text{pr}}(\phi) - \left(\tilde{y}_{\text{P}} \cos\phi - 0.5\xi^2 \lambda \cos^2(\phi)\tilde{c} \right) \, , \tag{5.16e}$$

$$\tilde{l}_{\text{pr,cont}}(\phi) = \frac{1}{\tilde{F}_{\text{pr,cont}}(\phi)} \left[\tilde{F}_{\text{pr},1c}(\phi) \left(\frac{\tilde{h}_{\text{pr}}}{4} - \frac{\tilde{l}_{\text{pr,f}}(\phi)}{2} \right) \right.$$
$$\left. - \tilde{F}_2(\phi) \left(\frac{\tilde{h}_{\text{pr}}}{4} + \frac{\tilde{l}_{\text{pr,f}}(\phi)}{2} \right) - \tilde{F}_{\text{pr,oil}}(\phi)\tilde{l}_{\text{pr,x}}(\phi) \right] \, , \tag{5.16f}$$

with $\tilde{l}_{\text{pr,f},0}$ being the the initial distance of the ring's lubricated surface to the piston (initial $\tilde{l}_{\text{pr,f}}$). These relations hold true for $\tilde{p}_1 > \tilde{p}_0$, where the ring is assumed to stay on the left side of the ring groove. As soon as $\tilde{p}_1 \leq \tilde{p}_0$, the ring shuttles instantaneous to the other side. The shuttle time due to the ring's inertia and due to oil sticking effects is neglected.
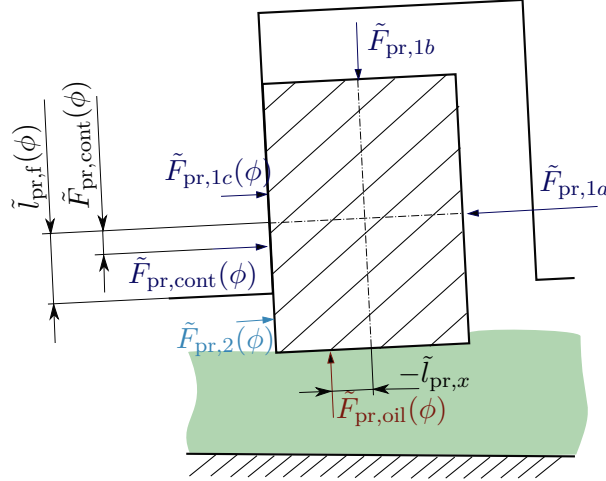

Figure 5.5: Mechanical analogous model of piston ring

5.2 CFD: compression model (FLUENT)

The intention of this model is the estimation of wall shear stresses on the cylinder wall of typical compressors to estimate the order of magnitude of gas driven oil flow. This is done by taking the exemplary compressor C2AR, shown in table 4.1. Its — in this context — relevant data is summarized in table 6.1: It is a reciprocating compressor, having on each side (crank-end and head-end) one discharge– and one suction valve. The rider ring is placed in the middle of the piston, which allows the piston to overrun the valve-clearances. Therefore, the open sectional area between compression region and valve-clearance is reduced at the end of each cycle. Geometrical valve data was not available, therefore, the geometry of a the compressor is measured manually to create a 3D-model. Attention shall be drawn to the coordinate system which is used for the CFD calculation. It differs from the so far used coordinate system in defining the y-direction to be the axial direction of the cylinder.

The numerical simulation of a compression cycle is done using FLUENT. The focus lies on the correct representation of the gas flow inside the compression chamber. The flow through the valves is not from interest and should be modelled such that the flow in the compressor channel is hardly affected by any simplifications. Therefore, a detailed modelling of the gas flow through suction- and discharge valve is not done. Instead, the mass flow through the valves is given using the Saint–Venant–Wantzel equation (3.51). The suction valve is modelled to close and open instantaneously. In case of the discharge valve, this valve model results in convergence issues. Therefore, more realistic, time-dependent empirical values for ϕ_{valve} are used: ϕ_{valve} equals zero until a certain differential pressure is reached, then its values increase by a quadratic characteristic until a maximum is reached after $1\,\mathrm{ms}$. This value is maintained until closure ($\tilde{\phi}_{\mathrm{valve}} = 0$).

5.2.1 Settings and Boundary conditions

For most settings the FLUENT-default values were used. To solve the transient calculation, the URANS equations are used to compute the time dependent flow. The first order implicit formulation is chosen with a constant time step of $\Delta\Theta = 0.05$. Air is assumed to behave like a compressible, ideal gas. The SST k-omega turbulence model [41] is chosen, which is recommended for high accuracy boundary layer simulations.

The cylinder wall is defined as a Sliding Interface consisting of the cylinder wall and the interface area between cylinder region and valve clearance volume. When the piston reaches the valve clearance volume, the open surface reduces and the interface area becomes a wall region (see Fig. 5.7).

The mass flow through the suction valve is defined using the mass flow inlet boundary condition. It is more complex to define the mass flow outlet, since there is no such boundary condition implemented in the used Fluent version. Hence, the mass flow through the discharge valve is modelled via a porous media. The porous

media mode is in detail explained in the ANSYS FLUENT Theory Guide [1]. Using a porous media in Fluent, the pressure loss in the flow is proportional to the fluid velocity squared in the cell, determined via an addition of a momentum source term to the standard fluid flow equations. It is composed of a viscous loss term (Darcy, the first term on the right-hand side of (5.17)) and an inertial loss terms (the second term on the right-hand side of (5.17))

$$\tilde{S}_i = -\left(\frac{\tilde{\mu}_\mathrm{g}}{\tilde{\alpha}} \tilde{v}_i + \tilde{C}_2 \frac{1}{2} \tilde{\rho}_\mathrm{g} |\tilde{v}| \tilde{v}_i \right) , \tag{5.17}$$

where $\tilde{S}_i$ is the source term for the ith (x, y, or z) momentum equation for a homogeneous media, $\tilde{\alpha}$ is the permeability and $\tilde{C}_2$ is the inertial resistance factor[1]. The pressure drop due to inertial losses is

$$\nabla \tilde{p} = -\sum_{j=1}^{3} \tilde{C}_{2_{ij}} \left(\frac{1}{2} \tilde{\rho}_\mathrm{g} \tilde{v}_j |\tilde{v}| \right) . \tag{5.18}$$

In our case, we are interested in a pressure loss in z-direction leading to

$$\frac{\Delta \tilde{p}}{\Delta \tilde{z}} = \left(\frac{\tilde{\rho}_0}{2} \tilde{w}^2 \right) \tilde{C}_2 , \tag{5.19}$$

where $\tilde{C}_2$ is the superficial velocity inside the porous medium, based on the volumetric flow rate, to ensure continuity of the velocity vectors across the porous medium[1]. Making use of (3.53), which describes the pressure-dependent mass flow through the valve,(5.19) and the relationship

$$\dot{\tilde{m}} = \tilde{\rho}_\mathrm{g} \tilde{w} \tilde{A}_\mathrm{por} , \tag{5.20}$$

we get

$$\tilde{C}_2 = \frac{\tilde{A}_\mathrm{por}^2}{\epsilon_\mathrm{c}^2 \tilde{\phi}_\mathrm{valve}^2 \tilde{t}_\mathrm{por}} . \tag{5.21}$$

For the pressure $\tilde{p}_0$ and density $\tilde{\rho}_0$, which are needed to define the compressibility ϵ_c, we use the average stagnation values in the discharge valve clearance volume

$$\tilde{p}_0 = \tilde{p} \left(1 + \frac{\kappa - 1}{2\kappa} \frac{\tilde{\rho}_\mathrm{g} \left| \vec{\tilde{u}} \right|^2}{\tilde{p}} \right)^{\frac{\kappa}{\kappa - 1}} , \tag{5.22}$$

$$\tilde{\rho}_0 = \tilde{\rho}_\mathrm{g} \left(\frac{\tilde{p}_0}{\tilde{p}} \right)^{\frac{1}{\kappa}} . \tag{5.23}$$

Equation (5.22) follows from the stationary energy equation along a streamline and the definition of isentropy. For the pressure $\tilde{p}$ and density $\tilde{\rho}$ we take the averaged values from the discharge-valve pocket. In case, the average stagnation pressure

$\tilde{p}_0 > \tilde{p}_s$, $\tilde{C}_2$ is prescribed using the definition of ϵ_c shown in (3.52). If not, $\tilde{C}_2 = 1 \times 10^{20}$, and the pressure at the outer side of the porous region is prescribed to have the same value as on the inner side to prevent any mass flow. This indirect approach to define $\tilde{C}_2$ is used, since $\tilde{\phi}_{\text{valve}}$ is usually the only known valve-parameter.

Any calculations are done at the end of each increment, using the user defined subroutine (UDF) "DEFINE_EXECUTE_AT_END". The values are then assigned using the UDF "DEFINE_PROFILE".

5.2.2 Mesh

The motion of the piston is modelled via the FLUENT built-in function (In-Cylinder option), which is used to define the time dependent position of the piston. The mesh of the deforming cylinder region is updated each time step using the Dynamic Layering Method. All other mesh regions (suction- and discharge valve-clearance regions) are stationary and have unstructured tetrahedral meshes due to their relatively complex geometries. The wall boundaries are meshed with layered hexahedral elements to capture boundary layer effects. Figures 5.6 and 5.7 show the resulting mesh.

5.3 Formulation of the EHL problem (coupled ABAQUS/Standard)

The decision to use the FE-method to solve the fully coupled EHL problem offers the ability to simulate rather complex rider-ring geometries with different profiles.

The strong interaction between the elastic deformations of the rider ring and the pressure distribution is implemented by user defined subroutines. The ABAQUS solver is used to calculate the deformations of the rider ring, while the implemented code in the user-subroutines defines the deformation-dependent pressure distribution, eccentricity and tilt of the piston (see Fig. 5.8). The rider ring's material is assumed to be isotropic and homogeneous. However, its material properties could easily be adjusted.

This model aims to show the significance of elastohydrodynamic deformations. Hence, we try to reduce as much complexity as possible in order to solely focus on elastohydrodynamic effects. As a side effect, the extensive computational time is reduced: We assume a fully flooded gap as well as an ideal piston-crosshead assembly: It is assumed to be rigid ($\tilde{q} = 0$), zero clearance between crosshead and crosshead guide is assumed ($\tilde{y}_C = 0$), as well as a zero crosshead moment $M_C = 0$. These assumptions lead to a drastically simplified 1-DOF dynamical system with one remaining equation of motion (compare to (4.11)–(4.13)):

$$\tilde{F}_{\text{P},y} = \frac{\tilde{l}_{\text{S2}}}{\tilde{l}_{\text{S}}} \tilde{m} \left(\tilde{\text{g}} - \alpha \ddot{\tilde{x}}_{\text{C}} \right) - \ddot{\alpha} \frac{1}{\tilde{l}_{\text{P}}} \left(m \tilde{l}_{\text{S2}}^2 + \tilde{I}_{\text{S}} \right) \tag{5.24}$$
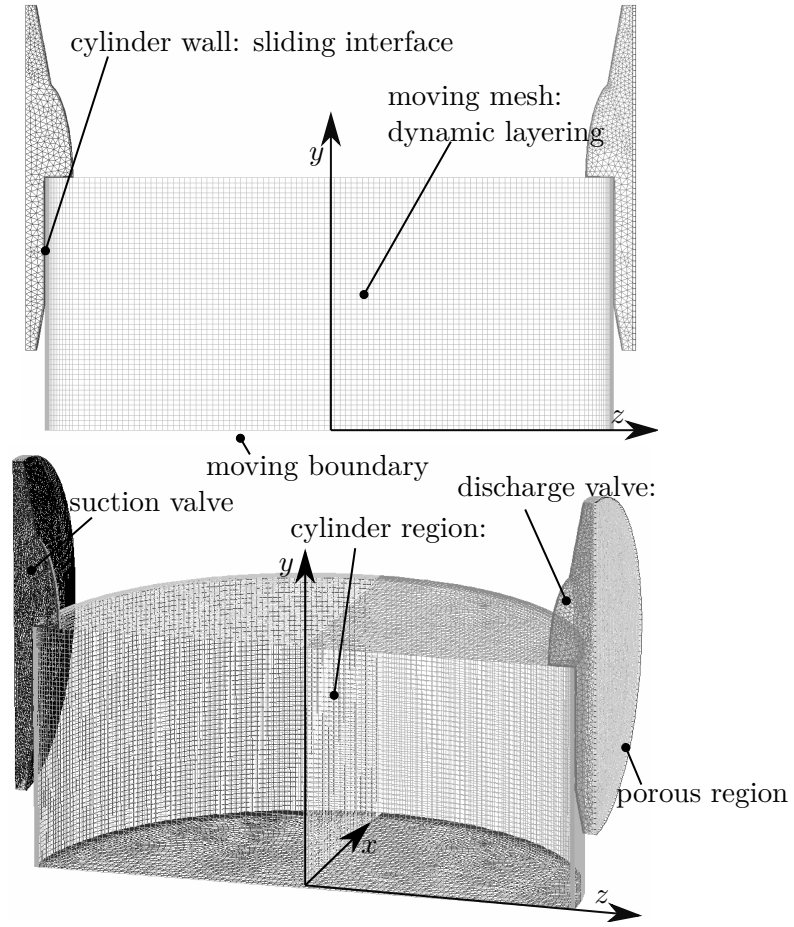
Figure 5.6: Mesh of CFD-C2AR-compressor model; top: symmetry plane; bottom: 3D view;

and the following relationship between tilt α and eccentricity $\tilde{y}_P$:

$$\tilde{y}_P = -\tilde{l}_P\, \alpha \ . \tag{5.25}$$

S denotes the centre of mass of the piston–piston rod–crosshead assembly, $\tilde{l}_S$ is the distance between point of contact of $\tilde{F}_{P,y}$ and S, and $\tilde{l}_P$ is the distance between point of contact of $\tilde{F}_{P,y}$ and crosshead bearing, $\tilde{l}_{S2} = \tilde{l}_P - \tilde{l}_S$. $\tilde{I}_S$ and $\tilde{m}$ are the mass moment of inertia and total mass of the simplified system.

The FE-model is shown in Fig. 5.9. The rider ring is assumed to seat solidly on the piston, which in turn is allowed to have a tilt relatively to the cylinder axis. Therefore, the radial degree of freedom of all inner nodes (nodes on blue surface in Fig. 5.9) is restrained in a local coordinate system coupled to the reference point RP_{ring}. This point can be rotated around the z-axis of the global coordinate system according to the piston tilt α and displaced along the y-axis, corresponding to the
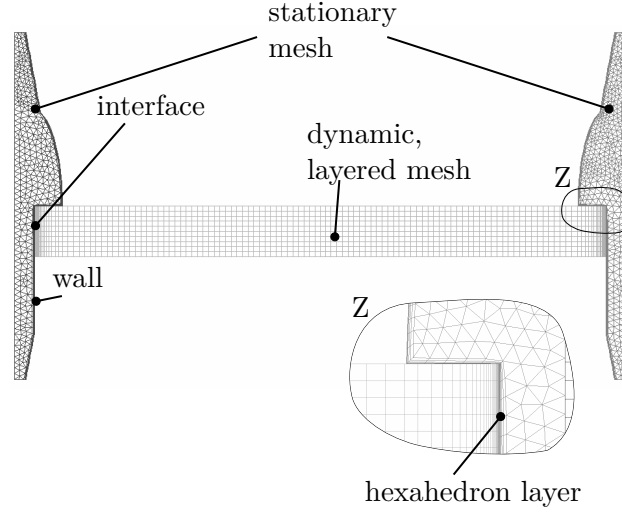
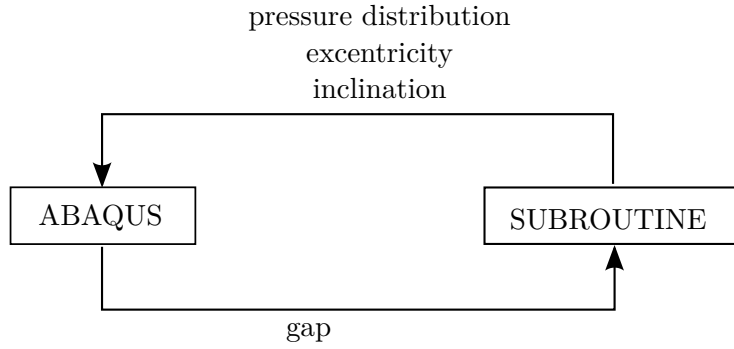Figure 5.7: Mesh of CFD-C2AR-compressor model at $\Theta = 123°$;

Figure 5.8: Interaction between Abaqus solver and user subroutines.

piston eccentricity. Symmetry around the x-y plane is assumed. The loads as well as the translation (y_P) and rotation (tilt α) of $\mathrm{RP_{ring}}$, which is the origin of the local coordinate system, are defined through user subroutines and are solution dependent. The reaction force of Node $\mathrm{RP_{ring}}$ equals the sum of all forces acting on the system and corresponds to $-\tilde{F}_{\mathrm{P},y}$.

The geometries of the simulated rider rings are assumed to be axisymmetric. Due to the loading condition of the ring (pressure load, hardly any bending), shear locking is not expected. Therefore, linear hexahedrons are used to mesh the geometries. Contact forces are defined for any nodes, whose gaps are below $\mathrm{gap_{min}}$ (see Sec. 3.3).

To solve this fully coupled EHD problem, an algorithm (see algorithm 1), which is using the residual definitions in (5.29), is used. It contains three loops:

- time-loop (superscript n): as soon as film thickness ($\epsilon_h < \mathrm{limit_h}$), pressure distribution ($\epsilon_p < \mathrm{limit_p}$) and reaction force show converged values, and the pressure forces balance the mass forces ($\epsilon_{\mathrm{RF}} < \mathrm{limit_{RF}}$) the crank angle is

increased. The eccentricity of the next time loop is guessed by a quadratic function, using the solutions of the last three time steps.

- eccentricity-loop (superscript p): film thickness, pressure distribution and re-action force show converged values, but $\epsilon_{\mathrm{RF}} > \mathrm{limit}_{\mathrm{RF}}$: adapt eccentricity of rider ring with Newton-Raphson algorithm;

- inner-loop (superscript q): the pressure distribution is changing significantly: eccentricity is not changed, solve Reynolds equation to update oil pressure distribution due to changed elastic deformations;

Underrelaxation is used for both the gap distribution as well as the pressure distribution:

$$p_{\mathrm{FE},k}^{(n,q,p)} = R\,p_k^{(n,p,q)} + (1-R)p_{\mathrm{FE},k}^{(n,p,q-1)} \;, \tag{5.26a}$$

$$h_{\mathrm{FE},k}^{(n,q,p)} = R\,h_k^{(n,p,q)} + (1-R)h_{\mathrm{FE},k}^{(n,p,q-1)} \;. \tag{5.26b}$$

The value p_k denotes the calculated pressure via Reynolds equation, $p_{\mathrm{FE},k}$ the applied, under-relaxated pressure, h_{FE} is the under-relaxated gap used for pressure calculation, h denotes the current gap distribution — a result of the FE-calculation. The relaxation factor R is set depending on the current clearance $c^{(n)}$:

$$R = R_0 + \left(\frac{\tilde{c}^{(n)}}{1 \times 10^{-5}} - 1 \right) \frac{1}{70} \;. \tag{5.27}$$

Calculations have shown the importance of using the 2D-formulation of the Reynolds equation to calculate the pressure distribution: Even though the pressure gradients in azimuthal direction of the converged solution are negligible, the convergence behaviour improves significantly using the 2D-formulation, especially in regions of small clearances ($< 10\,\mu\mathrm{m}$). The time step size accounts for the system's convergence behaviour: It increases with increasing clearances, but is limited by minimum and maximum values:

$$\Delta\Theta = \Theta_0 \frac{\pi}{180} + \left(\frac{\tilde{c}}{1 \times 10^{-5}} - 1 \right) \frac{1}{10} \frac{\pi}{180} \;,$$

$$\Theta_0 \frac{\pi}{180} \leq \Delta\Theta \leq 1.5 \frac{\pi}{180} \tag{5.28}$$

The parameters R_0 and Θ_0 are chosen according to table 5.1. R_0 needs to be set to a really small value to achieve convergence, which increases the computational time extensively.

The residuals, which define the stop criteria of the loops are estimated by Euklidian norms of pressure distribution, film distribution and absolute error of vertical piston force:

$$\epsilon_p = \frac{\left\| p_k^{n,p,q+1} - p_{\mathrm{FE},k}^{n,p,q} \right\|_2}{\left\| p_k^{n,p,q+1} - p_{\mathrm{amb}} \right\|_2} \;, \tag{5.29a}$$

Table 5.1: Calculation parameters

R_0	0.03
Θ_0	0.05

Data: algorithm of fully coupled EHD program
for *every time step* **do**

    $n = n + 1$;

    $\Theta^{(n)} = \Theta^{(n-1)} + \Delta\Theta^{(n)}$;

    guess $y_{\mathrm{P}}^{(n)}$: $y_{\mathrm{P}}^{(n)} = a\,\Theta^{(n)2} + b\,\Theta^{(n)} + c$;

    a, b and c being functions of $e^{(n-3)}, e^{(n-2)}, e^{(n-1)}, \Theta^{(n-3)}, \Theta^{(n-2)}, \Theta^{(n-1)}$;

    $p = 0, q = 0$;

    while $\epsilon_{\mathrm{RF}} > \mathrm{limit}_{\mathrm{RF}}$ **do**

        $n = n, p = p + 1, q = 0$;

        compute eccentricity $y_{\mathrm{P}p,q}^{(n)}$ (Newton-Raphson);

        while *no stabilty of film thickness and pressure distribution* **do**

            $n = n, p = p, q = q + 1$;

            solve Reynolds equation;

            apply updated pressure distribution;

            solve FE calculation;

            compute residuals;

        end

    end

end

Algorithm 1: Basic algorithm that describes interaction between ABAQUS FE-solver and user defined subroutine

$$\epsilon_h = \frac{\left\| h_k^{n,p,q+1} - h_{\mathrm{FE},k}^{n,p,q} \right\|_2}{\left\| h_k^{n,p,q+1} \right\|_2} \;, \tag{5.29b}$$

$$\epsilon_{R_{\mathrm{F}}} = \mathrm{abs}(R_{\mathrm{F}} + F_{\mathrm{P},y}) \;, \tag{5.29c}$$

where R_{F} denotes the reaction force in point $\mathrm{RP}_{\mathrm{ring}}$ and $F_{\mathrm{P},y}$ is the target value of the vertical piston force and p_{amb} denotes the ambient pressure.

Due to the elastic ring deformations, the time derivation of the gap $\partial h(z, y)/\partial\Theta$ is not linear any more and is estimated by the second order accurate finite approximation

$$\left(\frac{\mathrm{d}h}{\mathrm{d}\Theta}\right)^{(n)} = \frac{\Delta\Theta_n}{\Delta\Theta^{(n-1)}(\Delta\Theta^{(n-1)} + \Delta\Theta^{(n)})}h^{(n-2)} - \frac{\Delta\Theta^{(n-1)} + \Delta\Theta^{(n)}}{\Delta\Theta^{(n)}\Delta\Theta^{(n-1)}}h^{(n-1)}$$
$$+ \frac{\Delta\Theta^{(n-1)} + 2\Delta\Theta^{(n)}}{(\Delta\Theta^{(n)} + \Delta\Theta^{(n-1)})\Delta\Theta^{(n)}}h^{(n)} + \mathscr{O}(\Theta^2) \,. \tag{5.30}$$

The second derivative of $\tilde{y}_\mathrm{P}$ is also estimated by a second order accurate finite approximation:

$$\left(\frac{\partial^2 y_\mathrm{P}}{\partial\Theta^2}\right)^{(n)} = \frac{2\left(3\Delta\Theta^{(n)} + 2\Delta\Theta^{(n-1)} + \Delta\Theta^{(n-2)}\right)}{\Delta\Theta^{(n)}\left(\Delta\Theta^{(n)} + \Delta\Theta^{(n-1)}\right)\Delta\Theta_\mathrm{sum}}y_\mathrm{P}^{(n)}$$
$$- \frac{2\left(2\Delta\Theta^{(n)} + 2\Delta\Theta^{(n-1)} + \Delta\Theta^{(n-2)}\right)}{\Delta\Theta^{(n)}\Delta\Theta^{(n-1)}\left(\Delta\Theta^{(n-1)} + \Delta\Theta^{(n-2)}\right)}y_\mathrm{P}^{(n-1)}$$
$$+ \frac{2\left(\Delta\Theta_\mathrm{sum} + \Delta\Theta^{(n)}\right)}{\left(\Delta\Theta^{(n)} + \Delta\Theta^{(n-1)}\right)\Delta\Theta^{(n-1)}\Delta\Theta^{(n-2)}}y_\mathrm{P}^{(n-2)}$$
$$- \frac{2\left(2\Delta\Theta^{(n)} + \Delta\Theta^{(n-1)}\right)}{\Delta\Theta_\mathrm{sum}\left(\Delta\Theta^{(n-1)} + \Delta\Theta^{(n-2)}\right)\Delta\Theta^{(n-2)}}y_\mathrm{P}^{(n-3)} + \mathscr{O}(\Theta^2) \,, \tag{5.31}$$

with

$$\Delta\Theta^{(n)} = \Theta^{(n)} - \Theta^{(n-1)} \,,$$
$$\Delta\Theta_\mathrm{sum} = \Delta\Theta^{(n)} + \Delta\Theta^{(n-1)} + \Delta\Theta^{(n-2)} \,. \tag{5.32}$$

5.3.1 User defined subroutines

User defined subroutines that communicate with the ABAQUS solver are written in Fortran 95. The following user subroutines are used, extensive descriptions of them are found in [50]:

- UEXTERNALDB: "is called once each at the beginning of the analysis, at the beginning of each increment, at the end of each increment, and at the end of the analysis [50];" it is used for initialization, and for the main calculations: All routines shown in algorithm 1 are done therein (including the solution of the Reynolds equation,...). Above all, information for post-processing is exported to txt-files.

- URDFIL: "can be used to access the results file during an analysis; is called at the end of any increment in which new information is written to the results file [50];" this routine is used to read the geometry definition at the start of the simulation to create a coincidence matrix: Nodes being at the ring's outer surface are identified and sorted. This is necessary for getting the gap between cylinder wall and ring surface leading to the calculation of the oil pressure, and

for prescribing the pressure. It is also used to access the results file after each increment: the elastic deformations are read, as well as the reaction force in node RP_{ring}.

- DLOAD: "can be used to define the variation of the distributed load magnitude as a function of position, time, element number, load integration point number, etc.; will be called at each load integration point for each element-based or surface-based non-uniform distributed load definition during stress analysis [50];" DLOAD is used to apply the pressure on the outer ring's surface.

- DISP: can be used to define the magnitudes of prescribed boundary conditions or connector motions [50];" finally, this routine is used to prescribe the tilt δ and the eccentricity $\tilde{y}_{\text{P}}$ of the piston (DOF 2 and 6 for node RP_{ring}).

5.4 Implementation of global lubrication model (MATLAB)

The commercial program MATLAB is used to solve the equations of motions of the dynamic compressor model (4.11)–(4.13). The compressor model shows a very stiff behaviour, especially when the clearance of either piston or crosshead decreases and contact occurs. Therefore, the ODE solver "ode15i" [49] is chosen, which is a variable-step solver that uses orders from 1 to 5. It is designed to integrate a system of fully implicit differential equations of the form $f(t, y, y') = 0$. In addition, it calls after every converged time step optional event functions of (t, y, y') to find if they are zero. Such an event function is used to do the front tracking of the oil regions and to save data for post processing.

The algorithm of the global lubrication program is sketched below (see Algorithm 2): Initiating, the 2-equations gas pressure model is called to calculate the crank-angle dependent pressure values for all chambers. In the next step, the ODE-solver is started. Within each increment, the ode-solver calls "odefcn" to evaluate the residuals.

This function first computes all time and solution dependent values: U, β, $\tilde{F}_{\text{gas}}$, $\ddot{x}_C$, β, $\dot{\beta}$, $\ddot{\beta}$, $h(x, z)$, $\partial h / \partial \Theta(x, z)$. The well-known leading order relationship for bearings, $h(\Theta) = 1 + \epsilon \cos \phi$, where h denotes the gap and ϵ is the dimensionless eccentricity ($\tilde{y}_{\text{P}}/\tilde{c}$), is adopted for our purpose to account for the piston tilt δ:

$$h(x, z) = h_0(x, z) + (\epsilon + \xi \, x) \cos \phi - 0.5 \xi^2 \lambda \cos^2 \phi \tag{5.33}$$

with

$$\epsilon = \frac{\tilde{y}_{\text{P}}}{\tilde{c}_0} \ , \xi = \frac{\tilde{B}\delta}{\tilde{c}_0} \ , \lambda = \frac{\tilde{d_{\text{cyl}}}\tilde{c}_0}{2\tilde{B}^2} \ . \tag{5.34}$$

In (5.33), $h_0(x, z)$ are constant values, describing the initial dimensionless gap between ring and cylinder wall, with zero piston tilt and zero eccentricity. In a next step, the crosshead model is called, followed by calls of the rider ring model for each

rider ring. Each rider ring can see a different pressure level (dependent on piston layout) and different oil front positions. The general forces and moments $\tilde{F}_{\mathrm{C},y}$, $\tilde{M}_{\mathrm{C}}$ and $\tilde{F}_{\mathrm{P},x}$, $\tilde{F}_{\mathrm{P},y}$, $\tilde{M}_{\mathrm{P}}$ are calculated according to (4.26) and (4.25). Finally, the residuals of the equations of motion (6 ODEs) are calculated.

In case the time step is converged, the ODE-solver calls the event function. This function is used to

- call the piston ring model for each piston ring,

- do the oil front tracking and oil balancing routines (see Sec. 5.1.2),
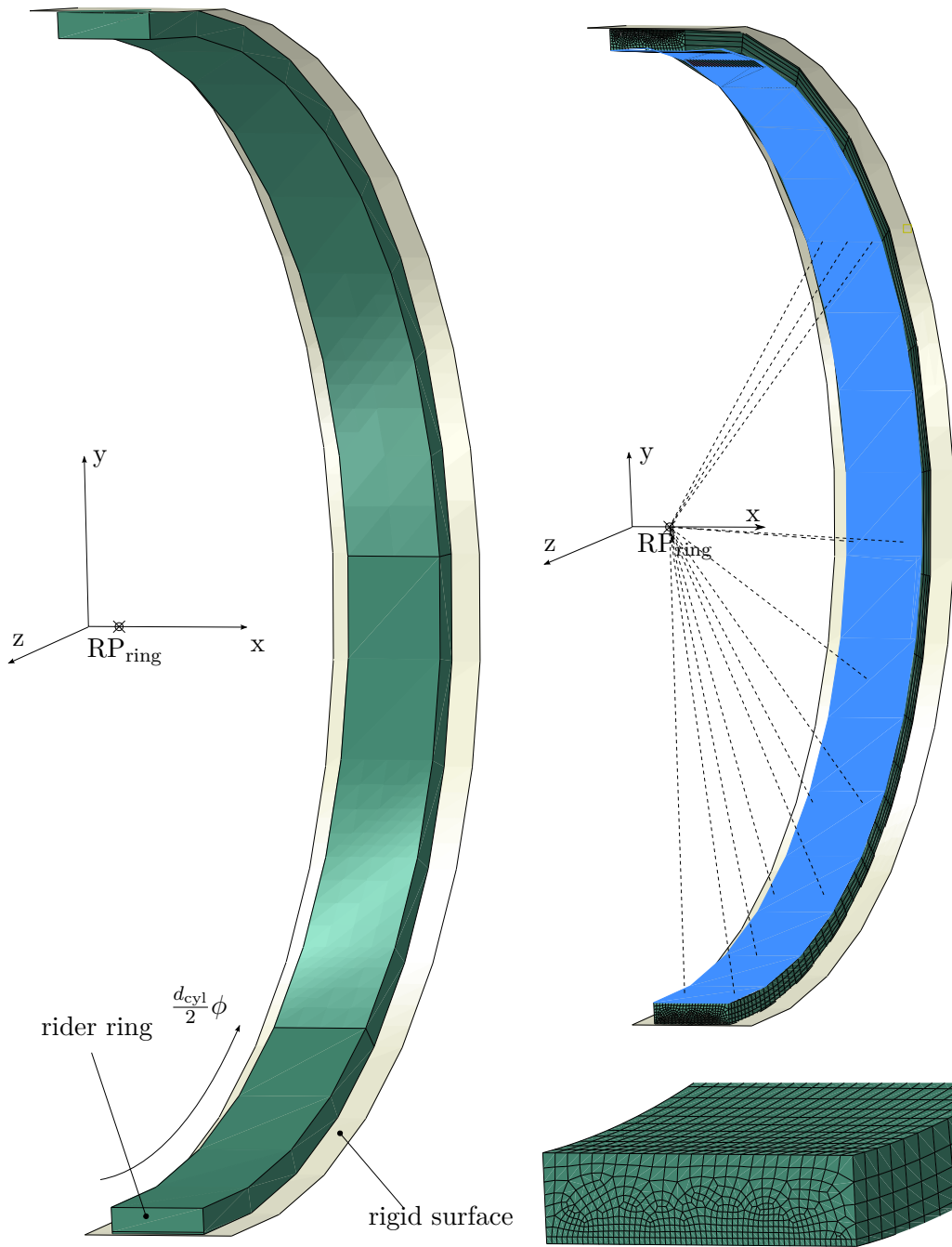
- save relevant data for postprocessing.

Figure 5.9: FE-Model: The left image shows the rider ring in the global coordinate system (x,y,z). The radial degrees of freedom of the "inner" nodes (nodes on blue-labelled surface) are constrained in a local coordinate system (with origin RP_{ring}), which can move in global y-direction and can rotate around the global z-axis.

Data: algorithm of global lubrication model
call 2-equations gas pressure model
call ode15i-solver
for *every time step* **do**
    for *every increment until convergence* **do**
        "ode15i" calls "odefcn", which calculats residuals
        time-dependent values are computed: $U, \beta, \ddot{x}_C$, etc.
        time-dependent gas pressure is read, $\tilde{F}_{\mathrm{gas}}$ is computed
        time- and solution-dependent values are computed:
         $\beta, \dot{\beta}, \ddot{\beta}, h(x, z), \partial h/\partial\Theta(x, z)$
        call rider ring model:
        for *each rider ring i* **do**
            compute $p(x, z)$
            compute $\tilde{F}_{\mathrm{P,x,sub},i}$
            compute $\tilde{F}_{\mathrm{P,y,sub},i}$
            compute $l_{\mathrm{rr,x},i}$
            compute $l_{\mathrm{rr,y},i}$
        end
        call crosshead model:
        begin
            compute $\tilde{F}_{\mathrm{C},x}, \tilde{F}_{\mathrm{C},y}, \tilde{M}_{\mathrm{C}}$
        end
    end
    call event function:
    begin
        call piston ring model
        compute oil volume flows for fully flooded and starved ring regions
        compute oil volumes of transition regions
        compute oil volumes on cylinder wall next to transition regions
        save data for post processing
    end
end
Algorithm 2: Basic algorithm that describes the iterative solver of the equation of motions.

6 Results

As mentioned in chapter 5, the developed programs are based on solving equations for non-dimensional variables. Therefore, all dimensional quantities will be marked by a tilde in this chapter. This chapter starts by showing the results of the CFD calculations (Sec. 6.1), which justify the neglect of the gas-driven oil flow in the global cylinder lubrication model. Then, the impact of elastohydrodynamic effects is shown (Sec. 6.2) using data of an in-house test rig of ©HOERBIGER. Finally, results of the global cylinder lubrication model are shown, using the case of a "real" manufactured compressor (Sec. 6.3).

6.1 CFD: results of compression cycle (FLUENT)

The focus of this simulation lies on calculating the wall shear stress at the compressor chamber's wall, which is necessary to estimate the gas driven oil flow. Further results are shown to gain confidence in the CFD model and its results, but are not needed for the global problem. Table 6.1 summarizes the relevant compressor data and operating conditions.

The mass flow through the suction– and the discharge valve as well as averaged pressures are compared to results of the 2–equations gas model (see Fig. 6.1). Basically, both models give very similar results, the following differences are identifiable: The peak at the beginning of the discharge-mass flow of the CFD calculation, which is most likely due to the different valve characteristic: Remember, $\tilde{\phi}_{\mathrm{valve}}$ is defined to increase from 0 to a maximum value after $1\,\mathrm{ms}$, following a quadratic characteristic in the CFD calculation while the 0D-model opens instantaneously. The closing event is modelled to be instantaneous in both models, producing in both cases oscillations.

The slightly smaller mass outflow per time in the CFD calculation, resulting in a longer opening time of the discharge valve is a result of the reduced cross section of the compression chamber: It acts like a bottleneck for the gas flow from the suction-valve pocket to the discharge valve, leading to two uncoupled clearance volumes. This is clearly seen in the first image of Fig. 6.2. Figures 6.2–6.5 show the pressure– and velocity distributions in the symmetry plane of the compression chamber of equally spaced time points (25° interval) over one revolution, starting from 8°–357°. The suction-valve pocket shows an almost uniform pressure, whose level is significantly higher than the pressure level of the discharge-valve pocket. This pressure overshoot in the suction-valve pocket is also shown in the lower graph of Fig. 6.1, where the curves show the averaged pressures in the discharge-valve pocket and in the suction-valve pocket, and the uniform pressure of the 2–equations gas pressure model. The pressure overshoot seems unrealistically high, although

Table 6.1: CFD: parameters of compressor C2AR

$\tilde{d}_{\text{cyl}}$	$203\,\text{mm}$
stroke	$89\,\text{mm}$
rpm	$750\,/\,\text{min}$
$\tilde{U}_{\text{m}}$	$2.2\,\text{m}\,\text{s}^{-1}$
$\tilde{p}_{\text{s}}$	$2.8\,\text{bar}$
$\tilde{\rho}_s$	$4.6\,\text{kg}\,\text{m}^{-3}$
$\tilde{T}_s$	$25°$
$\tilde{p}_{\text{d}}$	$8.2\,\text{bar}$
$\tilde{\rho}_d$	$8.6\,\text{kg}\,\text{m}^{-3}$
$\tilde{T}_d$	$131.3°$
gas type	air

pressure-measurements of the compressor are not available, which might confirm this assumption. In the presumably case that this pressure-overshoot is lower in reality, the difference can be explained by an imprecise geometry model: Since no original CAD-data was available, the geometry was manually measured — due to the complicated geometry some measurements of the valve pockets needed to be estimated. A bigger overlap between valve pocket and compression chamber (in azimuthal direction) would increase the bottleneck and would thus reduce the pressure level in the suction-valve pocket. This is also indicated by the compression– and expansion curves of the CFD model, which are steeper than the pressure curve of the 2–equations gas pressure model, indicating a lower dead space of the CFD model. Indeed, the dead space of the CFD model is 7.4 % vs. 10 %, gotten from the compressor manufacturer and taken for the 0D-model.

The images in Fig. 6.3 show an almost uniform pressure distribution in the cylinder region during the compression cycle, confirming the quasi-static approach of the 2–equations gas model.

The surprisingly good fit of the mass flows of the two simulation models is explained by the very similar pressure curves: Although the 0D-model is based on a uniform pressure distribution and does therefore not show the behaviour of the two uncoupled clearance volumes, its pressure results resemble the suction-valve pressure during expansion, and the discharge-valve pressure during compression. Valve closing and opening times (results taken from CFD calculation) are summarized in table 6.2.

Table 6.2: CFD results: opening and closing times of valves

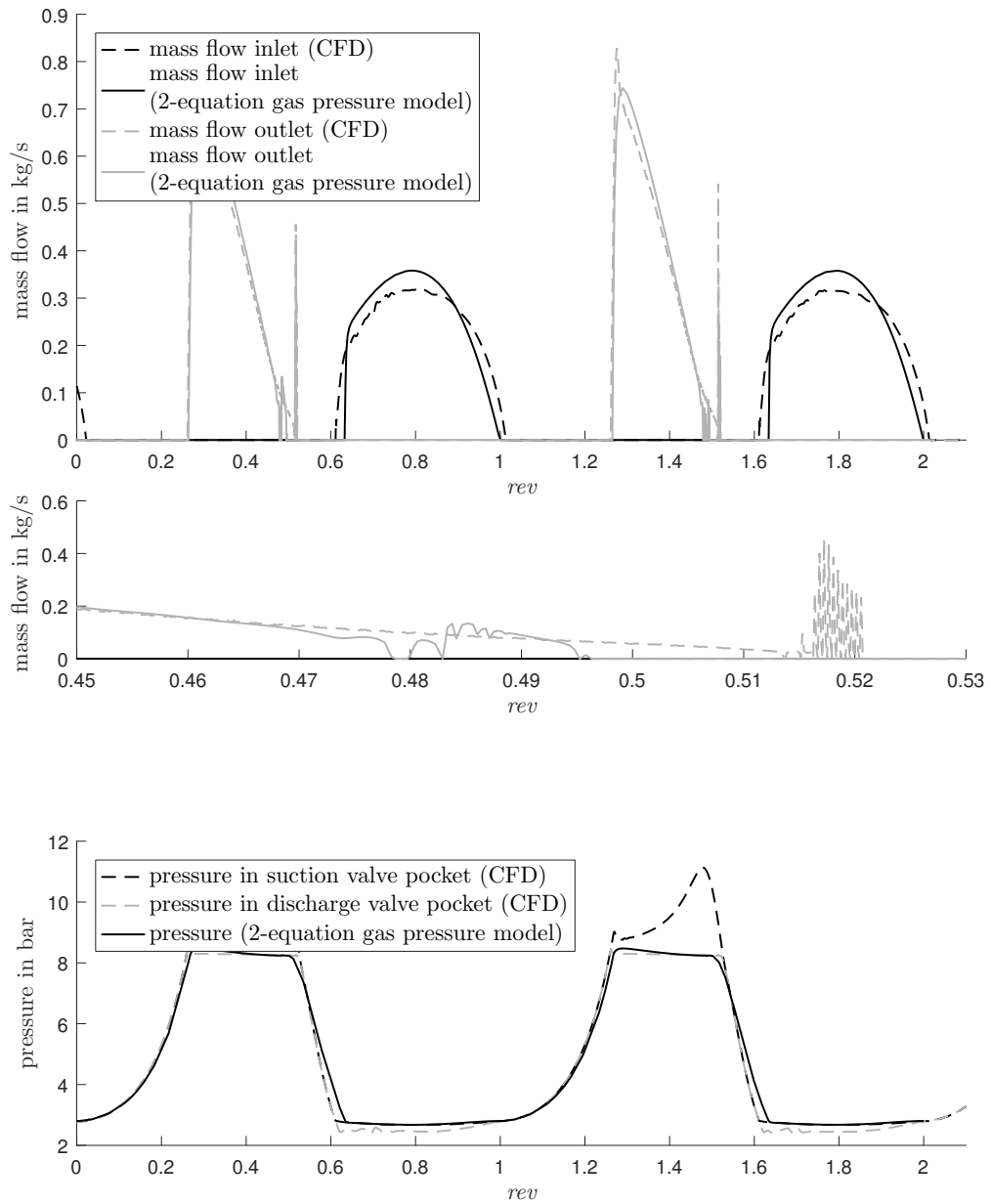|	crank angle	revolution
opening of suction valve	220°	0.61
closing of suction valve	5°	0.01
opening of discharge valve	93°	0.26
closing of discharge valve	187°	0.52

Figure 6.1: CFD results (dashed line) vs. 2–equations gas model (solid line) over 2 revolutions; upper Fig.: mass flow through suction– and discharge valve; middle Fig.: close up of closing event of discharge valve; lower Fig.: averaged pressures in suction-valve pocket and in discharge-valve pocket (CFD model) as well as uniform pressure (2–equations gas model);
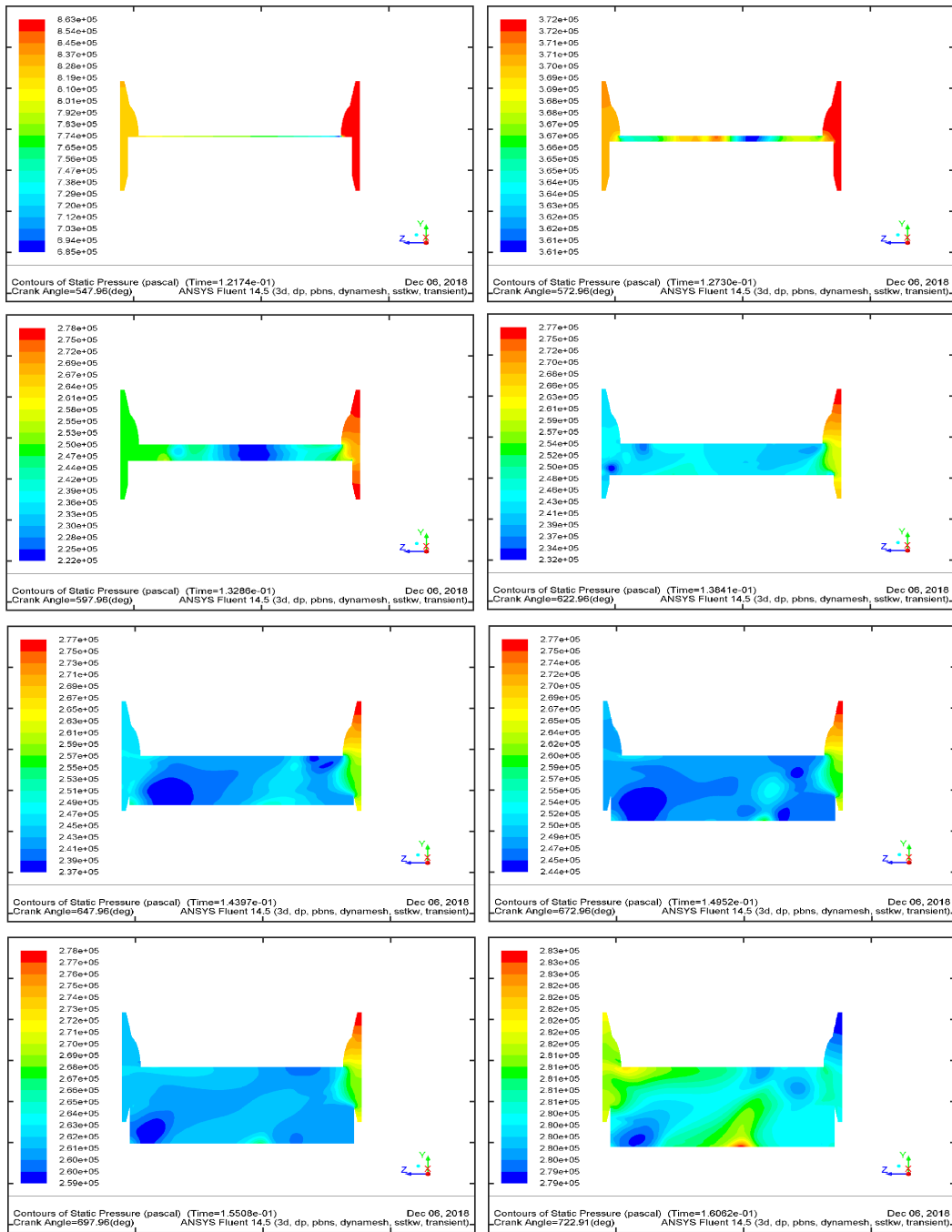
Figure 6.2: Pressure plots for symmetry plane for one revolution, starting from 8°–183°, equally spaced in time (25° interval), from top left to down right. Surface area, which is overlapped by the piston is shown in white; legend shows values in Pa;
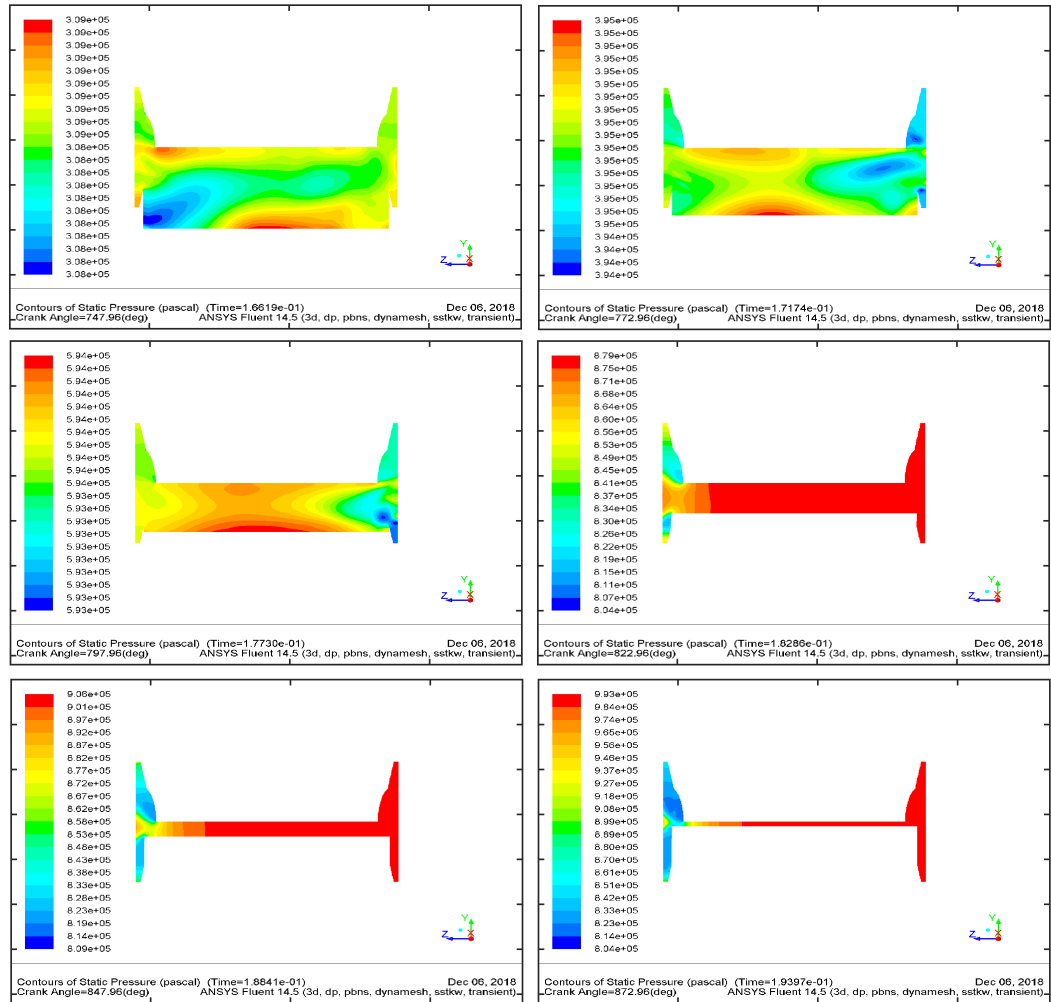
Figure 6.3: Pressure plots for symmetry plane for one revolution, starting from 208°–333°, equally spaced in time (25° interval), from top left to down right. Surface area, which is overlapped by the piston is shown in white; legend shows values in Pa;

Figure 6.4: Velocity plots for symmetry plane for one revolution, starting from 8°–183°, equally spaced in time (25° interval), from top left to down right. Surface area, which is overlapped by the piston is shown in white; legends show values in m/s;
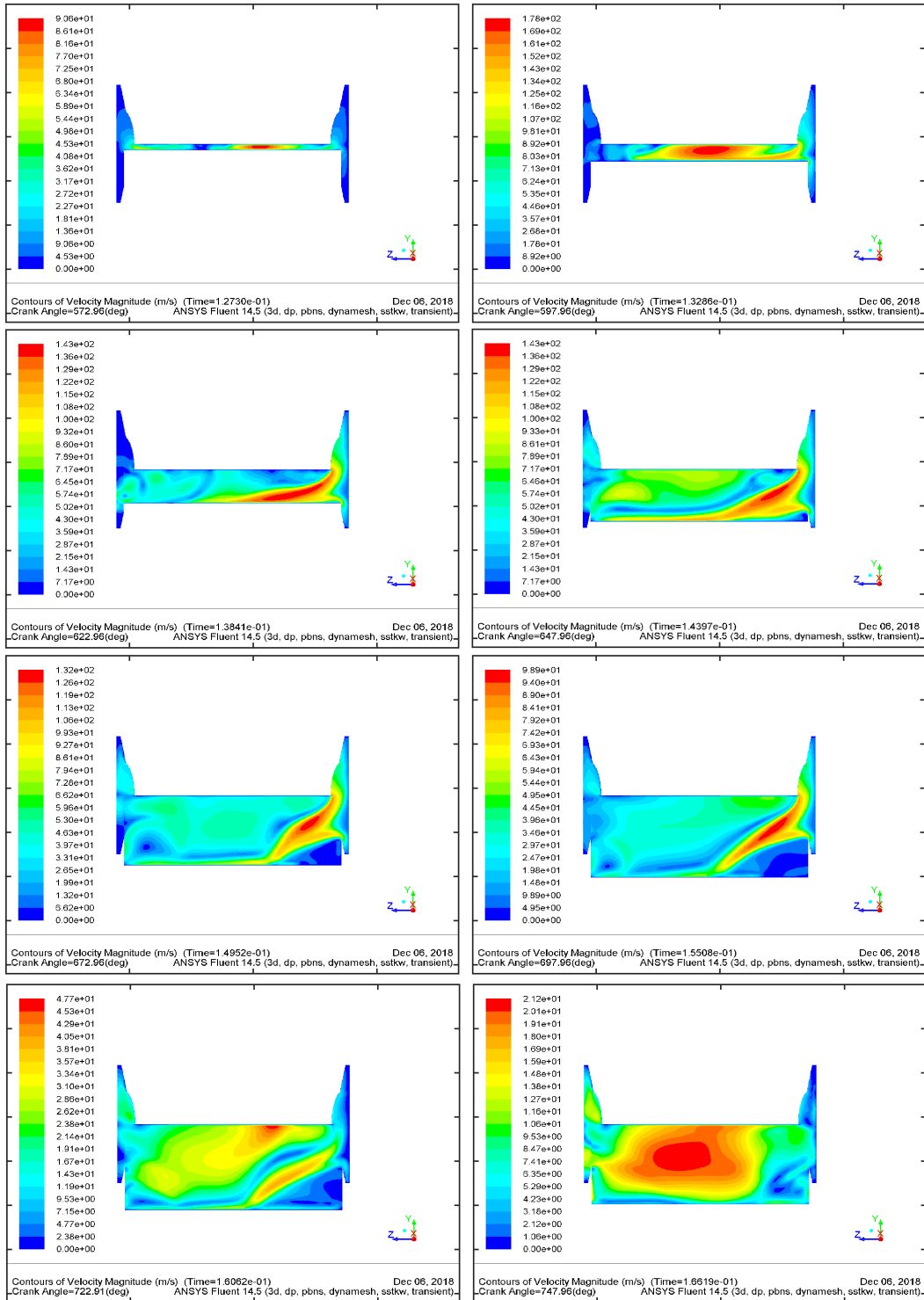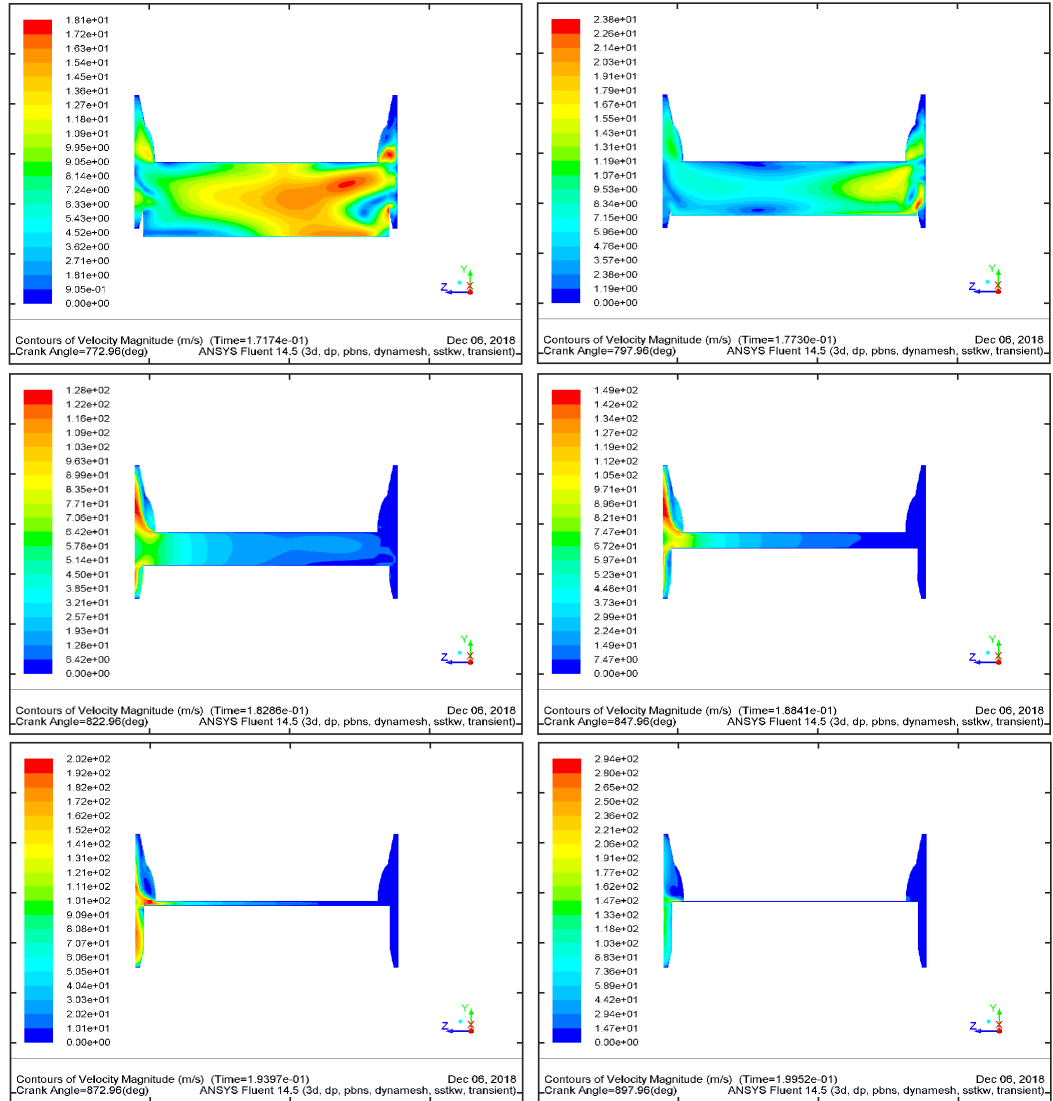
Figure 6.5: Velocity plots for symmetry plane for one revolution, starting from 208°–333°, equally spaced in time (25° interval), from top left to down right. Surface area, which is overlapped by the piston is shown in white; legend show values in m/s;

6.1.1 Oil film slip velocity due to wall shear stress

Equation 3.36 shows the linear correlation between $\tilde{u}(\tilde{x}, \tilde{y})$ and $\tilde{\tau}_g$. Hence, the slip velocity of the oil film is linear proportional to the oil-film thickness and the wall shear stress and reads

$$\tilde{u}_s = \frac{\tilde{\tau}_g}{\tilde{\mu}_f} \tilde{h}_{film} \; . \tag{6.1}$$

The slip velocity $\tilde{u}_s$ is exemplary calculated using (6.1) for $\tilde{h}_{film} = 0.1\,\text{mm}$, and taking a typical value for the dynamic viscosity $\tilde{\mu}_f = 0.1\,\text{Pa}\,\text{s}$. Based on these chosen parameters, $\tilde{u}_s = 1\,\text{m}\,\text{s}^{-1}$ corresponds to $\tilde{\tau}_g = 1\,\text{kPa}$. The wall shear stress $\tilde{\tau}_g$ and the slip velocity $\tilde{u}_s$ are shown in Fig. 6.6–6.8 for equally spaced time points (25° interval) of one revolution (starting from 8°–333°), which are the same time points as in Fig. 6.2–6.5: $\tilde{u}_s$, respectively $\tilde{\tau}_g$, is plotted over the developed cylinder surface. The discharge valve is at the left side near $\phi = 0$, the plots show $\tilde{u}_s$ and $\tilde{\tau}_g$ for the wall of the compression chamber in front of the piston, which length changes from an initial clearance of $1\,\text{mm}$ to l_{st}, dependent on the crank angle. Surface area, which is overlapped by the piston is shown in white.

The highly dynamic transition zones between compression chamber and valve pockets can be identified by the peaks near $\phi = (0, \pi)$. These peaks exist for the whole revolution. For a better visibility of the values apart from the transition regions, they are limited at $\tilde{\tau}_g = 0.1\,\text{kPa}$. Their unlimited values are shown in Fig. 6.6, which is basically the same figure, not limited this time and results viewed from the top. $\tilde{\tau}_g$ reaches values up to $6\,\text{kPa}$, dependent on crank angle and position and on the opening cross-section of suction– and discharge valve, leading to a significant oil-mass flow. Above all, a significant oil flow towards discharge valve is seen at the final moments of the discharge event. However, $\tilde{\tau}_g$ in the other regions is most of the time cycle below $0.3\,\text{kPa}$, leading to $\tilde{u}_s = 0.3\,\text{m}\,\text{s}^{-1}$, or even significantly lower — compare to $\tilde{U}_m = 2.2\,\text{m}\,\text{s}^{-1}$.

These results confirm, that $\tilde{u}_s \ll \tilde{u}_P$ (3.25) and justify the simplification of neglecting oil flow due to the gas flow in the basic simulation, at least for a predominant part of the cylinder wall and film heights. However, they also suggest a significant oil transport at the valve region and for all regions for higher film heights, giving a conclusive explanation for the removal of oil, which is left at the sides of the piston at the dead centre positions.
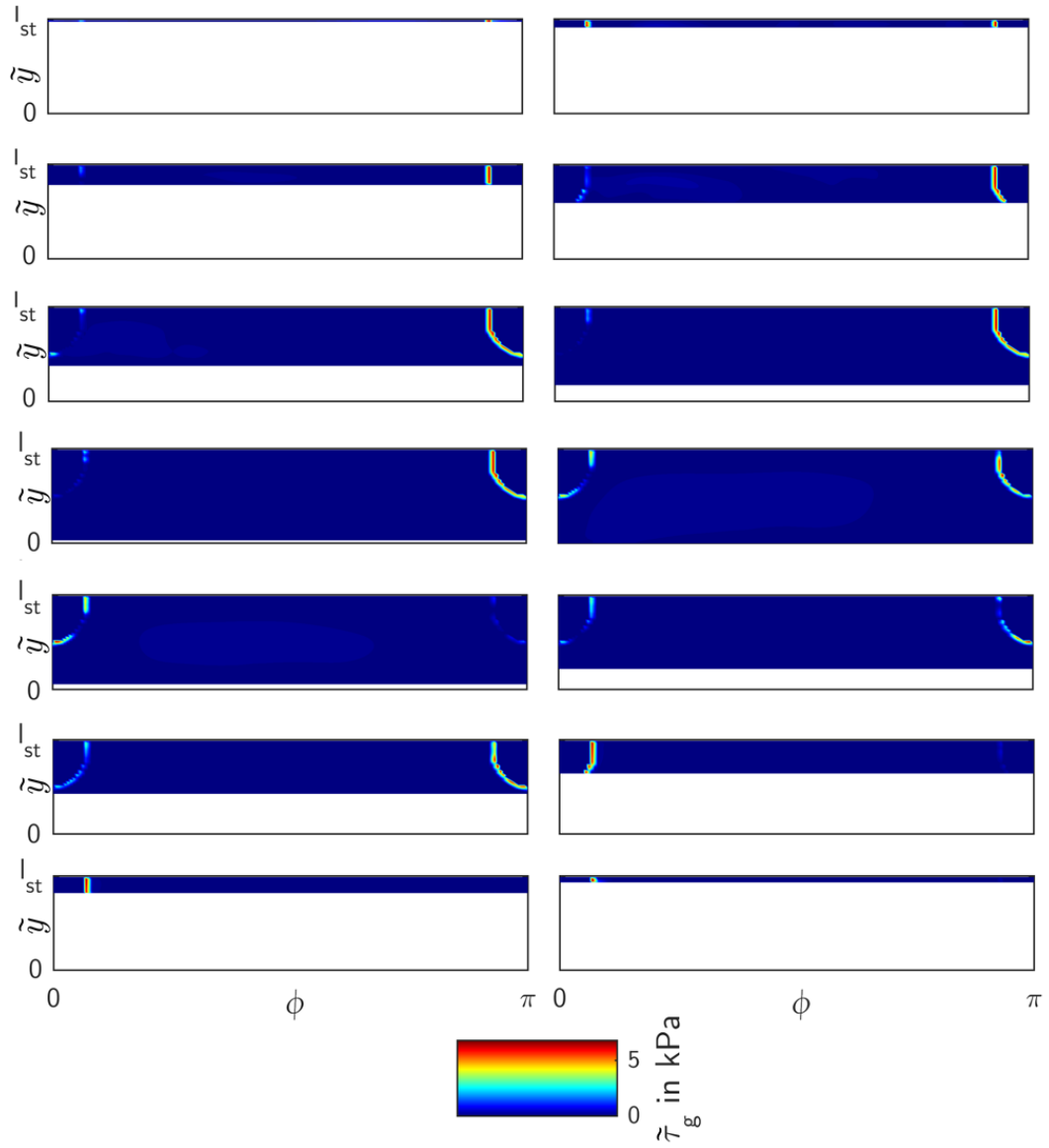
Figure 6.6: $\tilde{\tau}_\mathrm{g}$– plots for one revolution, starting from 8°–333°, equally spaced in time (25° interval), from top left to down right: It is plotted over the developed cylinder surface, where the discharge valve is positioned at the side of $\phi = 0$. Surface area, which is overlapped by the piston is shown in white.

Figure 6.7: Slip velocity plots for one revolution, starting from 8°–158°, equally spaced in time (25° interval), from top left to down right: The slip velocity is plotted over the developed cylinder surface, where the discharge valve is positioned at the side of $\phi = 0$. The slip velocity $\tilde{u}_\mathrm{s}$ is calculated for $\tilde{\mu}_\mathrm{f} = 0.1\,\mathrm{Pa\,s}$, $\tilde{h}_\mathrm{film} = 0.1\,\mathrm{mm}$. Surface area, which is overlapped by the piston is shown in white.
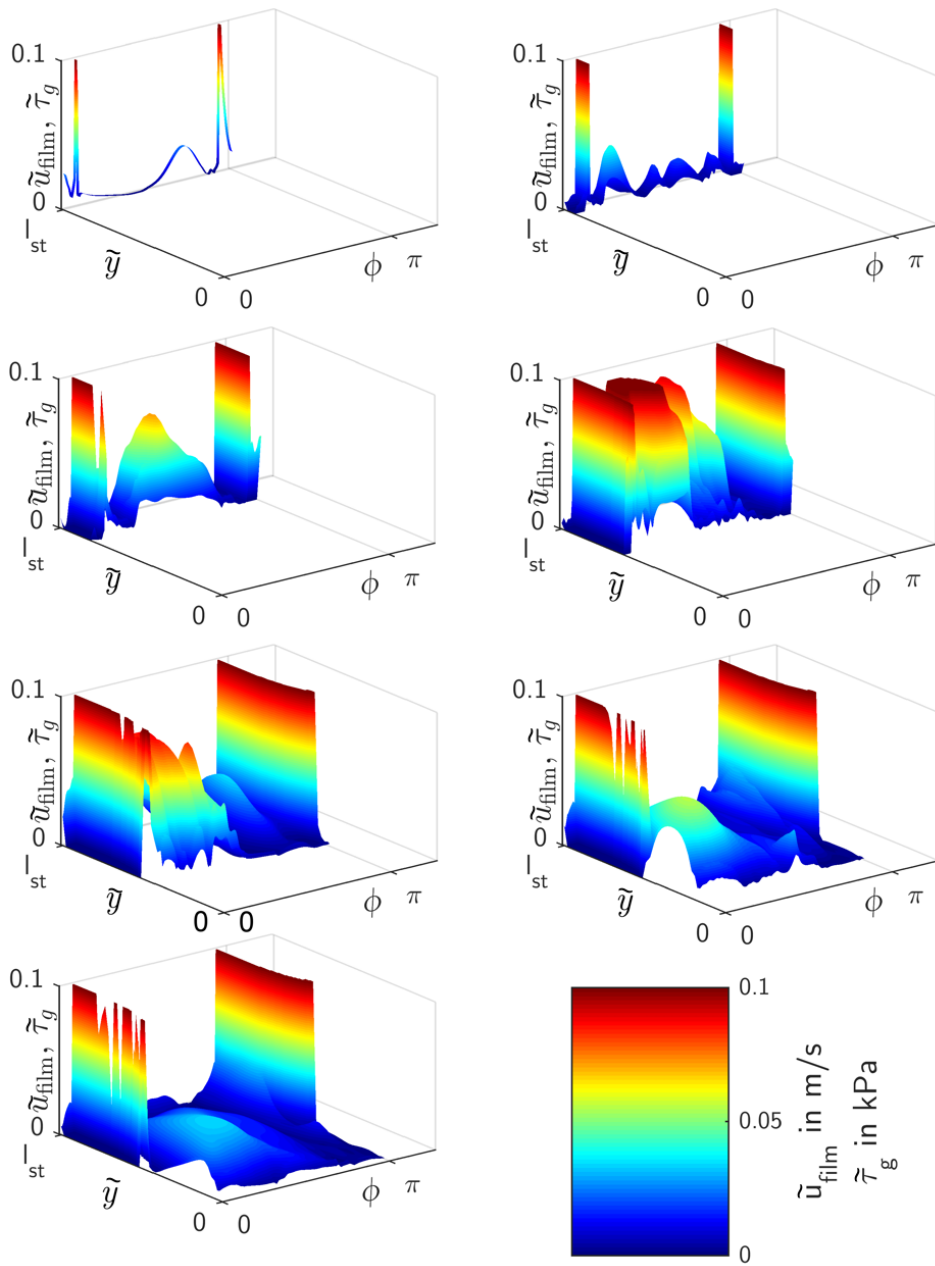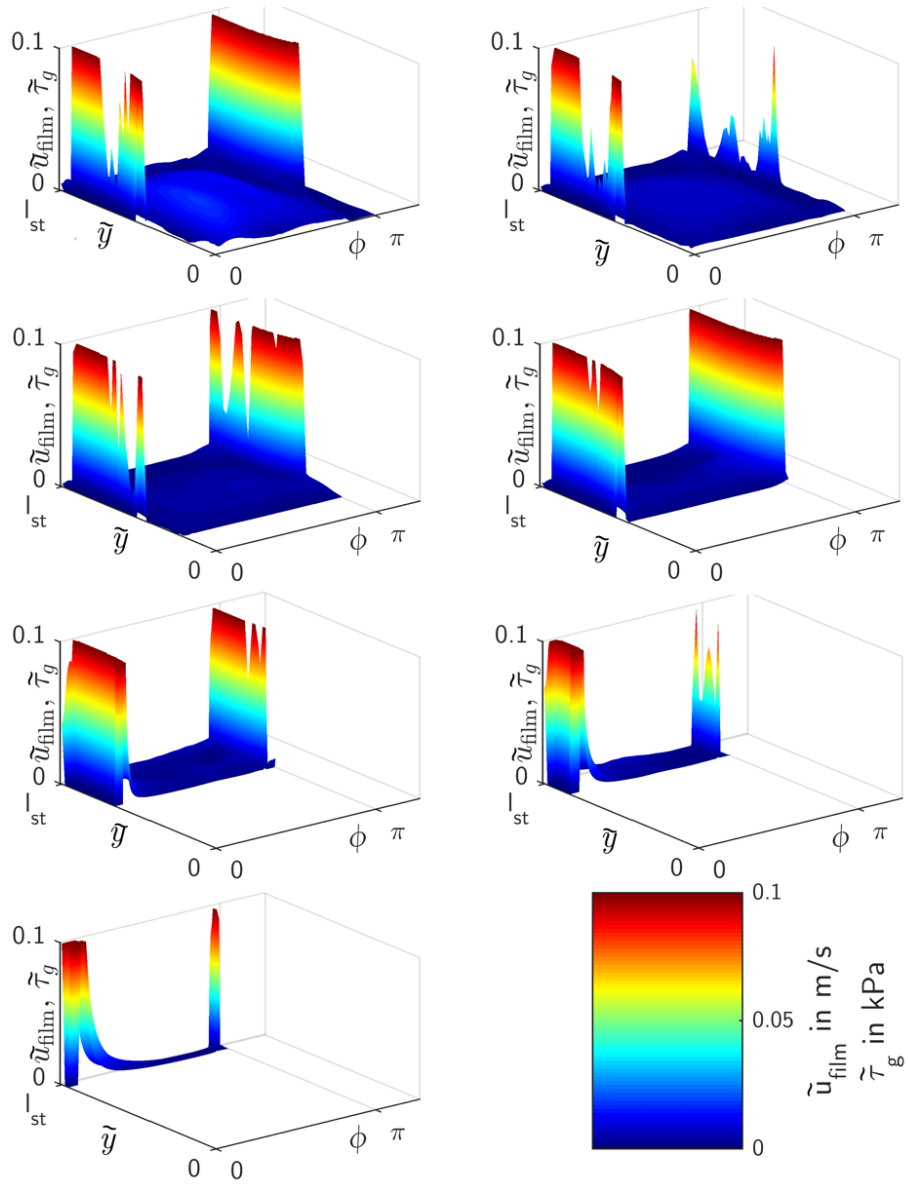
Figure 6.8: Slip velocity plots for one revolution, starting from 183°–333°, equally spaced in time (25° interval), from top left to down right: The slip velocity is plotted over the developed cylinder surface, where the discharge valve is positioned at the side of $\phi = 0$. The slip velocity $\tilde{u}_s$ is calculated for $\tilde{\mu}_f = 0.1\,\mathrm{Pa\,s}$, $\tilde{h}_{\mathrm{film}} = 0.1\,\mathrm{mm}$. Surface area, which is overlapped by the piston is shown in white.

Table 6.3: EHD: parameters of test rig

$\tilde{d}_{\mathrm{cyl}}$	$150\,\mathrm{mm}$
stroke	$100\,\mathrm{mm}$
rpm	$750\,/\min$
$\tilde{m}$	$14.19\,\mathrm{kg}$
$\tilde{p}_{\mathrm{s}}$	$2.8\,\mathrm{bar}$
$\tilde{p}_{\mathrm{d}}$	$8.2\,\mathrm{bar}$
gas type	air
$\tilde{c}_0$	$0.4\,\mathrm{mm}$
$\tilde{w}_{\mathrm{r}}$	$12\,\mathrm{mm}$
number of nodes in axial direction	103
number of nodes in azimuthal direction	76

6.2 Elastohydrodynamic effects (coupled ABAQUS/Standard)

For the research of elastohydrodynamic effects on oil consumption, data of an in-house test rig of ©HOERBIGER is used, see table 6.3 for details. The rig's piston is guided by one rider ring, which is assumed to be axial-symmetric, with a rectangular cross-section. The ring has a chamfer at both sides with the dimensions of $0.5 \times 0.5\,\mathrm{mm}^2$.

Elastohydrodynamic effects were researched by evaluating the net-oil flow. As mentioned in Sec. 5.3, we assume fully flooded gaps (including the chamfers), the interplay between rider– and piston rings is neglected in order to concentrate purely on elastohydrodynamic effects. The numerical calculation is highly time consuming: The simulation of one revolution takes approx. 10 days per revolution on 4 CPUs (3.6 GHz).

6.2.1 Full EHL formulation vs. rigid formulation

Figure 6.9 shows a comparison of EHL results and rigid results: the eccentricity and the net-oil flow for three revolutions in a steady state condition. The squared markers label the points of revolutions, which are investigated in more detail later in this section (see Fig. 6.11). Both calculations are done using $\widetilde{\mathrm{gap}}_{\mathrm{min}} = 5\,\mu\mathrm{m}$. Since we assumed an "ideal crosshead", a negative eccentricity always equals a positive tilt — see (5.25). Therefore, the piston in this simulation is always tilted positively, resulting in a convergent gap for negative (cylinder) velocities.

The piston reaches its maximum $\epsilon = -0.923$ at $rev = 0.455$ for the EHL case, and just slightly later, $\epsilon = -0.922$ at $rev = 0.46$ for the rigid-case, at a point of time where the velocity decreased below the level where the (elasto) hydrodynamic pressure does not push the piston upwards anymore. At $rev \approx 0.85$, the piston finally reaches the mixed lubrication regime, which it leaves immediately with $rev > 1$: A very low

Table 6.4: Impact of elasticity on net-oil flow

	net oil flow in l/h	percent
rigid formulation	0.804	100 %
EHL formulation	0.811	100.9 %

relative velocity is enough at these small gap heights to generate a sufficient high (elasto) hydrodynamic pressure. Obviously, the squeeze-effect plays an important role, almost preventing the piston to touch the cylinder wall in this case. It also softens the piston's motion upwards, resulting in a vertical movement of approx. 0.02 mm.

Elastohydrodynamic effects seem to play a minor role, noting a difference of just 0.1 % by looking at the maximal difference of eccentricities. This conclusion is supported by taking a look at the net-oil flow: It is calculated for both cases using the net-oil flow of three revolutions, and extrapolating these values to get a flow rate in l/h. A comparison shows a difference of less than 1 %—results are shown in table 6.4.
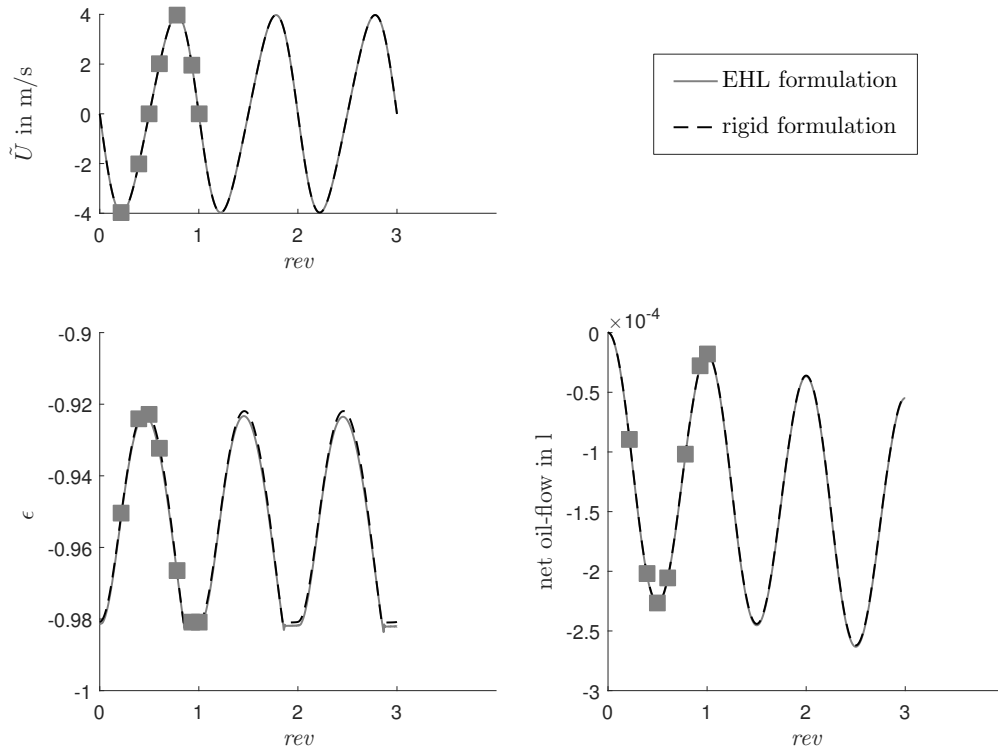

Figure 6.9: Velocity (upper image), eccentricity (left image) and net oil-flow (right image): EHL vs. rigid formulation; The squared markers label the points of revolutions, which are investigated in more detail, shown in Fig. 6.10.
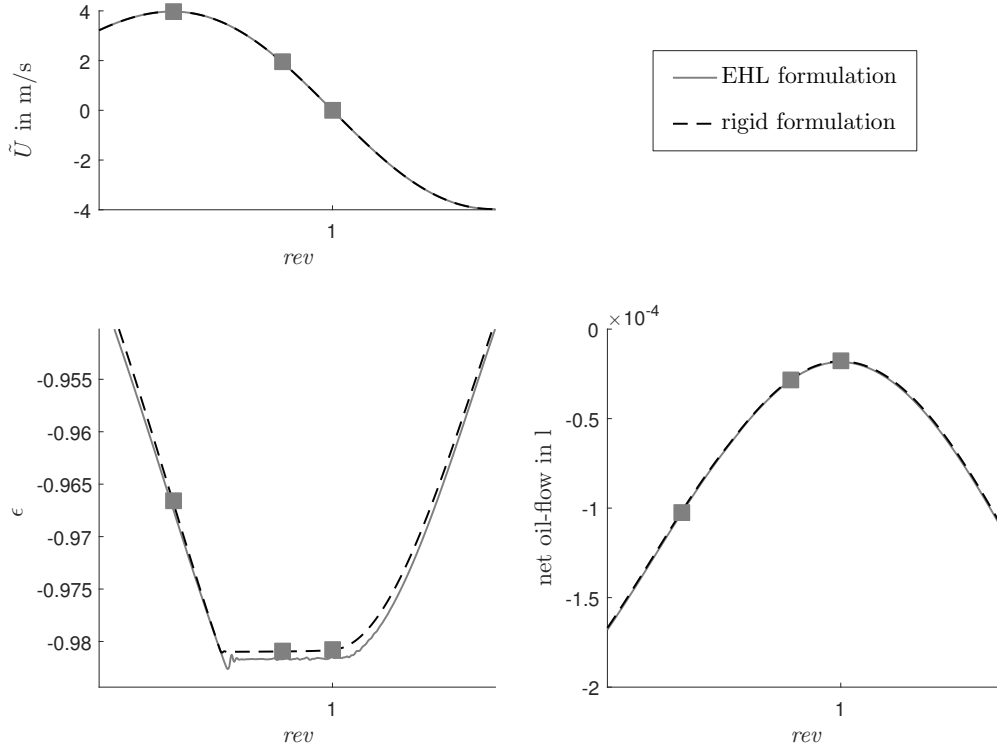
Figure 6.10: Velocity (upper image), eccentricity (left image) and net oil-flow (right image): detail of Fig. 6.9; .

The ring deformation is apparent by comparing the eccentricity in the mixed-lubrication regime: Both cases have the same minimal gap, but the minimal eccentricities differ by $\approx 1\,\mu m$, which corresponds to the estimation of ring-deformation in (4.29).

Effects of ring deformation are shown in more detail in Fig. 6.11: Pressure profiles and their corresponding gap profiles in the symmetry plane at $\phi = 0$ are shown for seven different time positions, marked in Fig. 6.9. Note, just the pressure and gap distributions underneath the ring without showing the area underneath the chamfers are plotted. The interpretation is tricky due to the superposition of squeeze– and wedge effects. Clearly elastohydrodynamic effects get less important with increasing gaps. Above gap heights of approx. $0.02\,mm$, the pressure distributions look very similar for the rigid and EHL results. The results at times, when the rings are in mixed lubrication, do not show any differences concerning the pressure distributions: Due to the divergent gaps, the oil is cavitating in both cases. Differences in the gap distribution are solely due to elastic deformations due to the mixed contact formulation (i.e. the spring forces). The biggest difference is seen at $\tilde{U} = 3.97\,\mathrm{m\,s^{-1}}$: The pressure profile is significantly different, resulting in a lower mean pressure due to elastic ring deformations. This pressure decrease results in a steeper decrease of eccentricity shown in Fig. 6.10.

In conclusion, the ring passes the elastohydrodynamic regime quite fast and is therefore just slightly affected by elastohydrodynamic effects. The oil flow is dominated by a Couette flow, which furthermore explains the small differences seen in the net-oil flow, keeping in mind the minimal differences of eccentricity.
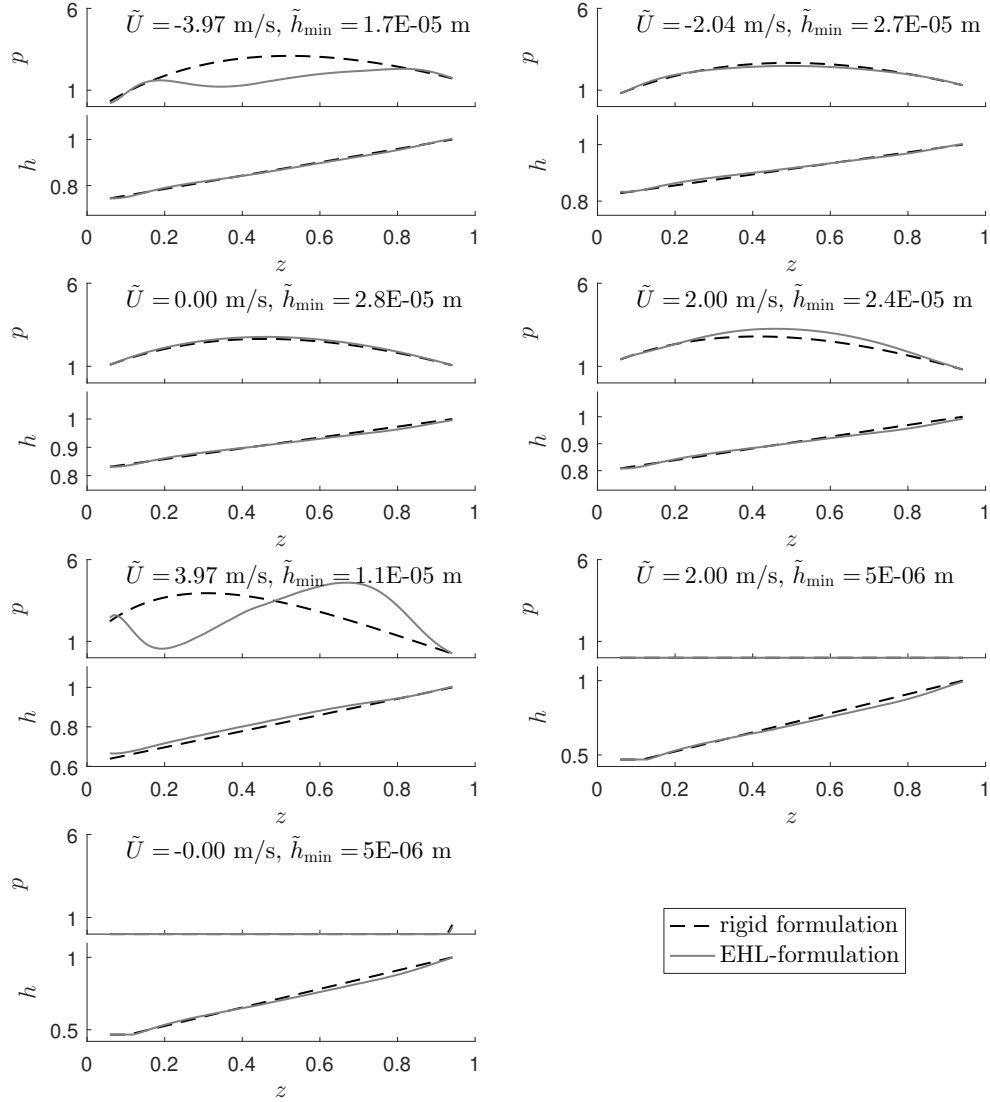

Figure 6.11: Gap and pressure distribution along piston at at $\phi = 0$: EHL vs. rigid formulation; $p = \tilde{p} - p_{\text{amb}}, h = \tilde{h}/\tilde{h}_{\text{max}}$

Table 6.5: Impact of $\widetilde{\text{gap}}_{\text{min}}$ on net-oil flow

$\widetilde{\text{gap}}_{\text{min}}$ in μm	net oil flow in l/h	percent
4	-0.76	100 %
5	-0.81	106 %
6	-0.86	113 %
7	-0.90	118 %
8	-0.95	125 %

6.2.2 Impact of minimal gap

Using the model covered in the previous section, the impact of the minimal prescribed gap shall be researched. Several calculations were done, with changing $\widetilde{\text{gap}}_{\text{min}} = 4\,\mu\text{m}$–$8\,\mu\text{m}$. Results are shown in Fig. 6.12, the impact on the net-oil flow is given in table 6.5. Changes of this parameter have a big impact on the results: The net-oil flow increases by 25 % when doubling $\widetilde{\text{gap}}_{\text{min}}$ from $4\,\mu\text{m}$–$8\,\mu\text{m}$, almost linearly. The point of times, when the piston starts and stops moving up is solely dependent on $\tilde{U}$, but independent of $\widetilde{\text{gap}}_{\text{min}}$. Therefore, the piston's vertical position is dependent on the prescribed $\widetilde{\text{gap}}_{\text{min}}$ throughout the calculation, and not only while the piston is in the mixed lubrication regime. Therefore, $\widetilde{\text{gap}}_{\text{min}}$ should be defined with care: An arbitrary increase to avoid numerical difficulties is not justified.
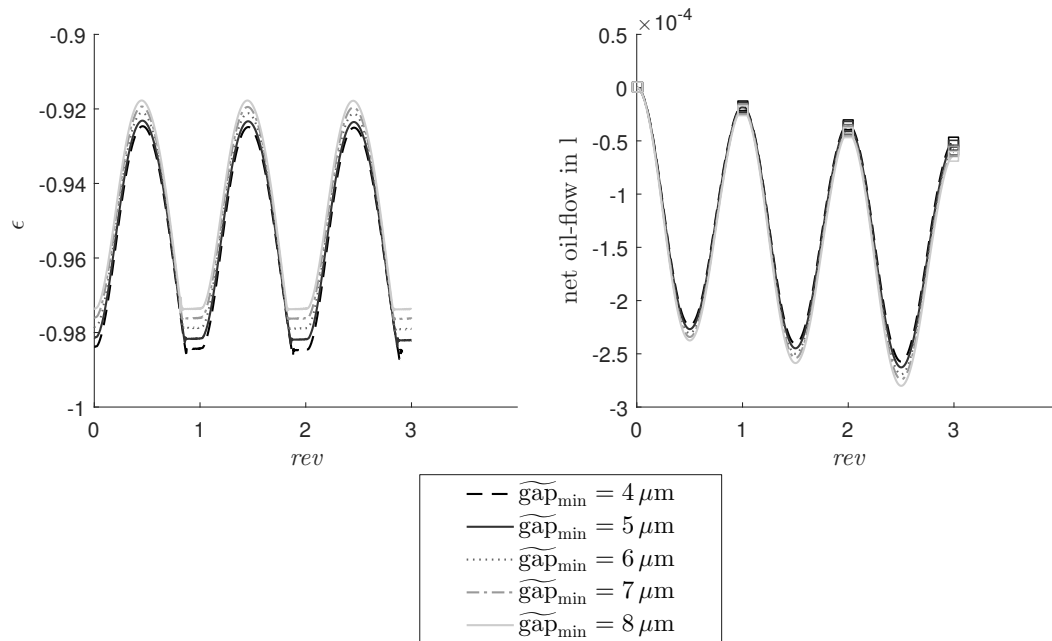

Figure 6.12: Eccentricity (left image) and net oil-flow: impact of minimal gap

Table 6.6: Parameters of simulated compressor;

number of rings	gas type	cylinder clearance	stroke	$\tilde{\phi}_{\mathrm{valve}}$	
4	96% H_2	$3.2 \times 10^{-4}\,\mathrm{m}$	$400\,\mathrm{mm}$	$10.62\,\mathrm{cm}^2$	
$\tilde{w}_{\mathrm{r}}$	$\tilde{h}_{\mathrm{r}}$	$\tilde{d}_{\mathrm{cyl}}$	$\tilde{p}_{\mathrm{s}}$	$\tilde{p}_{\mathrm{d}}$	$\tilde{T}_{\mathrm{d}}$
$79\,\mathrm{mm}$	$8\,\mathrm{mm}$	$190\,\mathrm{mm}$	$10\,\mathrm{bar}$	$25\,\mathrm{bar}$	$123\,^\circ\mathrm{C}$
$\tilde{m}_{\mathrm{P}}$	$\tilde{I}_{\mathrm{P}}$	$\tilde{l}_{\mathrm{P}}$	$\tilde{b}_{\mathrm{P}}$	$\tilde{l}_{\mathrm{CH}}$	$\tilde{l}_{\mathrm{CH2}}$
$70.9\,\mathrm{kg}$	$1.37\,\mathrm{kg\,m}^2$	$1.65\,\mathrm{mm}$	$422\,\mathrm{mm}$	$348\,\mathrm{mm}$	$41\,\mathrm{mm}$
$\tilde{m}_{\mathrm{CH}}$	$\tilde{\rho}_{\mathrm{PR}}$	$\tilde{E}_{\mathrm{PR}}$	$\tilde{r}_{\mathrm{PR}}$	$\tilde{A}_{\mathrm{PR}}$	$\tilde{J}_{\mathrm{PR}}$
$126\,\mathrm{kg}$	$7800\,\mathrm{kg/m}^3$	$210\,000\,\mathrm{MPa}$	$40\,\mathrm{mm}$	$0.005\,\mathrm{m}^2$	$2.01 \times 10^{-6}\,\mathrm{m}^4$
$\tilde{h}_{\mathrm{pr}}$	$\tilde{w}_{\mathrm{pr}}$	$\tilde{E}_{\mathrm{pr}}, \tilde{E}_{\mathrm{r}}$	$\tilde{m}_{\mathrm{CR}}$	$\tilde{l}_{\mathrm{CR}}$	$\tilde{l}_{\mathrm{CR1}}$
$11\,\mathrm{mm}$	$9\,\mathrm{mm}$	$8000\,\mathrm{MPa}$	$178\,\mathrm{kg}$	$1000\,\mathrm{mm}$	$350\,\mathrm{mm}$
$\tilde{c}_0$	$\tilde{c}_{0,\mathrm{CH}}$	rpm	$\tilde{I}_{\mathrm{CH}}$	$\tilde{l}_{\mathrm{b}}$	$\tilde{m}_{\mathrm{PR}}$
$0.32\,\mathrm{mm}$	$0.25\,\mathrm{mm}$	$370\,\mathrm{min}^{-1}$	$0.72\,\mathrm{kg\,m}^2$	$1009\,\mathrm{mm}$	$42\,\mathrm{kg}$

Table 6.7: Global lubrication model: simulation parameters

$\widetilde{\mathrm{gap}}_{\mathrm{min}}$	$2\,\mathrm{\mu m}$
number of nodes in axial direction	50
number of nodes in azimuthal direction	40
rel. solver tolerance	1×10^{-3}
abs. solver tolerance	1×10^{-6}

6.3 Results of global cylinder lubrication model (MATLAB)

The global cylinder lubrication model comprises the models and implementations, which were mentioned in the course of this work. It focuses on the net-oil transport along the piston assembly and neglects oil consumption due to evaporation (see Sec. 1.4). Gas driven oil flow dynamics affecting the oil trace of each ring are neglected based on the findings in Sec. 5.2 and Sec. 6.1. Since the focus lies on the net-oil transport, oil accumulation on the dead centre positions do not need to be studied further: Once accumulated, it does not affect the solution in the further course of the calculation and is transported through the discharge valve anyhow.

The objective is to find a steady motion of the global compressor dynamics. Once this task is accomplished, the focus lies on finding lubrication conditions, where the rings work with zero or small starving parameters *St* and then to evaluate the net-oil flow at this state. This is done without tuning any parameters: Initially, a uniform oil film is prescribed over the cylinder wall, and the progression of the oil film is studied.

The global cylinder lubrication model is applied to the case of a real compressor

Table 6.8: Simulation parameters: main case

$\tilde{\mu}_\mathrm{f}$	$0.1\,\mathrm{Pa\,s}$
initial crank angle	$9°$

(a "Maschinenbau Halberstadt" compressor), which allows to compare results with in-use lube rates, provided by state-of-the-art guidelines. The compressor-specific parameters are provided by ©HOERBIGER and summarized in table 6.6. This compressor was chosen, because it is a representative, usual compressor, having a sufficient number of rings to clearly show their interplay and its consequences. The basic geometry of its piston assembly is shown in Fig. 6.13, including piston, piston rod, one rider ring and three piston rings.

Cylinder and crosshead guide are assumed to be aligned perfectly coaxial. The tilt at rest, dependent on the vertical position of the crosshead guide relatively to the piston is chosen to $\alpha = 0$ according to [33, Annex C], which basically says that the difference between cylinder clearance and crosshead clearance should be balanced by a vertical offset of the crosshead guide. Simulation parameters are found in table 6.7. In advance to the global cylinder lubrication simulation, the time dependent pressure levels next to the piston rings are calculated, which are shown in Fig. 6.14.
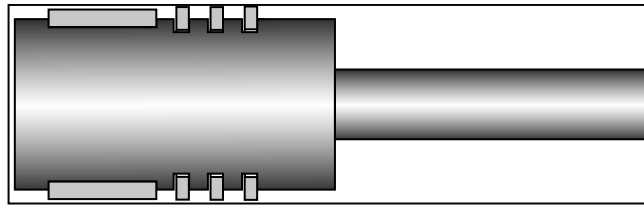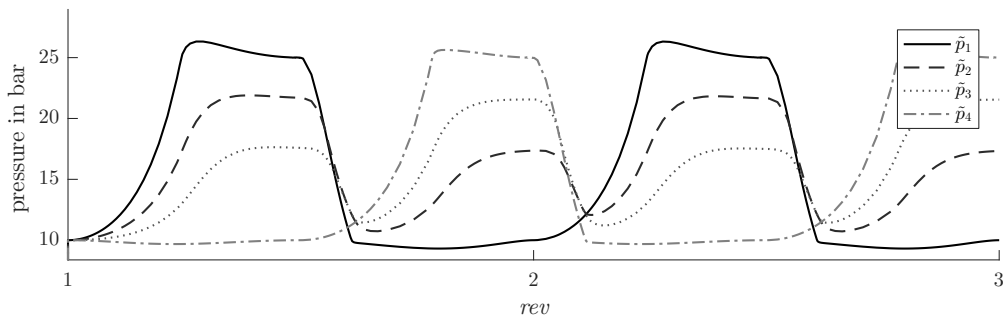

Figure 6.13: Basic geometry of the piston assembly;

Figure 6.14: Time dependent pressure levels next to piston rings;

6.3.1 Detailed simulation results of test case

Detailed model results are presented using a simulation case with initial conditions shown in table 6.8. The calculation is started shortly after the top dead center position with a positive piston velocity — the piston shown in Fig. 6.13 starts moving to the right side. The initial crank angle shows to have a big impact on the calculation, since it greatly affects the first oil trace which is left on the cylinder wall by the rings, as well as the volume of the outer transition zones.

In this simulation case, the piston rings, which are positioned on the right side of the rider ring, scratch most of the oil away and cause the rider ring to operate in partially wetted lube conditions from the start on. This is seen in Fig. 6.15, which shows the piston eccentricity over time: The piston sinks rapidly from its initial position, until the gap between rider ring and cylinder wall is partly filled with oil ($rev \approx 0.05$). Shortly afterwards, the rider ring overruns the trace of the first piston ring and its fully flooded region decreases, leading to a further lowering of the piston: Lower gaps result in higher pressures and compensate for the smaller region of pressure built up.

The oil film traces of the piston and rider rings at different moments of time are shown in Fig. 6.16: The plots presenting the oil film trace at half-revolutions (piston is at bottom dead centre — first and third plot from the top) clearly show an oil film trace starting with high values (defined by the oil flow out of the fully flooded region), merging into much smaller film heights resulting from the piston ring's oil film trace when the fully flooded ring region vanished for a certain value of ϕ. Fully flooded ring regions vanish faster at higher gap values which correspond to higher values of ϕ due to the negative piston's eccentricity. This and the following contour plots also show the numerical resolution of 50×40 nodes.

About three quarters of the rider ring are not wetted at all: Each revolution, the wetting angle ϕ_{w} of the rider ring decreases from 83° to 28°. The evolution of the fully flooded ring region at bottom dead centre position is shown in Fig. 6.17. After a steady state is reached (after approx 5 revolutions), a decline is apparent, indicating a decrease of the fully flooded ring region, finally leading to under-lubrication of the rider ring. It causes the piston's eccentricity to decrease each cycle (see Fig. 6.18), finally resulting in a contact, which is also clearly visible through the starving parameter St (see Fig. 6.19).

The piston rings, on the other hand, are partly working in the mixed lubrication regime from the beginning — see St, which is between 0.3–0.5. Their initial positions ($y_{\mathrm{pr}}(\phi)$) are calculated to fulfil the radial force equilibrium with a zero-squeeze term. Therefore, all piston ring parts having divergent gaps ($\phi > \pi/2$) start in contact and leave a trace $\approx \widetilde{\mathrm{gap}}_{\mathrm{min}}/2$. The oil volume in between the rings is not enough to provide sufficient oil to keep the ring surfaces fully lubricated. Figure 6.20 shows the total oil volume between rings and cylinder wall over time.

Although the global system dynamics show a steady state, we detect revolution dependent changes due to changes of the oil film distribution over time. The significant oil volume changes in the rider ring gap compared to the oil volume changes
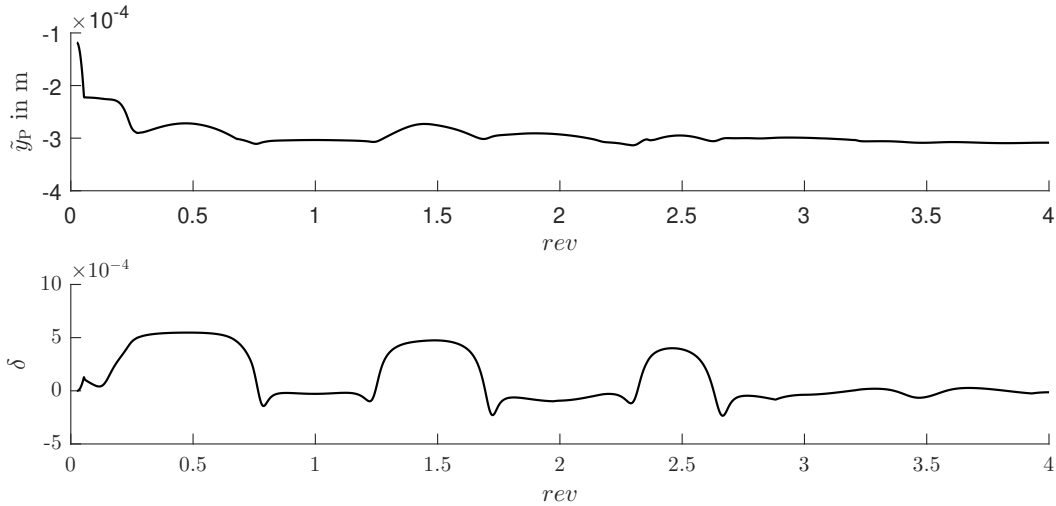
Figure 6.15: Time dependent piston eccentricity and piston tilt;

in the piston ring gaps are driven by the passive ring surface, which is not wetted. Near the top dead centre position, the oil film heights are not changed by the piston rings. Hence, they show their initial values of 0.1 mm (yellow region in Fig. 6.16).

Looking at Fig. 6.21 we see the total volume progression of the outer transition zones (summed up over all ϕ): the outer piston rings scratch oil away (ring four when going rightwards, ring two when going leftwards), causing additional starving of ring three. Minima near zero are due to the squeeze effect: Oil is drawn into the ring gap when it increases quickly. At each cycle, the rider ring accumulates oil on the right side when going rightwards, but its maximum oil volume, as well as the time period of oil accumulation decreases each cycle.

Let us get back to the global cylinder lubrication model results shown in Fig. 6.18. Looking at the vertical piston velocity $\dot{\tilde{y}}_P$, we see a local minimum, followed by a local maximum each cycle, when the piston reaches the bottom dead centre position ($rev = 6.5, 7.5, 8.5, ...$). This is explained by an increase of the fully flooded ring region when the piston moves left again, which decelerates the piston's vertical motion. Figure 6.22 shows the evolution of gap, pressure and volume fraction in this period.

The calculated piston force shows a high level of noise. This is due to the high dependency of pressure distribution on the gap size. Small variations of eccentricity in the order of calculation accuracy cause therefore visible force peaks. This behaviour is improved by choosing higher calculation tolerances. However, comparative calculations have shown negligible influence on the piston's eccentricity and on the net oil flow. The chosen tolerances are a good compromise between calculation accuracy and calculation speed.

The maximal piston rod bending in the order of a few hundredths of millimetres seems negligible at first glance. However, the piston tilt is more than twice as high
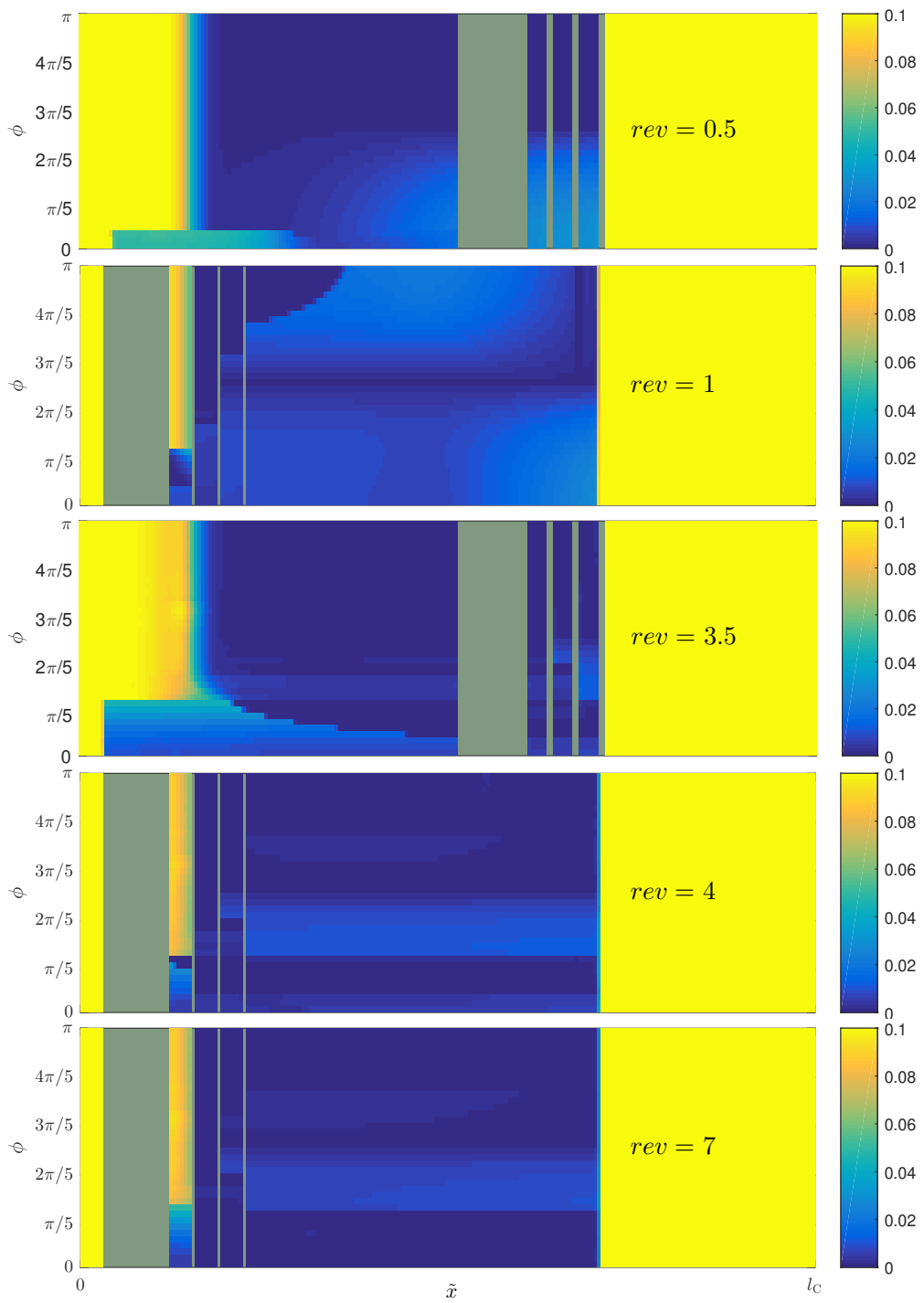
Figure 6.16: Oil film trace on developed cylinder wall at different moments in time, values are shown in mm; rings are shown in gray.
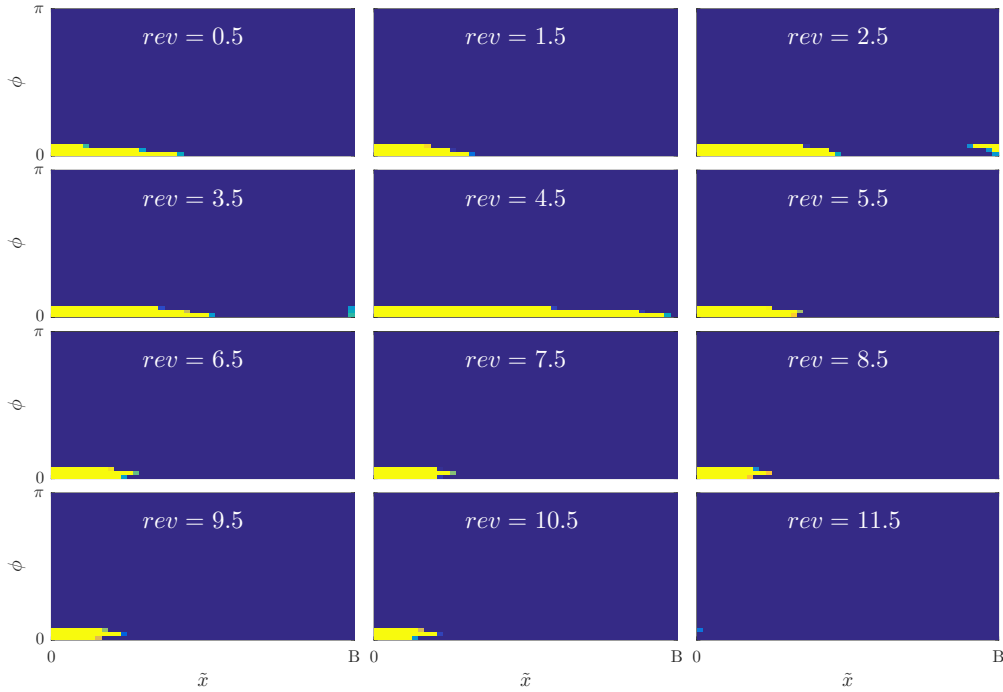
Figure 6.17: Fully flooded oil regions (shown in yellow) at bottom dead centre over time, shown on the developed cylinder wall;

as the crosshead tilt and has certainly a significant impact on the solution.

6.3.2 Net-oil flow

The accumulated oil flow along each ring is evaluated at the left-side cross section of each ring: The volume flow over each time increment is summed up, starting at the top dead center position. To get the net-oil flow in l/day, the difference of the accumulated oil flow over two revolutions is evaluated and then extrapolated. The accumulated oil flow along each ring is plotted in Fig. 6.23, including the resulting net-oil flow (see also table 6.9), extrapolated by use of the last two simulated revolutions. Additionally, the progression of the net-oil flow is shown in Fig. 6.24: This plot shows the predicted net-oil flow for each $rev = i$ by taking the accumulated oil flow of $rev = i - 1$ and $rev = i$ into account. All rings have a negative net-oil transport. Hence, they transport oil from the right to left side, which is also evident when taking a look at the change of oil reservoirs in time (see Fig. 6.25). The lower oil transport of the second ring (relatively to the first ring) reinforces the increase of partially wetted rider ring regions and finally leads to its under-lubrication.

It should be noted that table 6.9 shows the net-oil flows along the rings, calculated at a point of time, where the dynamical system shows steady behaviour. However, under these conditions, the rider ring already undergoes starved conditions, while the piston rings are still in a transient period.
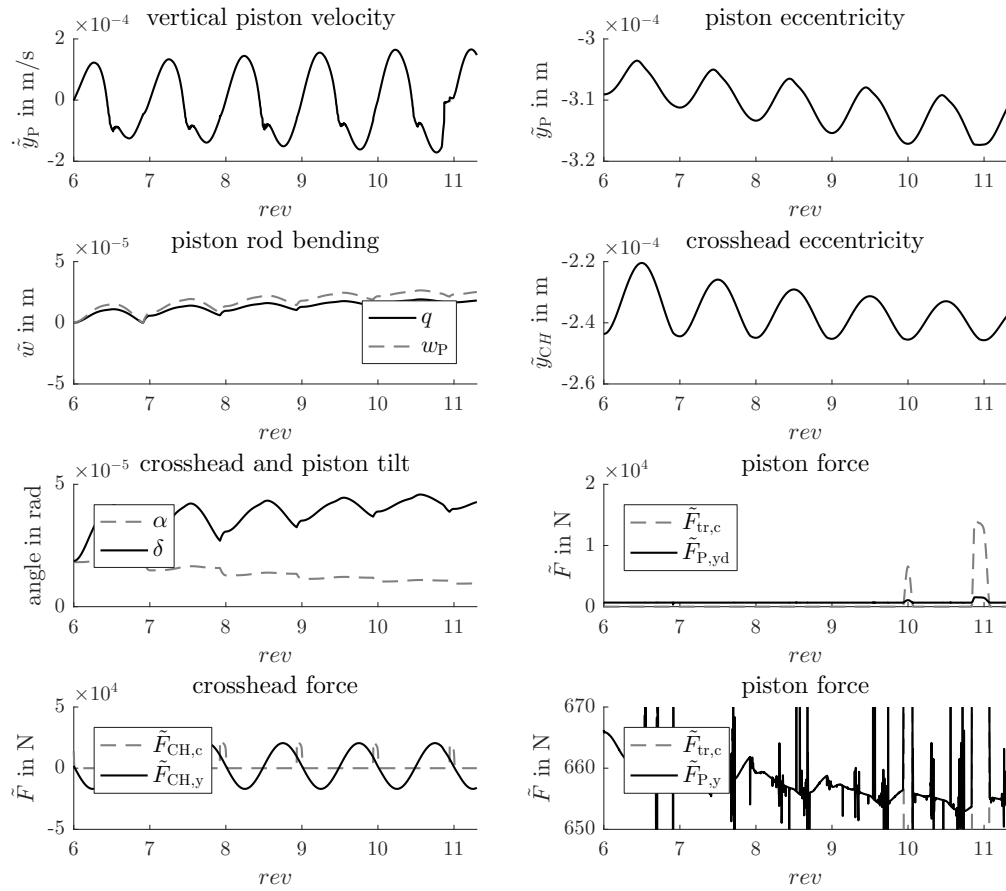
Figure 6.18: Selection of dynamical compressor model results;

Table 6.9: Global compressor model: net-oil flow; ring 2–4 are not working in steady state yet;

ring 1 (rider ring)	$-4.56\,\mathrm{l/day}$
ring 2 (piston ring)	$-2.17\,\mathrm{l/day}$
ring 3 (piston ring)	$-3.29\,\mathrm{l/day}$
ring 4 (piston ring)	$-2.28\,\mathrm{l/day}$
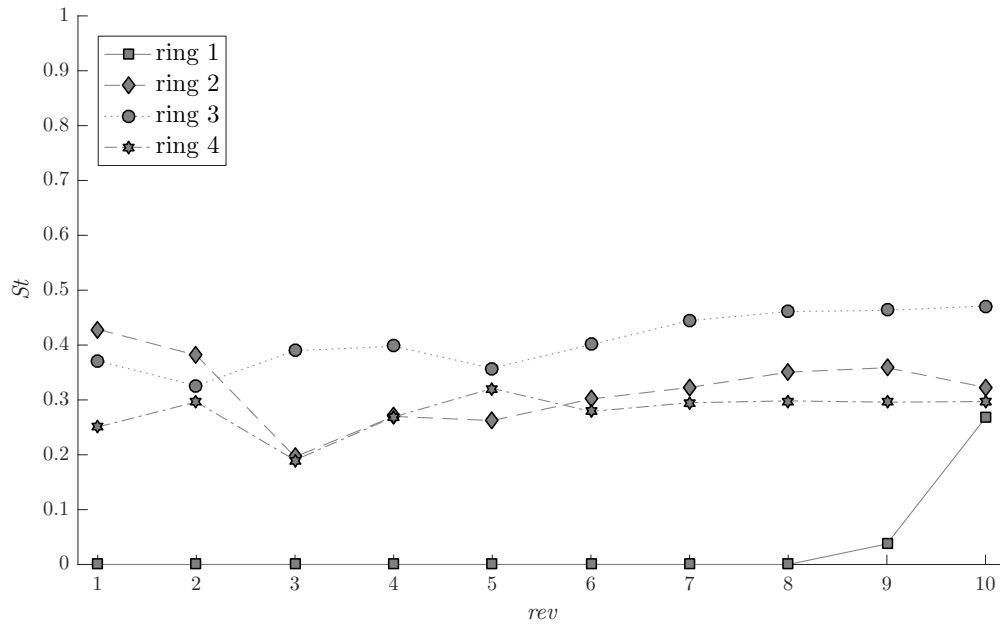
Figure 6.19: Starving parameter for each ring;
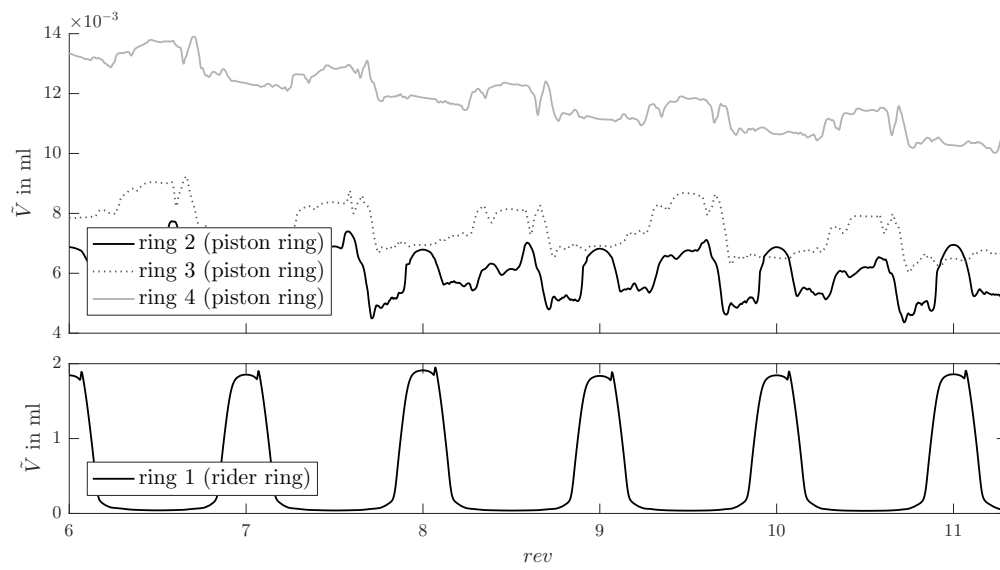
Figure 6.20: Oil volume in ml between rings and cylinder wall and its progression over time;

Figure 6.21: Progression of total oil volumes of transition zones;

Looking for example at *St* of the piston rings (Fig. 6.19) or at the progression of the oil film trace (Fig. 6.16) one can conclude that the minimal gap between piston rings and cylinder wall decreases in time: The piston ring partly lifts off in the first revolutions, which is possible due to the wedge effect. However, once a steady dynamical state is reached, the piston's tilt reduces significantly compared to the transient period at start of calculation. Therefore, the piston ring motion sha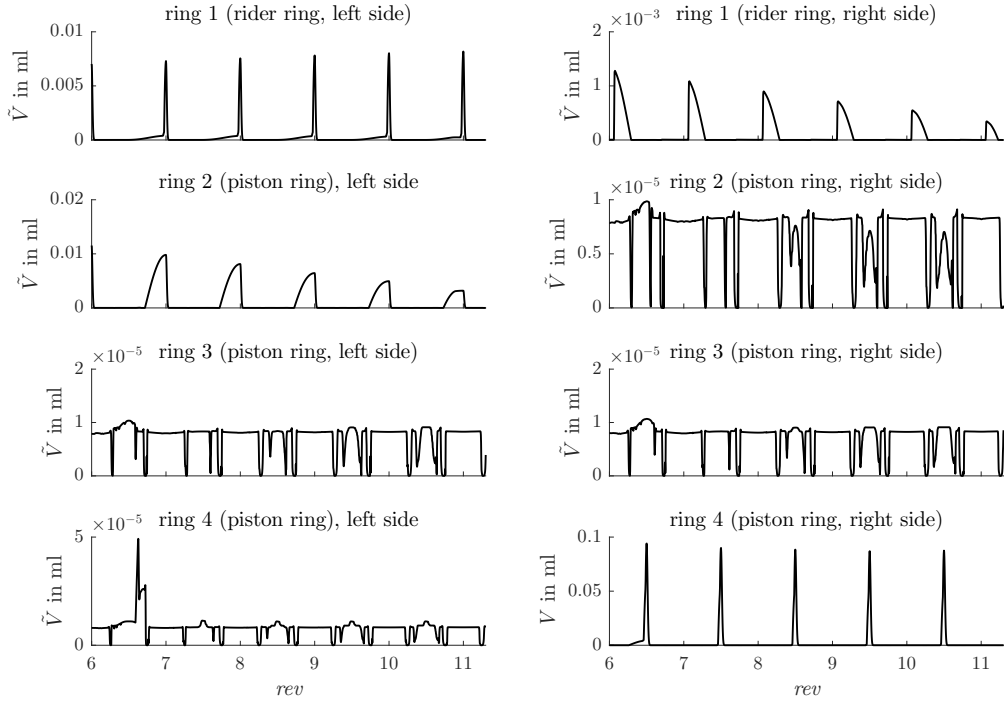ll be investigated further under the assumption of a steady state: The results of the compressor model (tilt and eccentricity) of the steady state are taken and extrapolated to a wider range of time. Then the motion of all piston rings is calculated, assuming fully flooded ring areas for the complete calculation, perfectly flat surfaces and reducing the minimal gap height to $0.1\,\mu m$.

The progression of the minimal gap for different values of ϕ is plotted in Fig. 6.27: The transient period takes many revolutions (steady conditions are not reached after 300 revolutions). The rings are working at approx. 0.5 microns gap heights. A comparison of the pressure levels between rider ring and piston rings shows that the additional oil pressure built up between rider ring and cylinder wall is around $1\,bar$, compared to up to approx. $8\,bar$ for the oil pressure built up between piston ring and cylinder wall. This explains the lower piston ring gaps, since the same piston inclination defines both the inclination of rider– as well as for piston rings. Another piston ring profile (either manufactured or altered by wear) would allow a higher pressure built up and might allow an operation at higher gap heights.
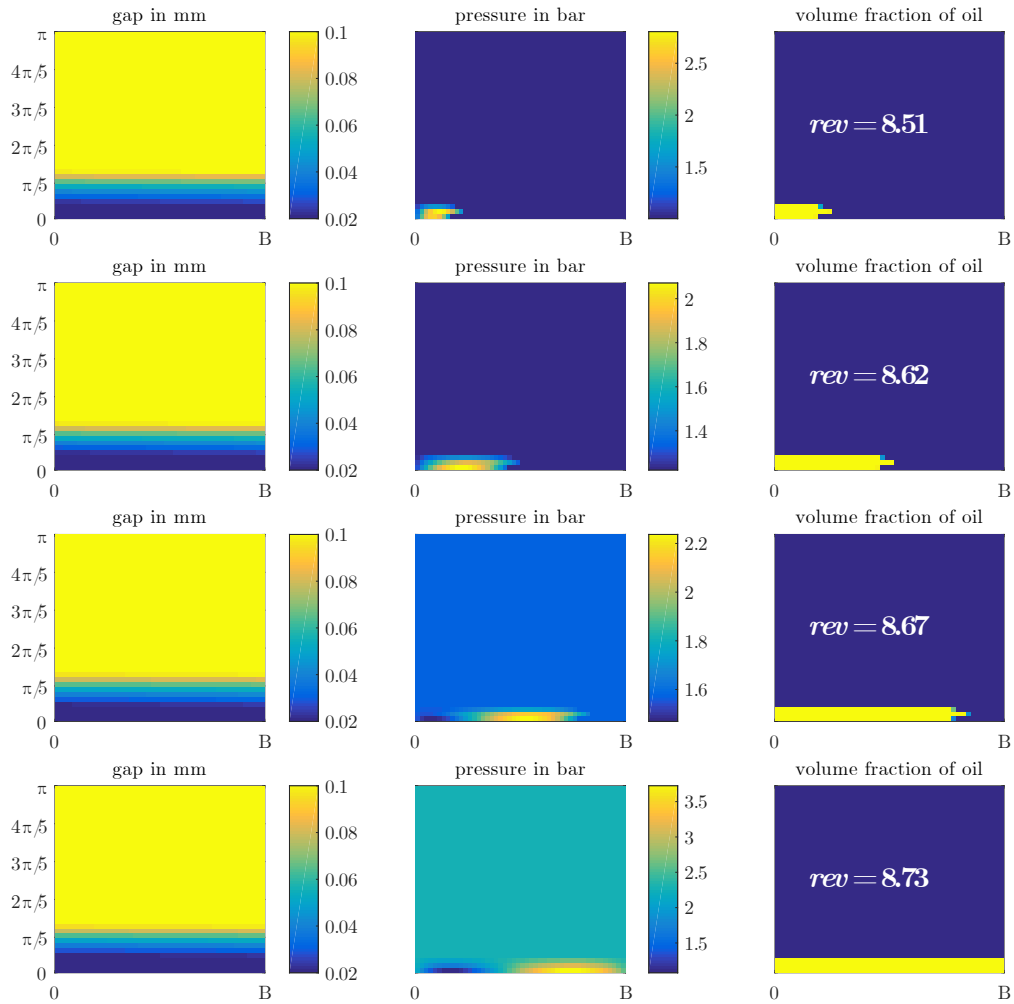
Figure 6.22: Gap, pressure and volume fraction of oil (yellow corresponds to fully flooded gap) at bottom dead center and afterward.
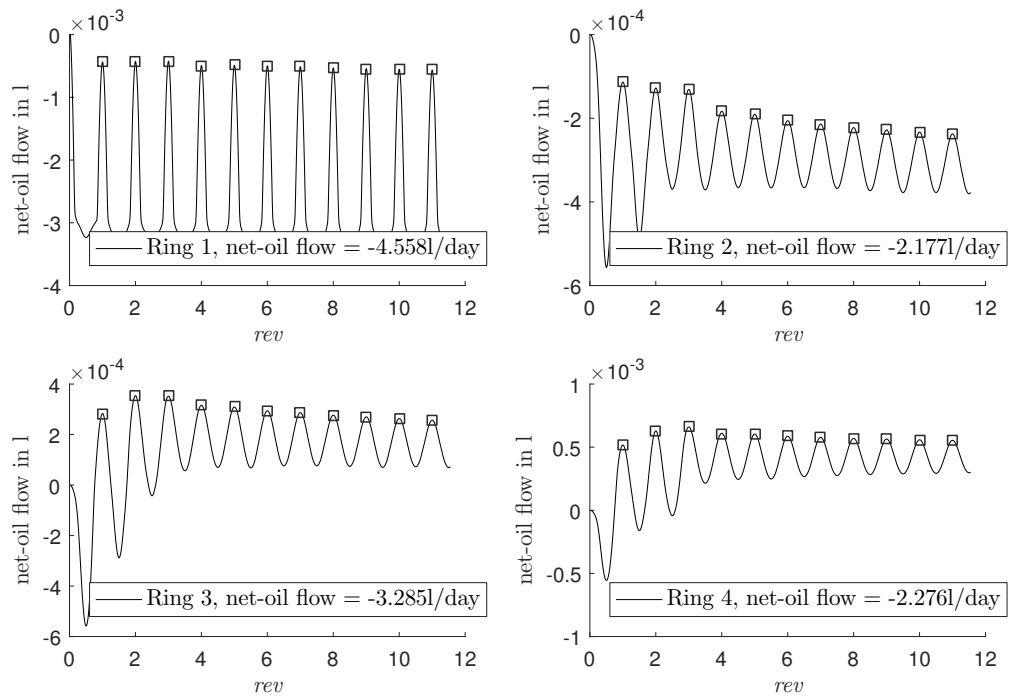
Figure 6.23: Accumulated oil flow along rider and piston rings;
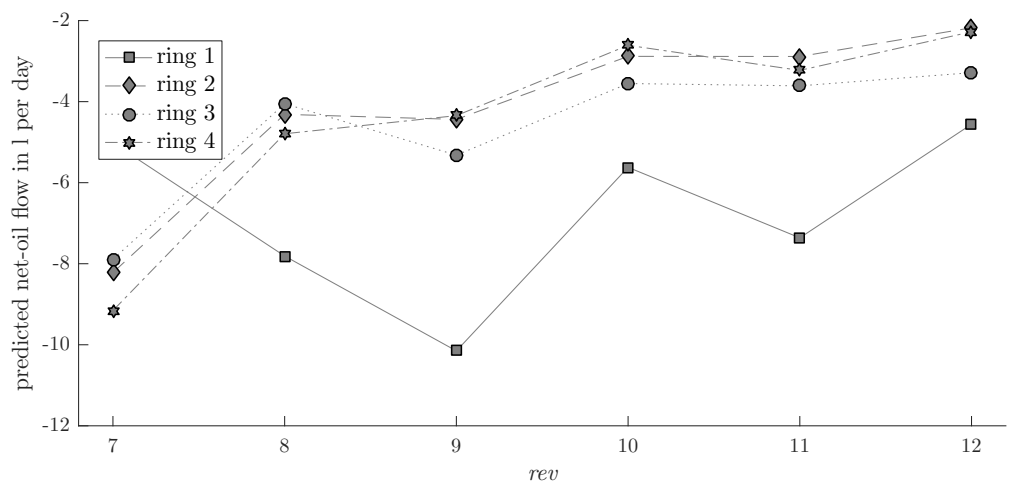
Figure 6.24: Net-oil flow over two periods extrapolated to get oil consumption per day and its progression over time;
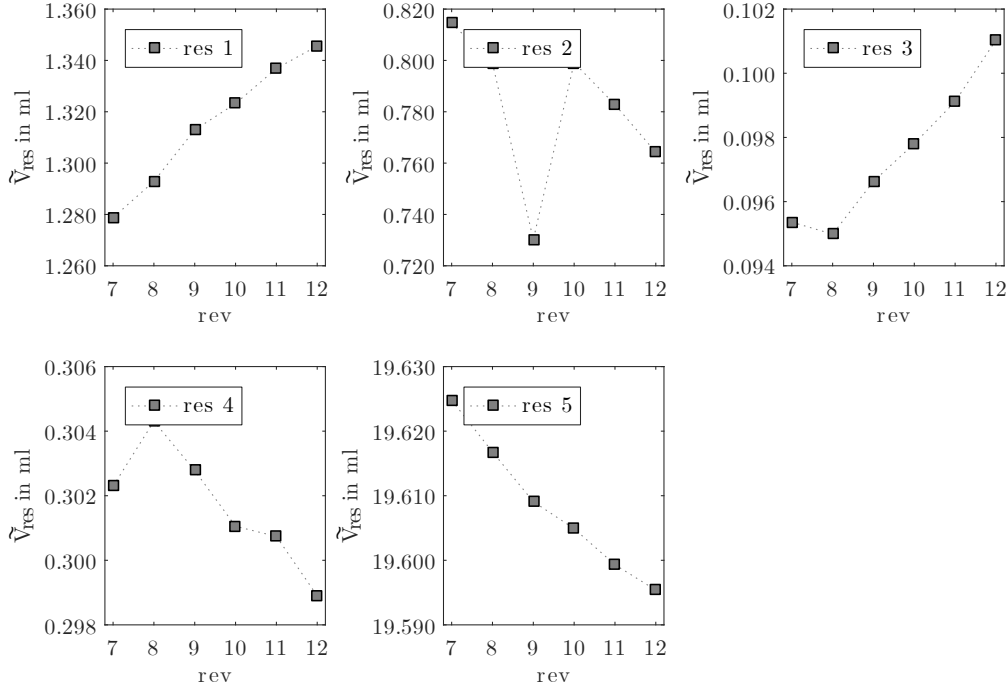
Figure 6.25: Total oil volume in of each reservoir and its progression over time;

These "steady state" calculations yield a significantly lower net-oil flow of approx. $-0.01\,\mathrm{l/day}$. The total oil volume, which is transported from one side to the other over half a revolution is approx. $0.1\,\mathrm{ml}$. This is the amount of oil which should at least cover the cylinder wall next to the piston rings. Of course, the net-oil flow is much less, since most of the oil is transported back during the second half of revolution (see Sec. 3.2). Hence, in this configuration, the piston rings act as an oil barrier, which are working at small gap heights of approx. $0.5\,\mathrm{\mu m}$. Changes of the resulting gap due to elastic ring deformations play, however, a significant role in this regime, but where neglected in this calculation. Therefore, this result needs to be interpreted with caution.

The net-oil flow along the rider ring has been estimated by evaluating the accumulated oil flow over two revolutions, starting at the top dead centre position, when the dynamic system has reached a steady state. However, the piston rings are certainly in a transient period yet, not having reached a steady state. Regardless, the accumulated volume flow along the rider ring is hardly affected by this circumstance: The maximal wetting angle ϕ_w of the rider ring is 83°, the oil in the remaining gap is passive and does not affect the net-oil flow along the ring. In the important area ($\phi_\mathrm{w} < 83°$), the left piston ring is already working as a barrier at small gap heights, accumulating oil at the left side of the ring (see Fig. 6.23). The final net-oil flows along the rings are summarized in table 6.10.

Finally, the assumption that the piston ring sits solidly in the groove flank (a), as

Table 6.10: Global compressor model: final net-oil flow in steady state;

ring 1 (rider ring)	$-4.56\,\mathrm{l/day}$
ring 2–4 (piston rings)	$-0.01\,\mathrm{l/day}$
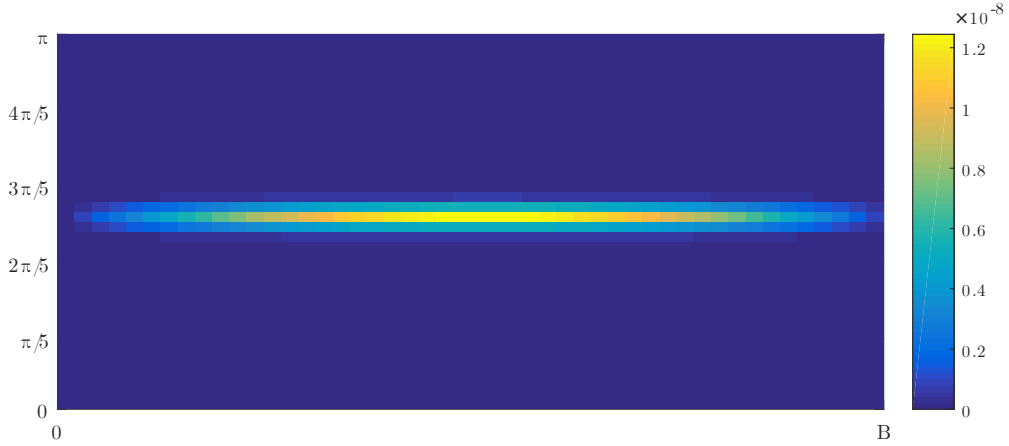
Figure 6.26: Relative error of pressure distribution (1D compared with 2D);

wall as the 1D-assumption (b) (see Sec. 3.4) shall be validated. To validate assumption (a), (5.15) is checked: Results show, that it is satisfied for all $\tilde{F}_{\mathrm{pr,cont}}(\phi) \gg 0$. If $\tilde{F}_{\mathrm{pr,cont}}(\phi)$ decreases towards zero, this assumption is not justified any more, which is acceptable, since the violation of this condition occurs during the the ring shuttling event, which is neglected anyhow. For validation of assumption (b) (see Sec. 5.1.4), the pressure profiles calculated by the 1D-Reynolds equation and by the 2D-Reynolds equation shall be compared: The ring deformation as a result of the 1D-calculation is taken and used to calculate the 2D-Reynolds equation. The relative error is shown in Fig. 6.26. The greatest relative error is found in the symmetry plane, but even there, the error due to the 1D-assumption is negligible.

6.3.3 Impact of dynamic viscosity

The dependence of the system behaviour on viscosity shall be evaluated. It follows from the Reynolds equation, that under the assumption of fully lubricated, convergent gaps, the required gap height increases with increasing dynamic oil viscosity for a certain load. This is apparent in Fig. 6.29, which shows the piston eccentricity at the transient period for different viscosities. Let us take a look at the period $rev = 1$–2: While $rev = 1$–1.5, the piston moves to the right side, oil is transported to the left side. Higher viscosities correspond to greater gaps, resulting in a higher oil flow to the left along the rider ring. Since the oil delivery is limited by the piston ring upstream, higher gaps result in a faster decrease of the fully flooded ring area,
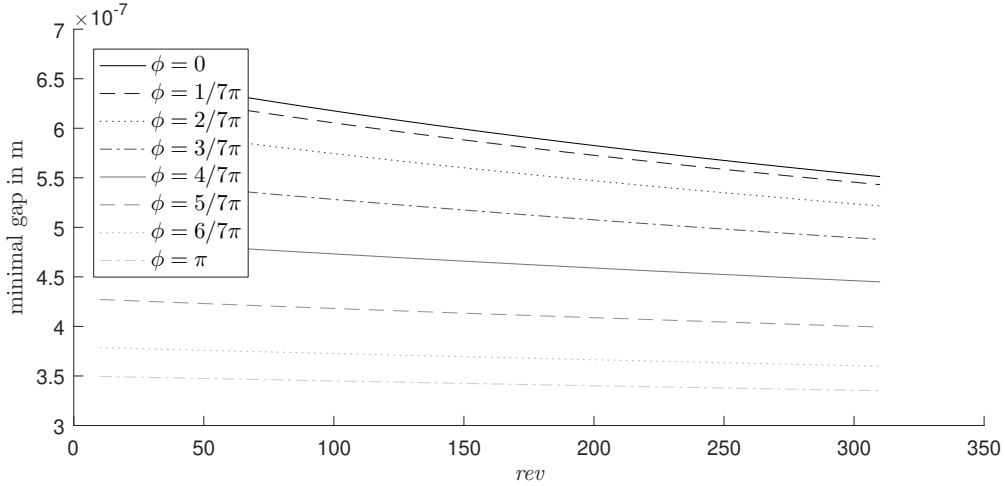
Figure 6.27: Minimal time dependent gap of left piston ring for $\phi = 0$–π;

Table 6.11: Global cylinder lubrication model: net-oil flow (along rider ring) dependence on dynamic oil viscosity

$\tilde{\mu}_\mathrm{f} = 0.1\,\mathrm{Pa\,s}$	$-4.56\,\mathrm{l/day}$
$\tilde{\mu}_\mathrm{f} = 0.03\,\mathrm{Pa\,s}$	$-1.1\,\mathrm{l/day}$

which in turn leads to a lowering of the piston. Therefore, the ring gap decreases faster, resulting in a lower oil flow to the right side along the rider ring. The faster decline of the fully flooded rider ring area for higher $\tilde{\mu}_\mathrm{f}$ is shown in Fig. 6.30. In the simulation case with $\tilde{\mu}_\mathrm{f} = 0.3\,\mathrm{Pa\,s}$, the fast decline of the fully flooded rider ring areas results in $St > 0$ for $rev \geq 2$. Compare to $St = 0$ for the other two simulation cases with lower viscosities. Since the rider ring starts to starve rapidly for $\tilde{\mu}_\mathrm{f} = 0.3\,\mathrm{Pa\,s}$, a net-oil flow can not be estimated but can be assumed to be higher than the net-oil flow for $\tilde{\mu}_\mathrm{f} = 0.1\,\mathrm{Pa\,s}$. The estimated net-oil flows for $\tilde{\mu}_\mathrm{f} = 0.03\,\mathrm{Pa\,s}$ and $\tilde{\mu}_\mathrm{f} = 0.1\,\mathrm{Pa\,s}$ are shown in table 6.11: The net-oil flow decreases significantly with decreasing oil viscosities.

6.3.4 Derivation of a lube strategy

The following main conclusions can be drawn by studying the numerical results presented above:

- There is a net-oil flow to the left along all rings.

- The rider ring being the first ring at the left side has the highest net-oil flow in steady state.
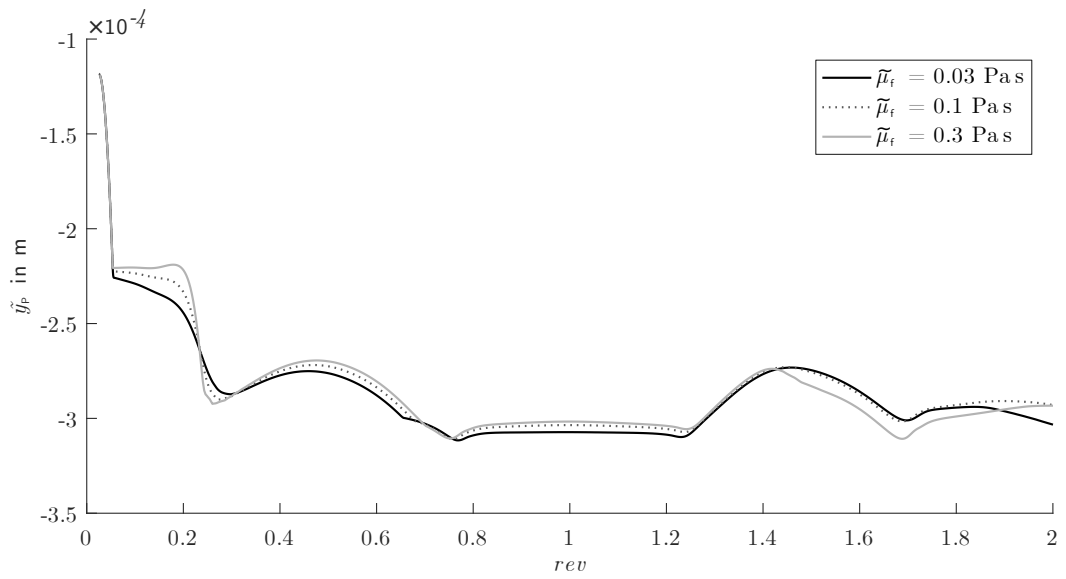
Figure 6.28: Piston eccentricity and its dependence on dynamic oil viscosity;
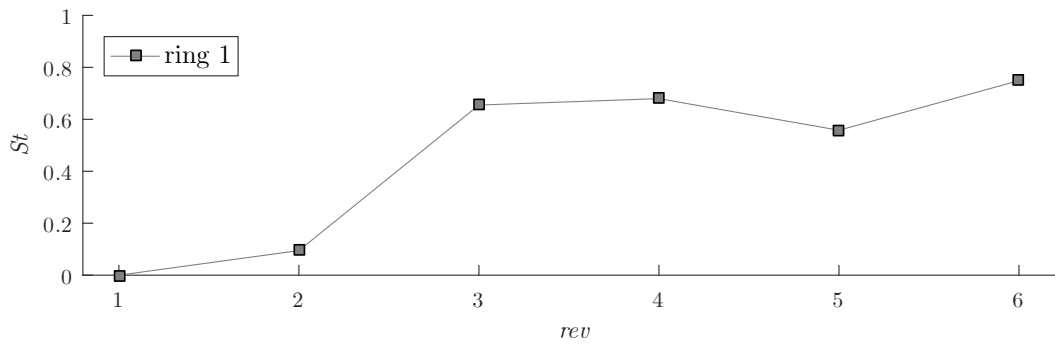
Figure 6.29: Starving parameter for $\tilde{\mu}_\text{f} = 0.3\,\text{Pa}\,\text{s}$
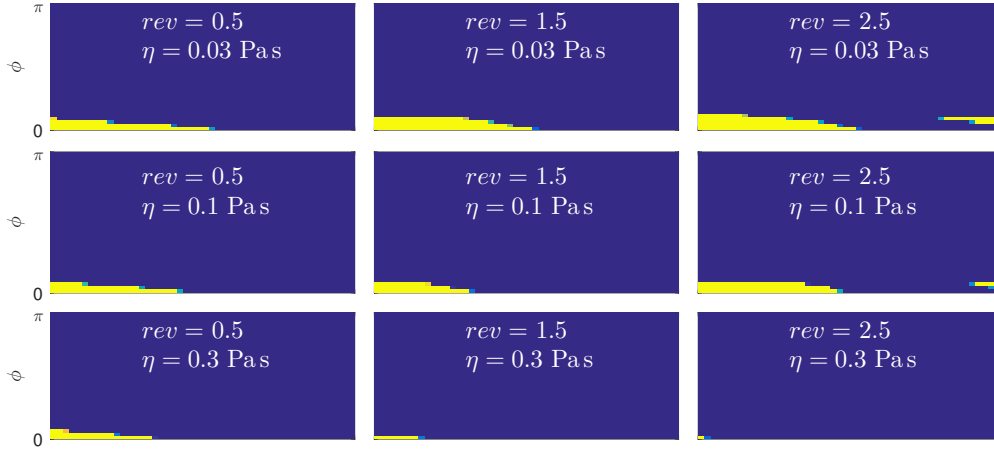
Figure 6.30: Progression of volume fraction of oil (yellow corresponds to fully flooded gap) at bottom dead center for three revolutions and its dependence on dynamic oil viscosity;

- The piston rings are working all time at very small gap heights of approx. 0.5 μm and act as an oil barrier.

- Increase of dynamic oil viscosity leads to a higher net-oil flow and accelerates starving conditions.

Due to the many input parameters, a lube strategy is case-dependent. Concerning the presented compressor it should take conclusions mentioned above into account and should include the following points:

- An oil feed rate of approximately $1.1\,\mathrm{l/day}\times$ safety factor is estimated.

- Oil should be injected to the right side of the rings.

- Oil should be injected to two positions: (1) about 99 % of the total lube oil to the right side of the rider ring and (2) the remaining part additionally to the right side of ring 4 (ring at right side). The rider ring only benefits from oil supply at the bottom of the cylinder (near $\phi = 0$), which suggests to inject the oil at the bottom of the cylinder, the piston rings need an oil supply at the whole circumference, which suggests to inject the oil at multiple points along the circumference.

- A dynamical oil viscosity of $\tilde{\mu}_\mathrm{f} = 0.03\,\mathrm{Pa\,s}$ proved sufficient to prevent a contact between rider ring and cylinder wall. Higher viscosities increase the net-oil flow along the rings and accelerate the increase of starving regions.

Case independently, it can be said that it seems advantageous to inject often, but small amounts of oil: Especially the rider ring should only be wetted at the region necessary to hold its weight. If other regions ($\phi > \phi_\mathrm{w}$) would get fully flooded by

oil due to a big lubricant quantity, it would just increase the net-oil flow, but would not increase the ring's lifetime. On the other hand, injecting bigger amounts of oil increases the risk of inertial driven formation of oil mist, which gets lost through the discharge valves.

The oil feed rate stated above is derived by the net-oil flow along the rider ring, greatly dependent on the wetting angle, which is influenced by the initial oil film height on the cylinder wall. It is certainly possible, that a smaller wetting angle — which would probably decrease the net-oil flow, would be sufficient to keep the rider ring operating in the hydrodynamic regime.

It is very encouraging, that empirical guidelines (e.g. Fig. 1.9, [30, Ch. 18], etc.) yield quite similar lube rates between 0.5–15 l/day, strengthening the derived global cylinder lubrication model to represent the most important effects leading to oil consumption.

7 Summary and critical discussion

In the course of this work, a comprehensive lubrication model for cylinder lubrication of reciprocating piston compressors was developed, which deepens the insight into the mechanisms of oil loss. A short summary of central aspects follows, preceding a critical discussion about the findings and limitations of this study.

7.1 Summary

The lubrication model was derived by focusing on the oil film dynamics on the cylinder wall: First, the oil film dynamics, where the lubrication effect comes into play (the contact areas of rider rings and piston rings), were investigated, requiring detailed knowledge of piston ring and rider ring motion. This led to the necessity to describe the piston motion in detail. Therefore, a 3-DOF model (vertical crosshead movement, tilt of piston rod, bending of piston rod) was developed, which is able to describe the secondary piston motions and must therefore account for piston– and crosshead clearances (Ch. 4). The 3-DOF model includes the crank drive and ring– and crosshead models, which describe on the one hand the motion and oil film dependent forces and moments acting on both crosshead and piston. On the other hand — in the case of the ring models — it describes the oil film dynamics in the ring areas. These are modelled as a free boundary problem including full fluid film lubrication and a passive region, where the gap between cylinder and rings is too big to be fully flooded with oil resulting in a free surface flow (Sec. 3.5).

The gaps between rings and cylinder wall are limited to a minimal gap in the order of the cylinder surface roughness to eliminate non-physically small gaps. The introduced contact forces are used for the calculation of a starving parameter, which is used as an indication for under-lubrication (Sec. 3.3).

A priori, it was not clear if elastohydrodynamic effects play an important role. Therefore, one fully coupled elastohydrodynamic test case was studied in detail, using ABAQUS/Standard to calculate the elastic ring deformations (Sec. 5.3 and 6.2). Results of this study showed that elastohydrodynamic effects play a minor role in the estimation of net-oil flows, that is why they were neglected in the final global lubrication model.

In a next step, the oil film dynamics next to the rings had to be considered. Two major mechanisms were identified: Evaporation of oil due to the high temperatures in the cylinder and gas driven oil flow:

A study of the existing literature (Sec. 1.4: due to the sparse literature concerning compressor cylinder lubrication, literature concerning cylinder lubrication of engines

was evaluated) yielded that oil evaporation as a driving factor of oil consumption can be ruled out: We get estimated evaporation rates between approx. $10^{-3}\,\mathrm{l/h}$–$10^{-1}\,\mathrm{l/h}$, depending on compressor size, which are certainly small compared to usual lubrication rates.

Asymptotic analysis (Sec. 3.6) yielded that the pressure forces of the oil film's Navier–Stokes equations are negligible compared to the viscous forces. Hence, the oil film is driven by the wall shear stress, induced by the gas flow. Furthermore, the slip velocity — the oil film velocity at the front oil–gas — is small compared to the piston velocity for usual film height $< 0.1\,\mathrm{mm}$. Thus, each piston– or rider ring leaves a trace of oil, which is time independent in the global system dynamic time scale.

Furthermore, a CFD calculation of an exemplary compressor is done (Sec. 5.2 and Sec. 6.1) to obtain a more precise estimate of the slip velocities. On the one hand, these calculations confirm the findings mentioned above. They show that oil film flows are for the predominant part negligible, but on the other hand, they give a conclusive explanation for the oil film removal: Around the valve pockets, and generally for greater oil film heights, the simulation shows non-negligible slip velocities, resulting in a removal of any oil accumulations (for instance at the dead end centre position of the outer rings).

In consideration of the aforementioned modelling aspects, the derived global lubrication model comprises the discussed mechanisms and allows to evaluate the lubrication conditions and its progression over time, starting from an initial state. It allows for detailed insights: The results comprise global compressor dynamics (piston and crosshead motion, piston rod bending, forces, etc.) as well as oil film dynamics including net-oil flows along each ring, progression of oil film height on the cylinder wall, decrease and increase of menisci (outer transition zones), etc. Above all, a starving parameter was introduced, which describes the degree of under-lubrication of each ring per revolution. The lubrication model gives indications how to define a compressor-specific lubrication guideline, which does not only specify a lube rate, but also specifies the best locations of lube oil injection.

7.2 Critical discussion

The objective of this study — to derive a comprehensive cylinder lubrication model for reciprocating compressors — requires consideration of a wide field of different effects and mechanisms. Taking all of them into account would have by far exceeded the frame of this work. Therefore, only the most important mechanisms are addressed and idealized conditions are assumed where possible. This approach allowed to derive a working cylinder lubrication model, and it also allows a steady improvement of the derived lubrication model by enhancing the model step by step.

It was a-priori not certain, that the asymmetry due to secondary piston motions leads to a significant accumulated net-oil flow along the rings, being the dominant factor responsible for oil consumption. And, in fact, the net-oil flow over one revo-

lution is very low compared to the net-oil flow over half a revolution, indicating on a first glance hardly any asymmetry and hence its neglect. However, accumulated over thousands of revolutions, the net-oil flow due to the discussed asymmetry sums up to a very realistic quantity in the order of typical lube rates which are derived by empirical guidelines and applied in industry. The results of an exemplary lubrication calculation of a "real" compressor, which is done in Sec. 6.3, are very encouraging and strongly suggest that the derived global lubrication model represents the most important effects leading to oil consumption.

One mechanism, which is not addressed at all, is the formation of oil mist: Its neglect was justified by assuming an idealized lubrication system. In reality, it is not clear what the oil injection looks like, if the entirety of the injected oil will cover the cylinder wall, and what percentage is lost directly because of oil mist formation. This topic is certainly worth to be covered by future studies. An inefficient lube injection might increase the oil consumption significantly. In this work, the presented simulation case starts initially with a uniform film covering the cylinder surface, assuming an ideal lubrication which does not lead to oil mist formation. The piston rings in the exemplary calculated compressor case act as oil barriers and accumulate most of the oil already at the first stroke at one side, leaving the main part of it near the dead end centre position. This result gives the important indication that timed lube injection might be an important factor in minimizing oil consumption.

This brings us to another effect not being discussed or rather extremely simplified: The throw-off of an oil droplet due to the piston's acceleration, or more generally the formation and progression of the menisci at the ring borders, what is called "outer transition zones" in this study. They are strictly geometrically modelled, not accounting for any oil dynamics in this region. This works fine for the downstream border for vanishing menisci, resulting in a downstream film height proportional to the oil flow through the cross-sectional area. However, the situation at the upstream meniscus is unclear: Both its shape as well as the formation of droplets. However, while the formation of the upstream meniscus does not immediately affect the downstream oil trace, the question remains, how the meniscus decreases in time (after each dead end centre). If it declines slower than implemented in this model, it might affect the oil trace, leading to an increase of oil film height in some regions and improving the overall lube conditions.

Another point, which needs to be discussed, is the treatment of wall roughness: The simulation of an exemplary compressor showed, that elastohydrodynamic effects are negligible when evaluating the net-oil flow along a rider ring. Also, wall surface roughness does not have to be considered, since the rider ring is only operating in the affected regime (characterized by minimal gaps of a few microns) for a relatively short time period. Similar results were expected for piston rings. However, actual results show that the piston rings — at least in the simulated compressor case — are working full time at small gap heights of approx. $0.5\,\mu\text{m}$. Compared to the net-oil flow along the rider rings, the net-oil flow along the piston rings is negligible. However, results need to be interpreted with caution, since the piston rings are actually working in the EHL regime, but elastic deformations have been neglected

in the global lubrication model.

To increase the number of piston rings would definitely be of help here, reducing the necessary oil pressure built up between each ring surface and cylinder wall and hence generally increasing the gaps. Since the inclination of piston– and rider ring gaps are solely defined by the piston inclination as well as the ring profiles, changing the ring profiles might improve the situation. In reality, the ring profiles are naturally altered by wear in operation, which might balance the varying load situation. It might be necessary to use the profile of real operated, worn rings to get more realistic results. This, however, leads to the question of parameter sensitivity, which can only be answered by a parameter study. The derived model opens the possibility to study the sensitivity of various parameters. For instance, the impact of oil viscosity on oil consumption could be shown in Sec. 6.3.3. In addition, it would be interesting to study the effects of small changes in, for instance, alignment of crosshead, clearances, ring profiles, crosshead profile, etc. Are, for instance, small parameter variations balanced by different ring profiles, which would be results of parameter specific ring wear? A parameter study should also comprise numerical impacts, like impact of discretisation, impact of contact stiffness, etc.

Another interesting, but yet missing point is the validation of the lubrication model, which was derived by purely theoretical means. A meaningful validation would include experiments, which are, however, very hard to accomplish: They would include measurements of the piston's and crosshead's motion (both tilt and eccentricity), as well as measurements of the oil film covering the cylinder wall. While the first point is feasible to accomplish by standard measurement technology, the second point (measuring of the oil film) is far more difficult: For instance, the oil film height can be measured using the laser-induced-fluorescence technique, which requires an optical assess in the liner (e.g. [51]). This requirement is hard to accomplish, since many compressors have cooling channels around the cylinders. Another option would be the usage of ultrasound: The principle is based on capturing and analysing the reflection of an ultrasonic pulse at the oil film [17], which seems advantageous, since the installation of sensor elements at the outer side of the cylinder line is sufficient, providing localised non-invasive measurements. The inner cylinder wall does not need to be modified, hence the oil film is not affected. Both methods have been used and proven to work for oil film measurements of engine-cylinders, but to the authors knowledge, the have not been applied to measure oil film height of compressor-cylinder walls yet. Another possibility to validate the lubrication model might be the study of ring wear: One could adapt the lubrication according to numerical results and study its impact on ring wear. However, this strategy seams very tedious, since ring wear occurs after many hours of operations requiring very long testing times — the usual service interval is two years.

In summary, the target of deriving a comprehensive lubrication model was successfully derived, which gives detailed insights into cylinder lubrication. It makes it possible to develop improved compressor specific lubrication guidelines, that go into much more detail than do the state-of-the-art empirical guidelines. By taking into account compressor-specific parameters such as clearances, ring profiles, moments of

inertia and oil viscosity, the new model provides not only an estimate of the optimal lube rate for a given compressor, but also guidance on the timing of oil injections.

However, the reliability of such derived lubrication guideline has to be proven yet, and the significance of various input parameters will have to be assessed in further studies. Furthermore, future studies should enhance the presented global lubrication model including the following aspects:

- formation of oil mist due to lube injection,

- throw-off of an oil droplet due to the piston's acceleration,

- formation and progression of the menisci at the ring borders,

- and elastohydrodynamic effects concerning piston ring lubrication.

126

Nomenclature

List of Symbols

α_B	pressure-viscosity coefficient used in Barus law that depends on pressure and temperature
Δt	time increment
$\varnothing_{\mathrm{pr}}$	piston ring's diameter (of neutral axis)
$\dot{w}$	rate of wear depth
ϵ	eccentricity ratio of piston
ϵ_{c}	compressibility of gas
ϵ_{l}	gap to length ratio
γ	tilt of mounting position of compressor
μ	dynamic viscosity
ν	kinematic viscosity
ω	angular velocity of compressor
ω_{PR}	eigenfrequencies of piston/piston rod assembly
ϕ	angle, that defines azimuthal position of calculation area
ϕ_{valve}	"effective" cross section of valve
ϕ_{w}	wetting angle: range of fully flooded ring area in azimuthal direction
ρ_{PR}	density of piston rod material
ρ_{pr}	density of piston ring
λ_s	relation of crank radius to connecting rod length
τ	shear stress or time
Θ	crank angle
Θ_V	fluid specific constant used in Vogel's equation
A_{c}	proportional sectional area to derive contact force
A_{PR}	sectional area of piston rod
A_{por}	cross sectional area of the porous region
A_{pr}	piston ring's cross sectional area
b	fluid specific constant used in Vogel's equation
C	constant used in Ubbelohde–Walter equation
$c_{0,\mathrm{CH}}$	initial clearance of the cross head at zero tilt

List of Symbols

c_0	initial clearance of the rider ring - the minimal gap between rider ring and cylinder at zero eccentricity and zero tilt
d_{cyl}	diameter of cylinder
e	eccentricity of piston
E_{pr}	Young's modulus of piston ring
E_{PR}	Young's modulus of piston rod material
E_{r}	Young's modulus of rider ring
E	Young's modulus
f_{e}	empirical factor used to derive basic lube rates
F_{c}	contact force due to elastic deformation
F_{C}	generalized crosshead force
F_{P}	generalized piston force
F_{gas}	gas forces acting on piston
F_{oil}	vertical piston force
F	volume fraction
g	gravitational acceleration
h_{pr}	piston ring's height
H_{f}	representative height of oil film
h_{min}	minimal gap between rider ring and cylinder wall
h_{film}	oil film thickness
h_{rl}	gap between rider ring and cylinder wall
h	gap between any ring and cylinder wall
h_{trans}	height of "outer" transition zone
I_{CR}	mass moment of Inertia (connecting rod)
I_{CH}	mass moment of Inertia (cross head)
I_{P}	mass moment of Inertia (piston)
$J_{\mathrm{pr,y}}$	piston ring's area moment of intertia
J_{PR}	area moment of inertia (piston rod)
K	fluid specific constant used in Ubbelohde–Walter equation
k	non-dimensional wear coefficient
k	nondimensional wear coefficient
l_{C}	length of compression chamber
l_{CR1}	distance connecting rod bearing (small end)–center of connecting rod
l_{CR2}	distance connecting rod bearing (big end)–center of connecting rod
l_{CR}	gauge of connecting rod
l_{CH1}	distance cross head center of mass–end of cross head nut
l_{CH}	distance cross head bearing–end of cross head nut
l_{P}	distance between center of mass of piston and cross head bearing

l_{PR}	length of piston rod
l_{b}	bending length of piston rod
l_{st}	length of piston stroke + clearance between piston and cylinder end
l_{trans}	length of "outer" transition zone
m_{CR}	mass of connecting rod
m_{CH}	mass of cross head (including nut)
m_{P}	mass of piston
M_{C}	generalized crosshead moment
M_{P}	generalized piston moment
p_{d}	discharge pressure
p_{E}	pressure in compression chamber
p_{gas}	gas pressure
p_{oil}	hydrodynamic oil pressure
p_{s}	suction pressure
q	bending degree of piston rod
q	oil volume flow per unit depth
q_{trans}	oil flow in or out the "outer" transition zone per unit depth
r_{cd}	crank radius
R_{cyl}	liner radius
r_{pr}	piston ring's radius (of neutral axis)
r_{PR}	radius of piston rod
$r_{\mathrm{i,r}}$	inner radius of rider ring
$r_{\mathrm{o,r}}$	outer radius of rider ring
$\mathrm{res}_{\mathrm{ring}}$	residuum of oil volume calculation
rev	revolution of crank drive
Re	nondimensional Reynolds number
RPM	revolutions per minute
RPS	revolutions per second
St	nondimensional starving parameter
stroke	piston stroke
h_{r}	height of rider ring
t_{C}	value of temperature expressed in Celsius
T_{d}	discharge temperature
T	value of temperature expressed in Kelvin
T_{s}	suction Temperatur
t_{por}	thickness of porous region
t	time in s
t_{ac}	acoustic time scale
t_{bl}	boundary time scale
t_{gl}	global system dynamic time scale
t_{lub}	lubrication time scale
u	velocity in x-direction

U_{c}	characteristic velocity
v_{P}	piston velocity in axial direction
U	rel. velocity of cylinder wall
U_{m}	mean piston velocity
v	velocity in y-direction
$\dot{V}^{(\mathrm{lube})}$	total oil demand
$\dot{V}^{(\mathrm{oil})}_{\mathrm{convection}}$	convective oil flow through discharge Valves
$\dot{V}^{(\mathrm{oil})}_{\mathrm{DV,CE}}$	total oil flow through discharge Valves at crank-end side
$\dot{V}^{(\mathrm{oil})}_{\mathrm{DV}}$	total oil flow through discharge Valves
$\dot{V}^{(\mathrm{oil})}_{\mathrm{evaporation}}$	oil flow through discharge Valves due to evaporation of oil
$\dot{V}^{(\mathrm{oil})}_{\mathrm{DV,HE}}$	total oil flow through discharge Valves at head-end side
$\dot{V}^{(\mathrm{oil})}_{\mathrm{oil\,mist}}$	oil flow through discharge Valves in the form of oil mist
$\dot{V}^{(\mathrm{oil})}_{\mathrm{pack}}$	oil flow to connecting piece throuch packing
$\dot{V}^{(\mathrm{oil})}_{\mathrm{P}}$	oil flow along piston assembly
V	total cell volume per unit depth
V_{oil}	cell volume per depth filled with lubricant
V_{w}	volume of wear being worn away
w	velocity in z-direction or displacement of piston rod due to bending
B	axial length of calculation regime (for the crosshead's pressure calculation: length of the crosshead; for the cylinder region's pressure calculation: the ring's width)
w_{pr}	piston ring's width
b_{P}	width of piston
w_{r}	width of rider ring
x_{CR}	horizontal position of connecting rod center
x_{C}	horizontal position of cross head bearing center
x_{CH}	horizontal position of center of mass of cross head including cross head nut
x_{P}	horizontal position of piston center
y_{CR}	vertical position of connecting rod center
y_{C}	vertical position of cross head bearing center
y_{CH}	vertical position of center of mass of cross head including cross head nut
y_{pr}	piston-ring displacement along the piston groove
y_{P}	vertical position of piston center

Acronyms

0D, 1D, 2D, 3D	zero–, one–, two–, three–dimensional
API	American Petroleum Institute
ASTM	American Society for Testing and Materials
CFD	computational fluid dynamics
DOF	degrees of freedom
EHL	elastohydrodynamic lubrication
FE	finite element
ISO	International Organisation for Standardization
LST	laser surface texturing
SLATEC	Sandia, Los Alamos, Air Force Weapons Laboratory Technical Exchange Committee
UDF	user defined subroutine
URANS	unsteady Reynolds-averaged Navier–Stokes equation
VOF	volume-of-fluid method

Subscripts

0	stagnation terms
c	contact terms
CH	crosshead
CR	connecting rod
f	oil film
g	gas
i	row i
j	line j
k	j times number of rows + i
P	center of cell, or piston
PR	piston rod
pr	piston ring
r	rider ring
ring	ring zone
sub	value corresponding to ring submodel
trans	transition zone
W,E,S,N	center of cell west, east, south, north of cell P
w,e,s,n	west-, east-, south-, north- border of cell P
x,y	force–, moment– or length components in x,y direction

Superscripts

*	intermediate result at current time step, to be corrected by residuum
lube	oil which is transported through valve
n	result at current time step
n-1	result at previous time step
p,q	index of eccentricity loop (p) and inner loop (q) in EHL formulation

Bibliography

[1] *ANSYS FLUENT Theory Guide*, November 2011.

[2] A. Almqvist, J. Fabricius, A. Spencer, and P. Wall. Similarities and differences between the flow factor method by Patir and Cheng and homogenization. *Journal of Tribology*, 133(3):031702–031702–5, July 2011. ISSN 0742-4787. doi: 10.1115/1.4004078.

[3] G. Barr. The determination of the viscosity of oils at high temperatures. In *Proc. General Discussion on Lubrication and Lubricants*, volume 2, pages 217–221, 1937.

[4] C. Barus. Art. x.–isothermals, isopiestics and isometrics relative to viscosity. *American Journal of Science (1880-1910)*, 45(266):87, 1893.

[5] G. Bayada and J. B. Faure. A double scale analysis approach of the reynolds roughness comments and application to the journal bearing. *Journal of Tribology*, 111(2):323–330, Apr. 1989. ISSN 0742-4787. doi: 10.1115/1.3261917.

[6] B. Bhushan. *Introduction to Tribology*. John Wiley & Sons, 2013.

[7] H. Bloch and J. Hoefner. *Reciprocating Compressors:: Operation and Maintenance*. Elsevier Science, 1996. ISBN 9780080515946.

[8] H. P. Bloch and C. Soares. *Process Plant Machinery*. Elsevier, 1998.

[9] M. Braun and W. Hannon. Cavitation formation and modelling for fluid film bearings: a review. *Proceedings of the Institution of Mechanical Engineers, Part J: Journal of Engineering Tribology*, 224(9):839–863, 2010.

[10] A. Cameron and C. Mc Ettles. *Basic Lubrication Theory*. E. Horwood Chichester, 1976.

[11] H. Czichos. *Hütte: Die Grundlagen der Ingenieurwissenschaften*. Springer, 2013.

[12] V. D'Agostino and A. Senatore. 10 - Fundamentals of lubrication and friction of piston ring contact. In H. Rahnejat, editor, *Tribology and Dynamics of Engine and Powertrain*, pages 343 – 386. Woodhead Publishing, 2010. ISBN 978-1-84569-361-9. doi: http://dx.doi.org/10.1533/9781845699932.2.343.

[13] D. Dowson, B. Ruddy, and P. Economou. The elastohydrodynamic lubrication of piston rings. *Proceedings of the Royal Society of London A*, 386(1791):409–430, 1983.

[14] W. Dresel et al. *Lubricants and Lubrication*. John Wiley & Sons, 2007.

[15] Z. Dursunkaya and R. Keribar. Simulation of secondary dynamics of articulated and conventional piston assemblies. *SAE transactions*, pages 853–863, 1992.

[16] Z. Dursunkaya, R. Keribar, and V. Ganapathy. A model of piston secondary motion and elastohydrodynamic skirt lubrication. *Journal of Tribology*, 116(4): 777–785, 1994.

[17] R. S. Dwyer-Joyce, T. Reddyhoff, and J. Zhu. Ultrasonic measurement for film thickness and solid contact in elastohydrodynamic lubrication. *Journal of Tribology*, 133(3):031501–031501, June 2011. ISSN 0742-4787. doi: 10.1115/1. 4004105.

[18] M. Esfahanian, B. J. Hamrock, and A. A. Elsharkawy. On the hydrodynamic lubrication analysis of piston rings. *Lubrication Science*, 10(4):265–286, 1998.

[19] C. L. Felter. Numerical simulation of piston ring lubrication. *Tribology International*, 41(9–10):914 – 919, 2008. ISSN 0301-679X. doi: http://dx.doi.org/10.1016/j.triboint.2007.11.018. Nordtrib 2006.

[20] J. H. Ferziger and M. Peric. *Numerische Strömungsmechanik*. Springer, 2008.

[21] R. Gamble, M. Priest, and C. Taylor. Detailed analysis of oil transport in the piston assembly of a gasoline engine. *Tribology Letters*, 14(2):147–156, 2003.

[22] J. Gehannin, M. Arghir, and O. Bonneau. A volume of fluid method for air ingestion in squeeze film dampers. *Tribology Transactions*, 59(2):208–218, 2016. doi: 10.1080/10402004.2015.1023409.

[23] J. Greenwood and J. Tripp. The contact of two nominally flat rough surfaces. *Proceedings of the Institution of Mechanical Engineers*, 185(1):625–633, 1970.

[24] J. Greenwood and J. P. Williamson. Contact of nominally flat surfaces. *Proceedings of the Royal Society London A*, 295(1442):300–319, 1966.

[25] S. Gulwadi. A mixed lubrication and oil transport model for piston rings using a mass-conserving algorithm. *Journal of Engineering for Gas Turbines and Power*, 120(1):199–208, 1998.

[26] B. Hacioglu and Z. Dursunkaya. Effect of oil feed groove on compressor piston lubrication. In *International Compressor Engineering Conference*, 2008.

[27] B. Hacioglu and Z. Dursunkaya. Effect of surface texture on compressor piston lubrication. In *International Compressor Engineering Conference*, 2010.

[28] R. Hahn and E. Holm. Electric contacts. *New York: Springer*, 1946.

[29] D.-C. Han and J.-S. Lee. Analysis of the piston ring lubrication with a new boundary condition. *Tribology International*, 31(12):753–760, 1998.

[30] P. C. Hanlon. *Compressor Handbook*. McGraw-Hill,, 2001.

[31] H. M. Herbst and H. H. Priebsch. Simulation of piston ring dynamics and their effect on oil consumption. *SAE transactions*, pages 862–873, 2000.

[32] C. W. Hirt and B. D. Nichols. Volume of Fluid (VOF) Method for the Dynamics of Free Boundaries. *Journal of Computational Physics*, 39(1):201–225, 1981.

[33] A. P. Institute. *Reciprocating Compressors for Petroleum, Chemical, and Gas Industry Services*, 5 edition, December 2007. Errata 2, July 2010.

[34] P. Johansson. *Oil-related particle emissions from diesel engines*. PhD thesis, KTH, 2008.

[35] R. Klein and N. Peters. Cumulative effects of weak pressure waves during the induction period of a thermal explosion in a closed cylinder. *Journal of Fluid Mechanics*, 187:197–230, 1988. doi: 10.1017/S0022112088000400.

[36] Y. Kligerman, I. Etsion, and A. Shinkarenko. Improving tribological performance of piston rings by partial surface texturing. *Journal of Tribology*, 127 (3):632–638, 2005.

[37] D. Knežević, V. Savić, et al. Mathematical modeling of changing of dynamic viscosity, as a function of temperature and pressure, of mineral oils for hydraulic systems. *Facta Universitatis. Series. Mechanical Engineering (Serbia).*, 2006.

[38] K.-H. Küttner. *Kolbenmaschinen*. Springer, 2013.

[39] L. Liu. *Modeling the performance of the piston ring-pack with consideration of non-axisymmetric characteristics of the power cylinder system in internal combustion engines*. PhD thesis, Massachusetts Institute of Technology, 2005.

[40] L. Liu, T. Tian, and E. Yilmaz. Modeling oil evaporation from the engine cylinder liner with consideration of the transport of oil species along the liner. In *World Tribology Congress III*, pages 579–580. American Society of Mechanical Engineers, 2005.

[41] F. R. Menter. Two-equation eddy-viscosity turbulence models for engineering applications. *AIAA journal*, 32(8):1598–1605, 1994.

[42] Noria Corporation. Reciprocating compressor basics. `https://www.machinerylubrication.com/Read/775/reciprocating-compressor`. Accessed: 2019-03-07.

Bibliography

[43] H. Parkus. *Mechanik der festen Körper.* Springer, 2013.

[44] N. Patir and H. S. Cheng. An average flow model for determining effects of three-dimensional roughness on partial hydrodynamic lubrication. *Journal of Lubrication Technology*, 100(1):12–17, Jan. 1978. ISSN 0742-4787. doi: 10. 1115/1.3453103.

[45] A. Prata, J. Fernandes, and F. Fagotti. Piston lubrication in reciprocating compressors. *Revista de Engenharia Térmica*, 1(1):56–63, 2001.

[46] O. Reynolds. On the theory of lubrication and its application to mr. beauchamp tower's experiments, including an experimental determination of the viscosity of olive oil. *Proceedings of the Royal Society of London*, 40:191–203, Jan. 1886. ISSN 03701662.

[47] G. H. Schneider. Kompression und Expansion eines Gases in einem Zylinder als Störproblem. *Acta Mechanica*, 41(3):157–184, Sep 1981. ISSN 1619-6937. doi: 10.1007/BF01177345.

[48] C. J. Seeton. Viscosity-temperature correlation for liquids. In *STLE/ASME 2006 International Joint Tribology Conference*, pages 131–142. American Society of Mechanical Engineers, 2006.

[49] L. F. Shampine. Solving 0= f (t, y (t), y'(t)) in MATLAB. *Journal of Numerical Mathematics*, 10(4):291–310, 2002.

[50] M. Smith. *ABAQUS/Standard User's Manual*, 6.9 edition, 2009.

[51] G. Tamai. *Experimental study of engine oil film thickness dependence on liner location, oil properties and operating conditions.* PhD thesis, Massachusetts Institute of Technology, 1995.

[52] W. H. Vandevender and K. H. Haskell. The SLATEC Mathematical Subroutine Library. *SIGNUM Newsl.*, 17(3):16–21, Sept. 1982. ISSN 0163-5778. doi: 10.1145/1057594.1057595.

[53] M. Wang and D. Kassoy. Evolution of weakly nonlinear waves in a cylinder with a movable piston. *Journal of Fluid Mechanics*, 221:23–52, 1990.

[54] J. Yance and J. Hagan. Lube reduction in reciprocating compressors. `https://www.arielcorp.com/Technical-Papers/Lube-Reduction-in-Reciprocating-Compressors/`. Accessed: 2019-01-28.

[55] E. Yilmaz. *Sources and characteristics of oil consuption in a spark-ignition engine.* PhD thesis, Massachusetts Institute of Technology. Dept. of Mechanical Engineering, 2003.

[56] E. Yilmaz, T. Tian, V. W. Wong, and J. B. Heywood. The contribution of different oil consumption sources to total oil consumption in a spark ignition engine. Technical report, SAE Technical Paper, 2004.

LEBENSLAUF

Persönliche Information

Name	Bernhard Fritz
Geburtsdatum	20. September 1983, Wien, Österreich
Adresse	Elisabethallee 81/1/7, 1130 Wien, Österreich
E-Mail	bernhard.fritz@aol.at

Schul- und Berufsbildung

2003–2010	Diplomstudium Maschinenbau an der TU-Wien; *Hauptschwerpunkt:* Modellbildung und Simulation *Vertiefungen:* FE und andere numerische Ingenieursmethoden & Methoden der Strömungsmechanik *Titel der Diplomarbeit:* Development of a Testing and Simulation Protocol for proximal Femurs
1994–2002	Schüler des Gynmasiums Sacré Coeur Pressbaum
1990–1994	Schüler der Volksschule Pressbaum

Arbeitserfahrung

seit 2012	Hoerbiger Wien, Wien
2010–2012	Siemens VAI, Linz